# Coupling between fluorescent emitters and surface plasmons in the weak and strong interaction regimes in spatially structured multilayer samples

Camilo Perez

PSL UNIVERSITÉ PARIS

**THÈSE DE DOCTORAT**

DE L'UNIVERSITÉ PSL

Préparée à **l'ESPCI**

Institut Langevin

# Coupling between fluorescent emitters and surface plasmons in the weak and strong interaction regimes in spatially structured multilayered samples

***Couplage entre émetteurs fluorescents et plasmons de surface en régime d'interaction faible et forte dans des échantillons multicouches structurés spatialement***


Soutenue par

**Camilo PEREZ**

Le 1 février 2022

École doctorale n°564

**Physique en Ile-de-France (EDPIF)**

Spécialité

**Physique**


Composition du jury :

| | |
|---|---|
| **Agnès MAÎTRE**<br>Professeure,<br>Sorbonne Université | *Présidente du jury* |
| **Renaud BACHELOT**<br>Professeur,<br>Université de Technologie de Troyes | *Rapporteur* |
| **Celine FIORINI**<br>Chercheur CEA,<br>Université Paris-Saclay | *Rapporteur* |
| **Paolo MAIOLI**<br>Chargé de Recherche CNRS,<br>Université Lyon 1 | *Examinateur* |
| **Yannick DE WILDE**<br>Directeur de recherche CNRS,<br>ESPCI Paris - PSL | *Directeur de thèse* |
| **Valentina KRACHMALNICOFF**<br>Chargée de recherche CNRS,<br>ESPCI Paris - PSL | *Encadrante* |

ESPCI PARIS | PSL

# Acknowledgements

In the following lines, I would like to express my gratitude to the people who accompanied me through my PhD. I must say that this period has been very particular and challenging, and so it is a period in which I have grown as in any other. For this, I have to thank the people that have accompanied me in my professional and personal life. I want to start by thanking my supervisor Valentina Krachmalnicoff, who trusted me to join her at Institut Langevin and opened me this incredible opportunity. From the beginning, you were there caring about my training and giving me the courage to not be disappointed if something does not go as expected. After numerous samples, an incredible amount of data, and a pandemic, I got to understand the meaning of perseverance and compromise to work following your example. Also, I thank you for teaching me the value of sharing and debating knowledge in a scientific community. In these weird times, you never stopped believing in the fruits of hard work and consistency. For all of this thank you, Valentina.

At Institut Langevin, I had the pleasure to work closely with wonderful people to whom I am grateful. When I arrived at the lab, I had the chance to be formed by Vivien Loo. I cannot think of anyone else that has taught me that many things in such a short period. I admire your skills in doing experiments, up to the end I kept using some gadgets or codes that you created. In my last two years, I worked side by side with Kevin Chevrier who is someone very pleasant to work with and to discuss the great questions of science. I thank you for being my mate, giving always support, and maintaining a good mood through the struggles that we had. At the same time, I had the chance to work on a few experiments with Margoth Cordova, from whom I learned from her vast experience in the domain. Also, it was good to have someone that comprehends in first-person what is like to deal with the migratory administration system. I would also like to thank Yannick de Wilde who, besides following the

progress of my project and giving pertinent advice, I have the pleasure to consider as a friend. While spatial-temporal conditions allow it, I will keep passing by the Institute to share a short break.

Something that I value and learned to value, is the importance of working together with other research groups. I would like to thank all the people from the different teams I worked with during my thesis. To Thomas Pons and Sandrine Ithurria, which provide the quantum dots and with whom we discussed their temporal response. To all the people from the ILM Lyon that I met. Since my first year, I had the chance to go and perform experiments at the ILM where Jean-Michel Benoit and Clémentine Symonds welcomed me and taught me the sample fabrication process and the optics lab, and Alban Gassenq invited me to use the gray room for lithographing the J-aggregates. Also, I thank Antoine Bard for the necessary discussions that we had and for answering some of my tedious questions. I especially thank Joel Bellessa, for sharing with me his passion for physics and maîtrise of Frenglish. I greatly appreciate that you were able also to exchange with me about the project, general topics in physics, and even theater, and for accepting to be part of my jury. In my last PhD year, I had the pleasure to collaborate with the Nanophotonics group of Laboratorie Charles Fabry. It has been enlightening and also pleasant to work with brilliant people such as Elise Bailly, Benjamin Vest, and Jean-Jaques Greffet. Also, I deeply thank Renaud Bachelot and Céline Fiorini for reviewing my thesis. I appreciate the time that you give to read it and make the respective reports, which were very encouraging. Likewise, I thank Agnes Maitre and Paolo Maioli for accepting to be at my defense as examinators. It was a great experience to meet you all and to discuss with you at the defense.

I would like to thank the people with whom we had interesting conversations or helped me during my thesis. To Jeanne, for her friendship and the multiple conversations regarding light-matter strong coupling phenomena, to Bart for the fundamental questions through the iron curtain, to Loubnan for deciphering together the R9 operation, to Samuel (Salvador) for his council in electronics (and electricity), to Luis for all the phone calls requiring to share his knowledge, to Ignacio, Clement, and Max for the discussions regarding microscopy, for searching inexistent filters and for lending optical paper. I also want to thank all the PhDs and postdocs with whom I shared good times at the lab. I especially thank Cécile and Samer for their support, emo-

tionally and computationally, for the birthdays and all the great (and not that great) times in R20. I hope for the best for their future and I hope that the plant in the office will survive as an eternal and silent witness of our passage.

Finally, I will like to thank people that are essential in my life. To my family, especially to my mom who from time to time had the courtesy to ask me about my project and tolerate 15 minutes of an incomprehensible monologue. Also to my aunt and uncle, Alba and Gilles for all the care, and the small and big lessons... I conclude this part by thanking someone to who I owe more than a recognition. To my partner of these years, Romane, who has to stand the bad days at my side and gave me the force to keep going in the toughest moments through the simple and everyday lovely gestures.

# Table of contents

# Introduction

The interaction between a well-defined quantum system that has optical transitions and its environment has been widely explored [1]. It is driven by the local density of states (LDOS), which informs about the number of modes in the environment interacting with the system. Two main interaction regimes can be considered: weak and strong coupling. In the weak coupling regime, emitter/environment interaction is characterized by a modification of the spontaneous emission rate of the emitter with respect to vacuum. In contrast, the strong coupling regime involves a coherent energy exchange between the emitter and the environment that modifies the eigenfrequencies at the resonant energies. Light-matter interaction in the strong coupling regime is a subject that has been explored for a wide variety of emitters in different electromagnetic environments. In this thesis, we study a particular phenomenon involving two different emitters and an electromagnetic mode that propagates at the interface formed between a metal and a dielectric material. This mode is called a *surface plasmon polariton* (SPP).

This thesis has been done in the frame of the *Plashybrid* ANR project led by J. Bellessa from Institut Lumière Matière (ILM) and including three other partners: Institut Langevin (IL) (scientific coordinator Valentina Krachmalnicoff), Institut de Science et d'Ingénierie Supramoléculaires (ISIS) (scientific coordinator Thomas Ebbesen), and Institut des Sciences Analytiques (ISA) (scientific coordinator François Bessueille). We have also benefited from the collaboration with the team of Jean-Jaques Greffet from Laboratoire Charles Fabry de l'Institut d'Optique (LCFIO), and Thomas Pons and Sandrine Ithurria from Laboratoire de Physique et d'Étude des Matériaux (LPEM). Following the pioneering experiments performed at ILM on strong coupling with plasmons and J-aggregates [2–4], the objective of the ANR project concerning my thesis was to combine the skills available at ILM to synthesize samples

and probe the global optical response of a strongly coupled system with those of IL to perform local optical measurements on plasmonic nanostructures with fluorescent emitters [5; 6], to study the behavior of a system involving surface plasmons and J-aggregates in the presence of other emitters than J-aggregates, according to their nature and spatial distribution. We decided to push our investigations following two directions: the coupling of weakly coupled quantum emitters to a strongly coupled system and the coupling between already strongly coupled systems. For these purposes, samples containing silver films and a patterned layer of J-aggregates were fabricated and then combined with semiconductor quantum dots provided by LPEM. During my PhD, I performed several journeys to ILM dedicated to the production and characterization of such samples. Similarly, we benefited from the visit of Antoine Bard, a PhD candidate from ILM, to our group at IL to perform local optical measurements. To deepen our understanding of our system, we had the chance to collaborate with the LCFIO team led by Jean-Jacques Greffet who proposed a theoretical model based on a local form of Kirchhoff's law [7] to describe our experimental results. Important efforts were then invested by his PhD student Elise Bailly to develop the numerical code adapted to our system and using our input parameters, which led to a very good agreement with our experimental observations [8; 9]. In the experiments presented in this thesis, as in the development of the respective setups, I worked together with Kevin Chevrier, who previously did his PhD in Joel Bellessa's group and is currently a postdoctoral researcher at IL.

This thesis is organized as follows. Chapter 1 gives a brief historical context of preceding studies that establish the foundation of fluorescent emitters and surface plasmons. We then focus on recent previous works regarding the spatial coherence of J-aggregates coupled to SPPs and plasmon-assisted energy transfer, on which we based the objectives of this thesis. We describe in Chapter 2 the theoretical fundamentals of the coupling between fluorescent emitters and SPPs. Through a coupled oscillators model, we distinguish the differences between the weak and strong coupling regimes for light-matter interaction. We also describe the specificities of this interaction for fluorescent molecules and SPPs. Chapter 3 presents the experimental setup used for characterizing the spectral and temporal properties of the samples studied in this thesis. We detail the optical path for performing real and reciprocal-space spectroscopy and decay rate measurements. Chapter 4 presents the leading

work of this PhD project. We start by describing the elements that compose our system, including the photophysical properties of J-aggregates and quantum dots, and the sample's fabrication process. We then show a series of measurements dedicated to the understanding of the coupling between the quantum dots and the strongly coupled system composed by the J-aggregates and the SPP. We also present a model based on local Kirchhoff's law for photoluminescence and the corresponding simulations performed at LFCIO. Chapter 5 presents a second study aimed to observe energy transfer between two strongly coupled dyes to an SPP. First, we describe the periodic structuration of the sample in which the two dyes are spatially separated. These samples were developed by the ILM team based on an original patterning method using the Moiré effect. We demonstrate the hybridization of the silver SPP with the emitters through reflectometry measurements. Then, we report on the polariton-assisted energy transfer observed through photoluminescent measurements [10]. Finally, we end this manuscript presenting the general conclusions of this research and an outlook for future experiments.

# References

[1] S. Haroche and J. M. Raimond, *Exploring the Quantum: Atoms, Cavities, and Photons*, Oxford Univ. Press, Oxford (2006). 1

[2] J. Bellessa, C. Bonnand, J. C. Plenet, and J. Mugnier, *Phys. Rev. Lett.* **93**, 036404 (2004). 1

[3] S. Aberra Guebrou, C. Symonds, E. Homeyer, J. C. Plenet, Y. N. Gartstein, V. M. Agranovich, and J. Bellessa, *Phys. Rev. Lett.* **108**, 066401 (2012).

[4] K. Chevrier, J. M. Benoit, C. Symonds, S. K. Saikin, J. Yuen-Zhou, and J. Bellessa, *Phys. Rev. Lett.* **122**, 173902 (2019). 1

[5] D. Bouchet, D. Cao, R. Carminati, Y. De Wilde, and V. Krachmalnicoff, *Phys. Rev. Lett.* **116**, 037401 (2016). 2

[6] D. Bouchet, E. Lhuillier, S. Ithurria, A. Gulinatti, I. Rech, R. Carminati, Y. De Wilde, and V. Krachmalnicoff, *Phys. Rev. A* **95** (2017). 2

[7] J.-J. Greffet, P. Bouchon, G. Brucoli, and F. Marquier, *Physical Review X* **8**, 021008 (2018). 2

[8] C. Perez, *et al. In preparation* (2021). 2

[9] E. Bailly, *et al. In preparation* (2021). 2

[10] A. Bard, *et al. In preparation* (2021). 3

# Chapter 1

# Strong coupling between J-aggregates and SPPs

## Contents

In this chapter, we introduce the context of the research presented in this thesis. In section 1.1, we review the historical development of studies of strongly coupled emitters that achieved breakthroughs in the field. Then, we review some seminal papers about the observation of strong coupling between an organic dye and an SPP. In section 1.2, we focus on previous research regarding the spatial coherence of the strongly coupled systems and the long-range energy transfer observable between fluorescent emitters coupled to SPPs. These works constitute the cornerstones on which our experiments are based. The specific objectives that we pursuit along this work are presented in section 1.3.

## 1.1 Historical survey

The simplest light-matter system consists of a two-level emitter interacting with a single electromagnetic mode supported by the environment. In practice, this is performed by placing a system with a radiative transition, such as an atom or molecule, inside an electromagnetic resonator that supports a few modes, such as a cavity. In such a system, Purcell *et al.* [1] made a major discovery in the 1940s regarding the interaction between hydrogen nuclei and electromagnetic fields oscillating at radio frequencies. They noted that the spontaneous emission of a spin could be modified by changing the boundary conditions imposed to the vacuum field. In 1970, Drexhage's experiment demonstrated that the spontaneous emission decay rate of a fluorescent emitter depends on its local environment [2]. To do so, he observed the decay rate of a layer of europium ions as a function of the distance to a silver mirror. In the mid-1980s, pioneering experiments reached the strong interaction regime using transitions between Rydberg levels coupled to microwave superconducting cavities [3–5]. The extension of strong coupling to optical wavelengths was performed with an atomic transition coupled to optical Fabry–Perot cavities, first with ensembles of atoms [6–8] and later with a single atom [9] inside a high-finesse cavity. The contribution of Weisbuch *et al.* in 1992 marked the integration of solid-state systems in the field. The occurrence of strong exciton–photon coupling in reflectivity spectra was demonstrated for quantum wells as an active medium in GaAs–GaAlAs based quantum microcavities [10].

The strong coupling behavior of a system is characterized by an energy splitting

of the system's states at the resonance between the uncoupled radiative transition and the electromagnetic mode. This energy splitting is the signature of the strong coupling regime of interaction in the spectral domain and it is referred to as the *Rabi splitting*. In the late 1990s, inorganic semiconductors integrated into microcavities at cryogenic temperatures showed Rabi splittings of the order of ~ 10 meV [11], which at optical energies represents less than 1% of the transition energy. In 1998 Lidzey *et al.* published the first report concerning organic dyes for realizing strong coupling: a large Rabi splitting (more than 100 meV) at room temperature was reported [12; 13]. This experiment consisted of placing a dye-doped polymer layer inside a cavity constituted by Bragg mirrors, as shown in the scheme of Figure 1.1(a). The microcavity was designed so that the angular-dependent energy spectrum matches the dye's absorption peak at a given angle. Figure 1.1(b) shows the dispersion relation of the coupled system showing a large Rabi splitting $\hbar\Omega = 110$ meV. By raising the concentration of the dye inside the cavity a splitting of 160 meV was achieved. The robustness of this strong coupling effect suggested that there were advantages in using organic dyes in the search for room-temperature strong coupling phenomena.

The history of coupling between organic dyes and surface plasmon polaritons goes back to the 1980s [14] when Pockrand *et al.* [15] reported a dispersion relation with multiple branches in 1982 in a surface plasmon attenuated total reflection experiment for a Langmir-Blogett dye film on a silver surface. This work was followed up more than twenty years later in 2004, when Bellessa *et al.* [16] reported strong coupling in a system consisting of a planar thin film of a dye, spin-coated on top of a silver layer, as represented in Figure 1.2(a). A Rabi splitting of 180 meV was observed in the dispersion relation obtained from reflectivity measurements, as shown in figure 1.2(b). In these studies, instead of resonant modes in optical cavities, the emitters couple to the propagating modes at the metal-dielectric interface, i.e., the SPPs. Moreover, the dye films that were used in both works were cyanine molecules aggregated in a head-tail arrangement (J-aggregates) with a large dipole moment that strongly interacts with light. An additional characteristic of J-aggregates strongly coupled to SPPs is that the hybridization of the electronic excitations and plasmonic modes entails extended coherent states in the medium [17], in which the fluorescence of distant molecules interfere. Experiments exploring this property are introduced in the following section.

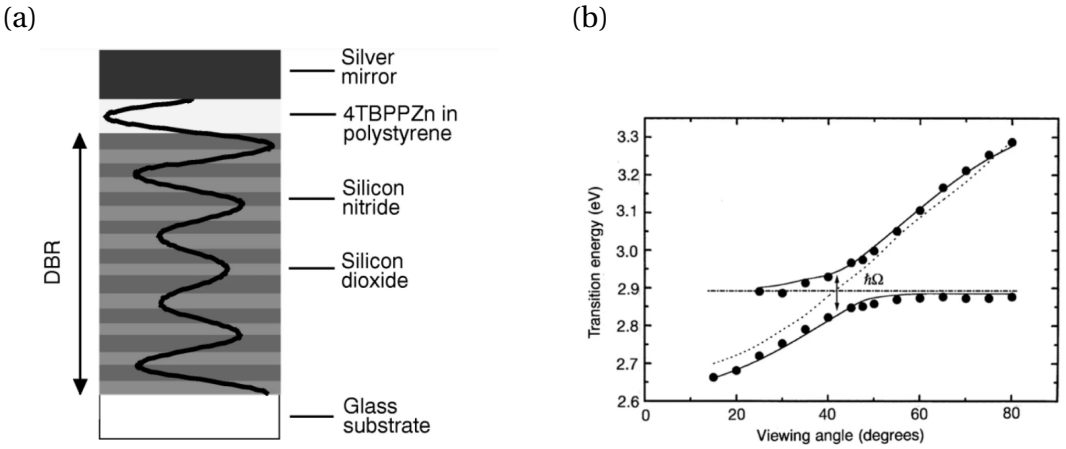


Figure 1.1 – (a) Scheme of a microcavity consisting of a distributed Bragg reflector (DBR) formed by alternating pairs of silicon nitride (refractive index n = 1.95) and silicon dioxide (n = 1.45) $\lambda/4$ layers, a blend of polystyrene and 4TBPPZn on top of the DBR mirror and a second mirror (on top) made by silver evaporation. The confined field possesses an antinode in the centre of the organic layer to maximize exciton–photon coupling. (b) Angular dispersion of the coupled modes in the microcavity showing a Rabi splitting of $\hbar\Omega = 110$ meV. The horizontal dash-dotted line at 2.88 eV is the 4TBPPZn exciton transition energy in the polystyrene blend film. The dotted line shows the measured angular dispersion of the photon mode for a control microcavity that contained polystyrene without the dye. Images taken from [12].

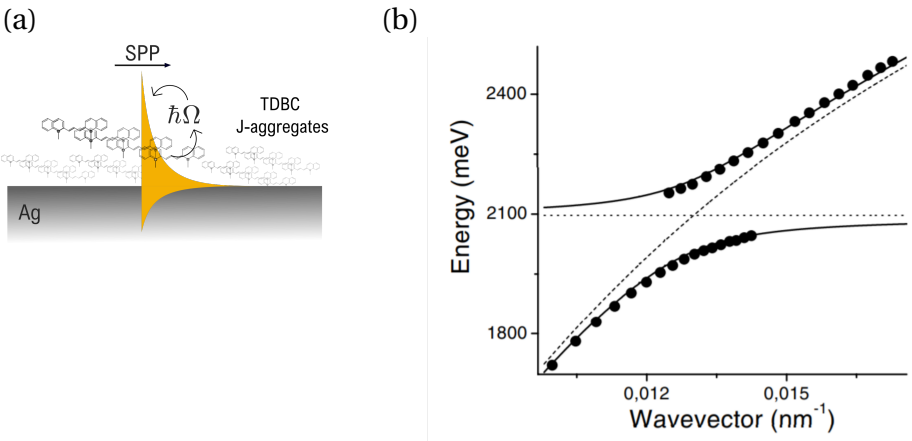


Figure 1.2 – (a) Sketch of a layer of J-aggregated cyanine dyes interacting with a surface plasmon polariton. (b) Reflectometry energy dips as a function of the wavevector. The dashed line is the calculated dispersion relation of an uncoupled SPP. The dotted line is the dispersionless J-aggregated dye exciton energy. In full lines are drawn the calculated energy branches of the strongly coupled system showing a Rabi splitting of $\hbar\Omega = 180$ meV. Image taken from [16].

## 1.2 Motivation and preceding research

### 1.2.1 Coherence length of the strongly coupled system

The coherence of the light emitted by the system described above has been demonstrated by Bellessa's group some years after the observation of strong coupling. Aberra-Guebrou *et al.* [18] showed that the J-aggregates in strong coupling with surface plasmons led to the formation of spatially coherent hybrid states extended on macroscopic distances. They performed a Young-type interferometric experiment, in which a J-aggregated dye layer deposited on a silver film was excited and the coherent emission from different molecular emitters separated by several microns was evidenced. Figure 1.3 (a) shows the experimental setup for coherent measurements in which the interference between signals coming from spatially separated spots can be observed by inserting two Young's slits in an intermediate image plane and refocused at the entrance of a spectrometer. The interference pattern obtained from the strongly coupled system was compared with control samples made of quantum dots weakly coupled to the plasmon, in which the emission from separated observation areas was incoherent, showing no interference pattern. The interference pattern is shown in figure 1.3 (b), which demonstrates the spatial coherence of the extended hybrid states over a distance of 2.8 $\mu$m.

The demonstration of the coherent character of strongly coupled systems opened the possibility to create metasurfaces by structuring the J-aggregate layer at the micron scale. Chevrier *et al.* [19], structured the sample of strongly coupled J-aggregates by photobleaching stripes on the dye layer with a given spatial period. They explored the behavior of the propagating modes varying the spatial period from 5 to 25 $\mu$m. In Figure 1.4(a), the dispersion of an SPP propagating at the interface between a bare silver film and air is shown. Figure 1.4(b) shows the dispersion measured on a silver film coated with a homogeneous layer of J-aggregates. An anticrossing, with a splitting of 155 meV, demonstrates that the system is in strong coupling. A patterned layer with a large period of 25 $\mu$m is shown in Figure 1.4(c). The dispersion shows the coexistence of a continuous line at the exact position of the bare silver plasmon (see Figure 1.4(a) for a comparison) and an anticrossing between two branches with a similar Rabi splitting than in a homogeneous dye layer at the same concentration

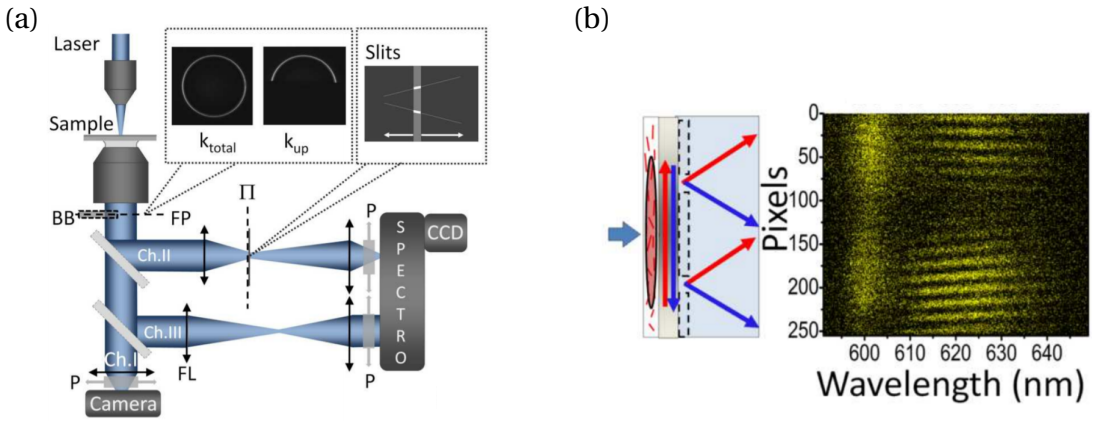


Figure 1.3 – (a) Coherence measurements setup. A direct imaging is performed on the channel I while channel II is devoted to observe the interference pattern coming from two areas of the sample plane by inserting slits in an intermediate image plane of the sample surface. Channel III was used for dispersion measurements, by imaging the Fourier plane of the microscope objective on the entrance slit of the spectrometer. (b) Interference pattern observed for a sample of J-aggregates strongly coupled to SPPs formed at the interface of the dielectric layer and the silver film. The excitation had a size of 0.7 $\mu$m at FWHM and the slits were separated by 2.8 $\mu$m. Images taken from [18].

(as in Figure 1.4(b)). This behavior can be considered as the response of the independent contributions of two distinct regions, with strong and weak plasmon-molecule coupling. In contrast, Figure 1.4(d) shows the dispersion of a patterned layer with a spatial period of 5 $\mu$m, below the coherence length. An effective behavior, showing a reduced Rabi splitting was retrieved while the signature of the bare plasmon is absent. In this study, they concluded that the coherence length of the strongly coupled modes of J-aggregates and SPPs is of the order of $\sim 10\,\mu$m. Notably, another feature of this metasurface is its anisotropy. For the layer with a small pattern period (Figure 1.4(d)), dispersion relations for different propagation directions were recorded. For propagation along the stripes, the dispersion presented a coexistence of bare plasmon and polariton lines, while in the direction perpendicular to the stripes, only polariton lines were recorded.

The extended coherent state of the strongly coupled system appeals to explore the spatial-dependent interactions with other systems. Based on the experiments presented in this section, we explore in Chapter 4 of this manuscript the modifica-

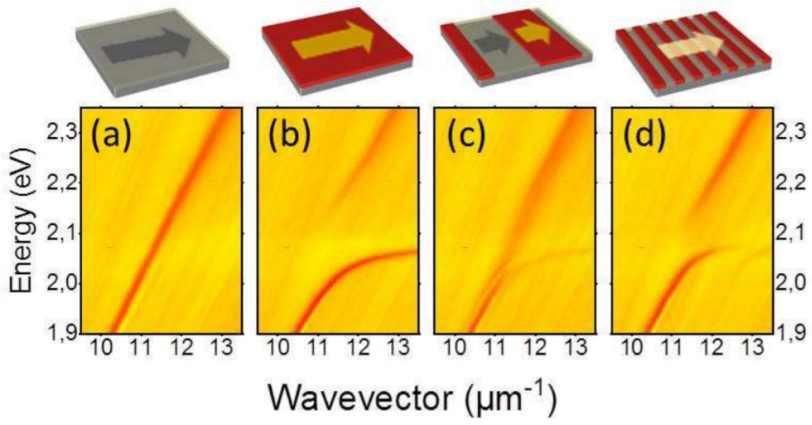


Figure 1.4 – Experimental reflectometry dispersion images of a 50 nm silver film covered by a 17 nm thick dye layer, measured along the propagation direction perpendicular to the stripes: (a) homogeneously UV-irradiated film; (b) homogeneous active dye film; (c) patterned layer with a large period (25 $\mu$m); (d) patterned layer with small period (5 $\mu$m) [19].

tion of the electromagnetic environment produced by the strongly coupled system in areas where the dye has been photobleached. To this aim, we use the same photobleaching technique as in [19] but structuring the J-aggregates layer with a different geometry.

### 1.2.2 Plasmon-assisted energy transfer

The second group of experiments that set the basis for this thesis concerns plasmon-assisted energy transfer between fluorescent emitters. This phenomenon exploits the micron-scale decay length of the SPPs propagation to extend the interaction between fluorophores. Our group at the Institut Langevin demonstrated a great enhancement of energy transfer between a donor/acceptor pair of emitters in the weak coupling regime. In [20], Bouchet *et al.* dispersed large fluorescent beads (100 nm) embedded in a continuous layer of dye molecules were deposited on a silver film. The experiment is shown in Figure 1.5(a) and depicts the focused excitation on a bead, which acts as an energy donor for the surroundings. Surface plasmons propagate, and the plasmon-assisted energy transfer can be characterized by separating the detection from the laser pump. In this case, the energy transfer was observed up to distances of 7 $\mu$m between the pump and the probe.

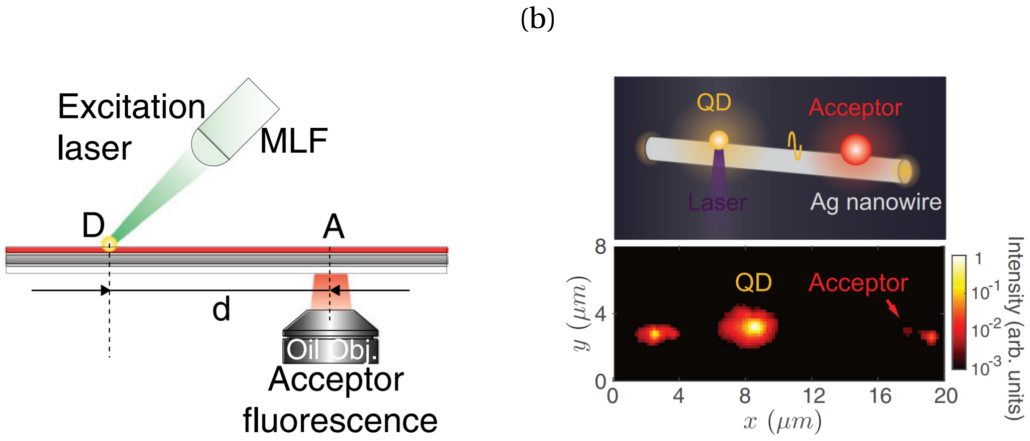


Figure 1.5 – (a) Scheme of the experimental setup to observe an energy transfer between a fluorescent bead (D, donor), excited by a microlensed fiber (MLF), and exciting the acceptors A in the surroundings through surface plasmons polaritons. Image taken from [20] (b) Top: Sketch of the experiment showing a single quantum dot and a fluorescent bead coupled to a silver nanowire. The quantum dot is excited and acts as the donor of the energy transfer process. Bottom: Electron multiplying CCD (EM-CCD) acquisition taken during the experiment, while the laser is focused on the QD. Bright spots are detected at the position of both emitters as well as both ends of the nanowire. Image taken from [21].

In a second experiment [21], Bouchet *et al.* reported plasmon-assisted energy transfer between a single quantum dot and a fluorescent bead coupled to a nanowire. A sketch of the experiment, together with an image of the system's luminescence, is shown in Figure 1.5. Notably, they observed that the dye molecules inside the acceptor bead showed the same blinking behavior as the quantum dot. This is a demonstration that the two emitters are interacting via the single plasmon that is launched by the quantum dot and propagates along the silver nanowire.

In the experiments presented in this thesis, we drew our attention towards energy transfer effects as well. In Chapter 4 we studied them for continuous layers of emitters and in Chapter 5 for spatially separated dyes. The possibility of reducing the concentration of molecules to the single-emitter level is left as a future perspective for this work.

## 1.3 Objectives of the thesis and potential impact

This thesis aims to characterize the interaction between different species of fluorescent emitters in an environment supporting SPPs. We study structured multilayer samples to exploit the coherence extension of strongly coupled J-aggregates and the long-range propagation of the SPPs. We explore two different systems: the first consists of samples in which we probe the interaction of quantum dots with the strongly coupled J-aggregates/SPP. The second corresponds to two J-aggregated dyes that are spatially separated between them and simultaneously hybridized with the SPP.

The first experiment is presented in Chapter 4. We designed a sample to investigate the electromagnetic environment created by the strongly coupled J-aggregates by probing the extended spatial coherence of this system with semiconductor quantum dots deposited in an additional layer. Mixing materials of different nature, as the inorganic semiconductor quantum dots, with the organic J-aggregates, could open the possibility to exploit the properties of these distinct emitters. On the one hand, organic materials as the J-aggregates show a large absorption cross-section, high oscillator strength, and thus strong light-matter interaction. On the other hand, inorganic materials, such as the quantum dots, are photostable, have enhanced optical nonlinearity, and have high electrical conductivity, which remains a crucial feature for electrical pumping, in the view of integrating fluorescent emitters into electronic devices [22]. In order to unify these characteristics into one system, we studied the interaction between this two different kinds of emitters and aimed to characterize energy transfer from one to the other in a plasmonic medium. To explore the effects of the strongly coupled system on the quantum dots, we performed an optical lithography on the J-aggregates layer creating photobleached zones of different sizes. In such a system, we search to explore the effects of the extended coherence explained in subsection 1.2.1 combined with the long-range energy transfer between different emitters presented in subsection 1.2.2. Since the quantum dots weakly couple to the SPP, we use them to measure the modification of their spectrum, emission pattern, and decay rate due to the presence of strongly coupled systems. By observing the luminescence of the system in such areas, we can characterize the non-local effects of the hybridization between the dye and the SPP.

The second experiment performed during this thesis is presented in Chapter 5.

We proposed a sample in which two species of J-aggregates enter in strong coupling with the SPP while they are spatially separated. The optical properties of such a system are mediated by the interplay between the mode's hybridization and the energy transfer between its elements. We aimed to characterize the extension of the energy transfer process, assisted by the hybrid modes propagating in this system. Plasmon-assisted energy transfer in strong coupling could lead to a distance increase of three orders of magnitude compared to Förster processes associated with direct dipole-dipole interactions (limited to a range of a few nm). This enhancement of the interaction, in turn, could lead to non-local switching, which represents a way of modulating light remotely: an excited material (optically or electrically) could modulate the behavior of a second material separated at the micron scale. Also, since analogous configurations have been explored in microcavities [23–25], it will be interesting to compare phenomena such as the relaxation between hybrid states and the spatial extension of energy transfer in both systems. For example, in a study published this year [25], energy transfer at a distance of to 2 $\mu$m between two J-aggregate cyanine dyes contained in a microcavity was reported. Finally, we precise that energy transfer mediated by plasmon/exciton modes could be favored in a plasmonic environment by a proper design of the sample's structure.

# References


[1] E. M. Purcell, H. C. Torrey, and R. V. Pound, *Physical review* **69**, 37 (1946). 6

[2] K. Drexhage, *Journal of luminescence* **1**, 693–701 (1970). 6

[3] P. Goy, J. M. Raimond, M. Gross, and S. Haroche, *Phys. Rev. Lett.* **50**, 1903–1906 (1983). 6

[4] Y. Kaluzny, P. Goy, M. Gross, J. Raimond, and S. Haroche, *Physical review letters* **51**, 1175 (1983).

[5] D. Meschede, H. Walther, and G. Müller, *Phys. Rev. Lett.* **54**, 551–554 (1985). 6

[6] M. G. Raizen, R. J. Thompson, R. J. Brecha, H. J. Kimble, and H. J. Carmichael, *Phys. Rev. Lett.* **63**, 240–243 (1989). 6

[7] Y. Zhu, D. J. Gauthier, S. E. Morin, Q. Wu, H. J. Carmichael, and T. W. Mossberg, *Phys. Rev. Lett.* **64**, 2499–2502 (1990).

[8] G. Rempe, R. J. Thompson, R. J. Brecha, W. D. Lee, and H. J. Kimble, *Phys. Rev. Lett.* **67**, 1727–1730 (1991). 6

[9] R. J. Thompson, G. Rempe, and H. J. Kimble, *Phys. Rev. Lett.* **68**, 1132–1135 (1992). 6

[10] C. Weisbuch, M. Nishioka, A. Ishikawa, and Y. Arakawa, *Phys. Rev. Lett.* **69**, 3314–3317 (1993). 6

[11] M. S. Skolnick, T. A. Fisher, and D. M. Whittaker, *Semiconductor Science and Technology* **13**, 645–669 (1998). 7

[12] D. G. Lidzey, D. Bradley, M. S. Skolnick, T. Virgili, S. Walker, and D. Whittaker, *Nature* **395**, 53–55 (1998). 7, 8

[13] D. G. Lidzey, D. Bradley, T. Virgili, A. Armitage, M. S. Skolnick, and S. Walker, *Phys. Rev. Lett.* **82**, 3316–3319 (1999). 7

[14] P. Törmä and W. L. Barnes, *Reports on Progress in Physics* **78**, 013901 (2014). 7

[15] I. Pockrand, A. Brillante, and D. Möbius, *The Journal of Chemical Physics* **77**, 6289–6295 (1982). 7

[16] J. Bellessa, C. Bonnand, J. C. Plenet, and J. Mugnier, *Phys. Rev. Lett.* **93**, 036404 (2004). 7, 8

[17] V. M. Agranovich, M. Litinskaia, and D. G. Lidzey, *Physical Review B* **67**, 085311 (2003). 7

[18] S. Aberra Guebrou, C. Symonds, E. Homeyer, J. C. Plenet, Y. N. Gartstein, V. M. Agranovich, and J. Bellessa, *Phys. Rev. Lett.* **108**, 066401 (2012). 9, 10

[19] K. Chevrier, J. M. Benoit, C. Symonds, S. K. Saikin, J. Yuen-Zhou, and J. Bellessa, *Phys. Rev. Lett.* **122**, 173902 (2019). 9, 11

[20] D. Bouchet, D. Cao, R. Carminati, Y. De Wilde, and V. Krachmalnicoff, *Phys. Rev. Lett.* **116**, 037401 (2016). 11, 12

[21] D. Bouchet, E. Lhuillier, S. Ithurria, A. Gulinatti, I. Rech, R. Carminati, Y. De Wilde, and V. Krachmalnicoff, *Phys. Rev. A* **95** (2017). 12

[22] V. Agranovich, Y. N. Gartstein, and M. Litinskaya, *Chemical reviews* **111**, 5179–5214 (2011). 13

[23] D. M. Coles, N. Somaschi, P. Michetti, C. Clark, P. G. Lagoudakis, P. G. Savvidis, and D. G. Lidzey, *Nature materials* **13**, 712–719 (2014). 14

[24] K. Georgiou, P. Michetti, L. Gai, M. Cavazzini, Z. Shen, and D. G. Lidzey, *ACS Photonics* **5**, 258–266 (2018).

[25] K. Georgiou, R. Jayaprakash, A. Othonos, and D. G. Lidzey, *Angewandte Chemie International Edition* (2021). 14

# Chapter 2

# Basic concepts

## Contents

This chapter introduces the coupling mechanism between light and matter in the context of plasmonics. First, we present an analogy to this phenomenon, analyzing two harmonic oscillators coupled together. Then, we consider a simple model for the interaction between a single-mode electromagnetic wave and a radiative emitter. We study the corresponding light-matter Hamiltonian, and we discuss the difference between the interaction's weak and strong coupling regimes.

In the second section, we introduce the properties of surface plasmon polaritons (SPPs) supported at the interface between a metallic film and a dielectric medium. The SPPs field enhancement and its extension at the micron scale are studied for an air/silver interface. In the last part, we briefly compare the properties of silver with those of other metals.

Finally, the third section presents the specific features of strong coupling between SPPs and fluorescent emitters. We study the importance of the emitters' oscillator strength and then center the discussion on the influence of the mode linewidths in the interaction. Finally, we introduce the formalism of the transfer matrix method, which we use to obtain the modes in the system with a multilayer geometry and calculate the strength of the coupling.

## 2.1 Light-Matter Interaction

Inside a medium, light induces additional fields by driving the charges that compose it. The resulting behavior is therefore determined by the superposition of the incident and induced fields. In this section, we study a system in which the two fields are characterized as oscillators able to exchange energy. We start by analyzing two harmonic oscillators that perform this exchange via a coupling spring, while they lose energy towards their surroundings via friction. We use this analogy to approach the distinction between the regimes of weak and strong coupling. Then, we analyze the case of a continuous single-mode electromagnetic wave interacting with a fluorescent emitter, described by a quantized two-level oscillator. After describing the temporal and spectral behavior of the system, we explain the effect of the losses in the strong coupling regime.

### 2.1.1 Coupled Harmonic Oscillators

In this section, we have followed the work in [1] in which coupled harmonic oscillators are studied to discuss the basic properties of strongly coupled systems, as well as the similarities and subtle differences between classical and quantum descriptions of coupled dissipative systems. Let us consider the situation depicted in Figure 2.1 in which two oscillating systems constituted by two bodies of mass $m$ ($m_1 = m_2$) are attached to the walls by springs with stiffness $k_{1,2}$. Both are connected through an additional spring with stiffness $\kappa$.

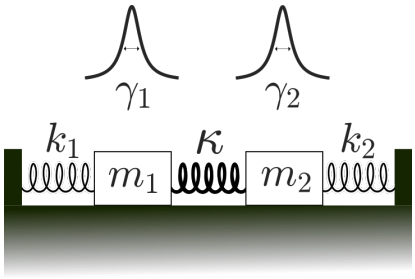


Figure 2.1 – Two spring-mass systems coupled together through the spring with stiffness $\kappa$. Each spring has a stiffness $k_{1,2}$ and the oscillators loss rates due to friction are $\gamma_{1,2}$.

The corresponding equations of motion for the displacement $x_{1,2}$ from the equilibrium position of the oscillators are:

$$\begin{aligned} \ddot{x}_1 - \gamma\,\dot{x}_1 + \omega_1^2\,x_1 + \Omega^2\,(x_1 - x_2) = 0 \\ \ddot{x}_2 - \gamma\,\dot{x}_2 + \omega_2^2\,x_2 + \Omega^2\,(x_2 - x_1) = 0 \end{aligned} \tag{2.1}$$

where $\omega_i = \sqrt{k_i/m}$ is the frequency of an uncoupled oscillator and $\Omega = \sqrt{\kappa/m}$ is defined as the coupling frequency. We are interested in the dynamics of the harmonic doublet. Specifically, we want to establish the normal frequencies of the coupled system in terms of the coupling frequency. We also want to recognize the interplay between energy exchange, driven by the coupling spring, and the dissipative losses of the whole system.

First, we shall calculate $\omega$ in an ideal environment without friction, i.e. $\gamma_1 = \gamma_2 = 0$. By assuming a harmonic solution of the form $x_i = A_i e^{i\omega t}$ for equations in (2.1), we

obtain the matrix form $\mathbb{M}\vec{\mathbf{x}} = 0$, where:

$$\begin{pmatrix} \omega^2 - \tilde{\omega}_1^2 & \Omega^2 \\ \Omega^2 & \omega^2 - \tilde{\omega}_2^2 \end{pmatrix} \begin{pmatrix} x_1 \\ x_2 \end{pmatrix} = \begin{pmatrix} 0 \\ 0 \end{pmatrix} \tag{2.2}$$

where $\tilde{\omega}_i^2 = \omega_i^2 + \Omega^2$ is the angular frequency of each mass considering that the other one remains fixed. We retrieve the solutions by considering $\det(\mathbb{M}) = 0$, resulting in:

$$\omega_\pm^2 = \frac{\tilde{\omega}_1^2 + \tilde{\omega}_2^2}{2} \pm \sqrt{\frac{\Delta^2}{4} + \Omega^4} \tag{2.3}$$

where $\Delta = |\tilde{\omega}_1^2 - \tilde{\omega}_2^2|$ is the difference between the squared frequencies of the uncoupled oscillators.

Figure 2.2 shows the behavior of the solutions as a function of the normalized detuning $\delta = (\tilde{\omega}_2 - \tilde{\omega}_1)/\tilde{\omega}_1$ with a coupling frequency $\Omega^2 = 0.1\,\tilde{\omega}_1^2$. Far from resonance, the solutions converge to the uncoupled frequencies and they repulse each other approaching $\delta = 0$.

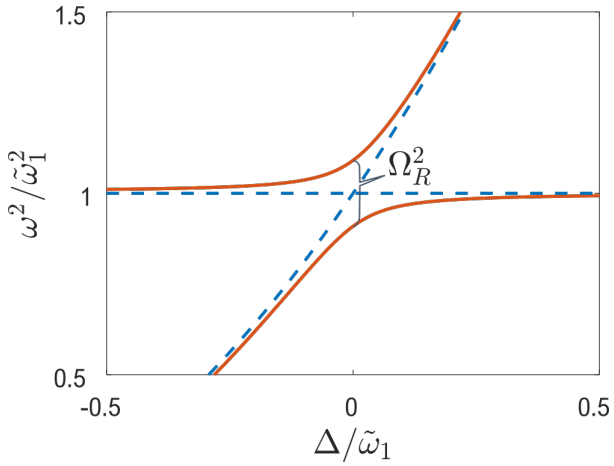


Figure 2.2 – Frequencies of two harmonic oscillators as a function of their detuning. The blue dashed lines show the frequencies of the uncoupled oscillators, and the red curves show the behavior of the eigenfrequencies for the coupled harmonic system. Both axes are normalized by $\tilde{\omega}_1$.

It is observed that the largest effect produced by attaching the two masses occurs when the two harmonic resonators have the same natural frequency. At resonance $\tilde{\omega}_{1,2} = \tilde{\omega}_0$, the solutions show an avoided crossing and are explicitly given by:

$$\omega_{\pm}^2 = \tilde{\omega}_0^2 \pm \Omega^2 \tag{2.4}$$

The difference in the squared eigenfrequencies is $\Omega_R^2 = 2\Omega^2$, where $\Omega_R$ is the Rabi frequency. This magnitude usually characterizes the strength of the coupling for interacting resonators. Later in this chapter, we will discuss how the Rabi splitting is the signature of strong coupling between plasmons and fluorescent emitters.

To study the effects on the damping in our model, we analyze the dynamics of the system at resonance $\omega_{1,2} = \omega_0$, and we give finite values to $\gamma_{1,2} = \gamma$ to solve the set of equations in (1). To study the energy exchange, we consider the following situation: at $t = t_0$, $m_1$ is displaced out of the equilibrium by a given amplitude while $m_2$ remains at rest. As a consequence, the total energy $\mathscr{E}_0$ is concentrated in one oscillator. As time evolves, this energy is distributed to the whole system and also dissipated to the surroundings. To study the behavior of the system, we tune the coupling spring constant $\kappa$ and consider different regimes depending on the value of $\Omega^2/\omega_0\gamma$.

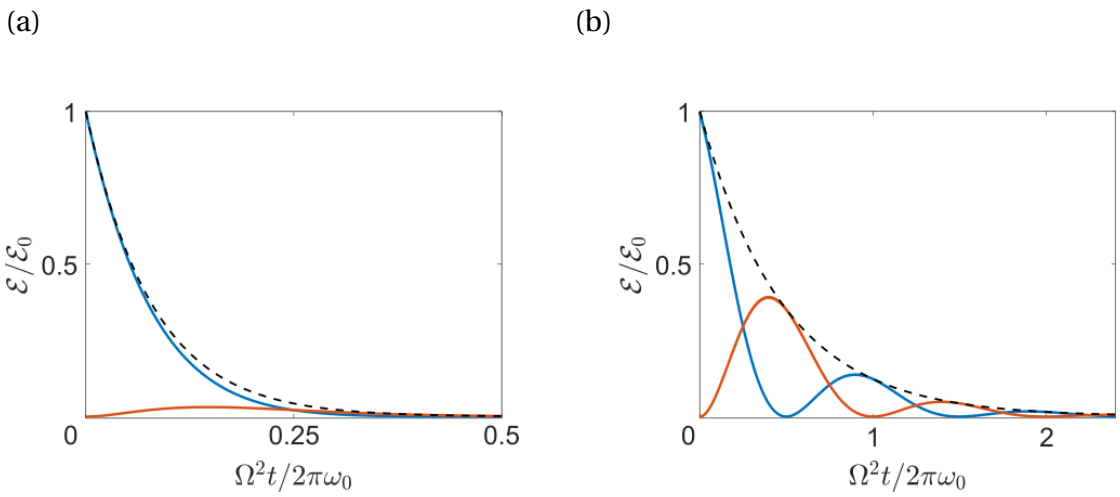


Figure 2.3 – Energy as a function of the dimensionless time parameter $\Omega^2 t/(2\pi\omega_0)$ of two identical harmonic oscillators coupled together. The initial conditions set that oscillator 1 concentrates all the energy (in blue). As time goes on, it is partially distributed to oscillator 2 (in red) while it decays following the exponential black dashed curve. In (a), $\frac{\Omega^2}{\omega_0\gamma} = 0.5$ dissipation prevents a coherent exchange while in (b) $\frac{\Omega^2}{\omega_0\gamma} = 5$, the system's energy oscillates between the two resonators.

Figure 2.3 shows the temporal evolution of the system of the energy normalized

by the energy of a single oscillator with the same amplitude. The normalized energy of the system $\mathscr{E}_0$ and its relaxation towards equilibrium due to the dissipation is observed as a function of the dimensionless time variable $\Omega^2 t/(2\pi\omega_0)$. In figure 2.3a, $\Omega^2/\omega_0\gamma < 1$ dissipation dominates over energy exchange: the initial energy stored in one oscillator is dissipated before it can be transferred to the oscillator. In contrast, figure 2.3b, shows the dynamics for $\Omega^2/\omega_0\gamma > 1$, in which the oscillators exchange the energy $\mathscr{E}(t)$ during multiple cycles in the time-domain before the energy is dissipated. The system's Rabi frequency governs this temporal coherence. In the context of light-matter interaction, this change in the system's global behavior depending on the coupling strength distinguishes two regimes of interaction: the weak and the strong coupling regime.

This classical description captures the physics of oscillating systems coupled together. We can observe that the coupling effect is maximal if the oscillators are resonant. The new solutions of the system are split with respect to the uncoupled counterparts, and this splitting depends on the Rabi frequency. Moreover, the competition between losses and energy exchange is evident, showing a physical criterion to differentiate the weak from the strong coupling regime. Finally, the fact that $\mathbb{M}$ is not diagonal in the position basis of the individual oscillators tells us that it is no longer adequate to describe the system in terms of the two uncoupled oscillators, but we require a new basis with *hybrid modes*. Notably, we worked with the squared frequencies because they are proportional to the total energy of harmonic oscillators, and the analogy holds to a simplified light-matter Hamiltonian presented in the following section.

### 2.1.2 Interaction between a two-level system and the electromagnetic field

In this section, we will show that the results obtained in the classical model with two coupled harmonic oscillators can be transposed to model the interaction of a two-level system with the electromagnetic field of the resonator. We are interested in studying the interaction of an electromagnetic wave capable of exchanging energy with a fluorescent emitter. We consider the system shown in figure 2.4 in which a molecule with a transition dipole moment $\boldsymbol{\mu}$ and an intrinsic linewidth $\gamma_0$ is inside

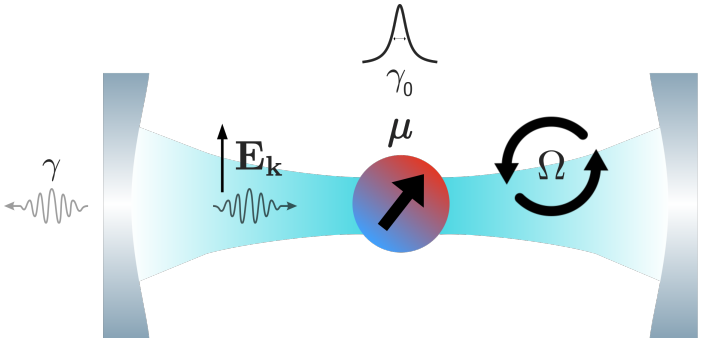


Figure 2.4 – Sketch of a molecule with dipolar moment $\boldsymbol{\mu}$ interacting with an optical cavity that has a resonance for $\mathbf{E_k}$. The strength of the coupling is given by $\Omega$.

an optical resonator supporting a mode $\mathbf{E_k}(t)$ with a damping constant $\gamma$. For simplicity, let us consider a harmonic wave $\mathbf{E_k}(t) = \mathbf{E}_0 \cos(\omega t)$ as the resonator's mode. In the last section, we observed that the distinction between the weak and the strong coupling regime of interaction is mediated by the rate of energy exchange between the coupled oscillators. In the light-matter interaction, the coupling constant

$$\Omega = \boldsymbol{\mu} \cdot \mathbf{E_k} \tag{2.5}$$

determines the exchange rate between the emitter and the field.

First, let us consider the case where the exchange rate is slower than the dephasing of either constituent, i.e. if $\Omega \ll \gamma, \gamma_0$. The damping of the system overcomes the exchange interaction, and the temporal evolution of the system is similar to the one illustrated in figure 2.3a. This regime is known as *weak coupling*, and the energy eigenstates of the system remain unchanged. However, an important effect in the modification of the emitter's excited state lifetime subsists. If the emitter is resonant with the electromagnetic mode, the optical density of states seen by the emitter is increased with respect to the vacuum density of states. Therefore, the spontaneous emission rate is enhanced: the dipole decays radiatively faster than in vacuum, and the photons are emitted in the resonator mode. The relative modification of the spontaneous emission is proportional to the Purcell factor $F_P$:

$$F_p = \frac{3Q(\lambda/n)^3}{4\pi^2 V_{\text{eff}}} \tag{2.6}$$

which is a figure of merit to quantify the influence of the resonator in the spontaneous emission rate. $F_p$ depends only on parameters of the resonator, the quality factor Q, the wavelength of the mode $\lambda$, the refractive index $n$, and its effective volume $V_{\text{eff}}$ which quantifies the field enhancement due to spatial confinement [2].

If $\Omega$ is significantly larger than the characteristic resonance linewidths of the system, the effects of the coupling are dramatically different. In order to analyze the strong coupling regime, let us present a very simplified model in which we consider an emitter with a resonance $\omega_0$ as a two-level system exchanging energy with a single photon of the cavity mode oscillating at a frequency $\omega$. The two-level system undergoes a cycle of emission and re-absorption of the photon. The system oscillates then between the state $|e,0\rangle$ in which the emitter is excited and there are zero photons in the cavity, and the state $|g,1\rangle$ in which the emitter is in its ground state and there is one photon in the cavity. The corresponding Hamiltonian,in the basis $\{|e,0\rangle, |g,1\rangle\}$, reads [3]:

$$\hat{H} = \hbar \begin{pmatrix} \omega_0 & \Omega/2 \\ \Omega/2 & \omega \end{pmatrix} \tag{2.7}$$

If we now diagonalize $\hat{H}$, we see that the new eigenvalues are:

$$\mathscr{E}_{U,L} = \frac{\hbar}{2}(\omega + \omega_0) \pm \frac{\hbar}{2}\Omega_R \tag{2.8}$$

where $\Omega_R = \sqrt{\Omega^2 + \Delta^2}$ is the Rabi frequency and $\Delta = \omega - \omega_0$ is the detuning. We observe that the interaction results in two new hybrid states separated by the Rabi splitting $\hbar\Omega_R$. The solution with the plus sign is associated with the upper polariton branch $\mathscr{E}_U$, and the minus with the lower polariton branch $\mathscr{E}_L$. The term *polariton* refers to the new mixed modes between the photon of the resonator and the excitation from the emitter. At resonance $\Delta = 0$, the energy difference is the *vacuum Rabi splitting* $\hbar\Omega$. The splitting between the two new hybrid modes is the spectral signature of the strong coupling regime.

By taking into account the linewidths of the emitter and the cavity, it is possible to establish a condition to separate the weak from the strong coupling regime. By adding the dephasing terms in eq. 2.7, it is straight-forward to show that the polariton

energies (2.8) become:

$$\mathscr{E}_{U,L} = \frac{\hbar}{2}(\omega + \omega_0) - \frac{i}{2}(\gamma + \gamma_0) \pm \frac{1}{2}\sqrt{\hbar^2\Omega_R^2 - (\gamma_0 - \gamma)^2} \tag{2.9}$$

where the dissipation rates are expressed in energy units [2]. To observe a splitting, the relation between the damping and the Rabi frequency must satisfy $\hbar^2\Omega_R^2 - (\gamma_0 - \gamma)^2 > 0$ so the term in the square root remains positive. This condition seems enough for a system to be in the strong coupling regime; however, the energies $\mathscr{E}_{U,L}$ are complex, and we have to understand them as damped modes with linewidths characterized by $(\gamma_0 + \gamma)/2$. The new normal modes inherit the damping from both the resonator and the emitter. The actual Rabi splitting will be clearly defined only if the real part of the energies is bigger than the widths of the new modes. This implies,

$$\hbar^2\Omega_R^2 > (\gamma_0^2 + \gamma^2)/2 \tag{2.10}$$

which is often taken as an order of magnitude condition [4].

## 2.2 Surface Plasmon Polaritons

In this section, we drive our attention towards the specificities of surface plasmon polaritons (SPPs) as electromagnetic modes. First, we study the conditions for their existence in metal-dielectric interfaces. Then, we examine the dispersion relation, the field confinement and the propagation length of an SPP created at an air/silver interface.

### 2.2.1 Properties of SPPs

A surface plasmon polariton is an electromagnetic surface wave propagating at the interface between dielectric and metallic media. Here, the term polariton points out that this mode is a hybrid wave with energy contributed by two parts. One is the pure electromagnetic field, and the second is the conduction electron sea oscillating in the metal. To study its properties, let us consider the environment shown in figure 2.5a in which a surface wave travels along the $x$ direction at the interface between a semi-infinite metallic plane ($z < 0$) and a semi-infinite dielectric plane ($z > 0$). The

dielectric functions are $\varepsilon_d$ for $z > 0$ and $\varepsilon_m$ for $z < 0$. The metallic character of the bottom half-plane requires $\mathrm{Re}\{\varepsilon_m\} < 0$. We search for a propagating solution of the wave equation at the interface $z = 0$ of the form $\mathbf{E}(x, y, z) = \mathbf{E}(z)e^{ik_{\mathrm{spp}}x}$, with $\mathrm{Re}\{k_{\mathrm{spp}}\} \neq 0$ .

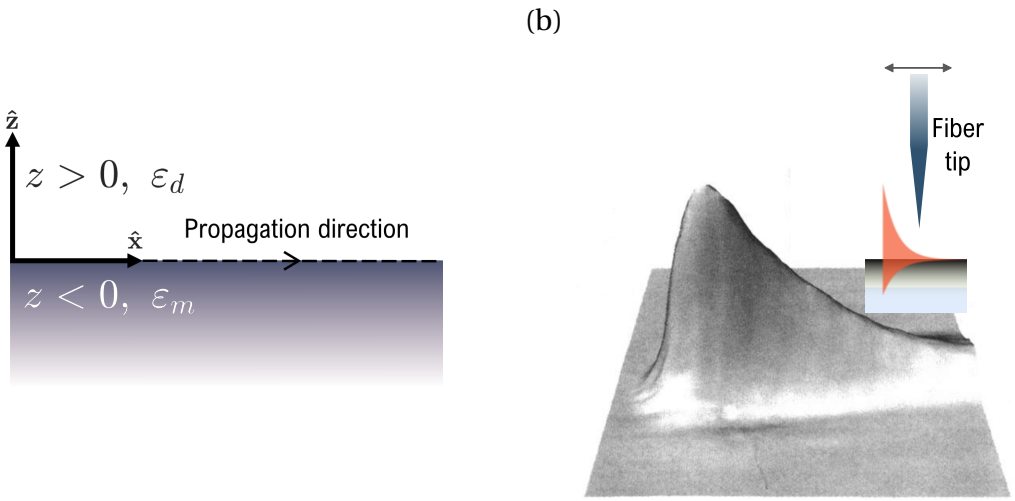


Figure 2.5 – a) Geometry for an interface between two semi-infinite metal and dielectric media. b) Imaging of surface plasmon propagation on a thin silver film using a photon scanning tunneling microscope, which consists on a scanning fiber tip that couples to the evanescent field of the SPP. Image adapted from [5].

By applying the continuity conditions for the electric and magnetic field at the interface, we find out two requirements for the existence of such a mode. First, the real parts of the dielectric permittivities of the media have opposite signs $\mathrm{Re}\{\varepsilon_m\}\mathrm{Re}\{\varepsilon_d\} < 0$, which is generally satisfied by noble metals $\varepsilon_m < 0$ and dielectrics $\varepsilon_d > 0$ in the visible spectrum. The second, is that the surface mode only exists in the *transverse magnetic wave* (TM) polarization in which the electric field has a parallel component to the propagation $x$. For both media, this field is:

$$\begin{aligned} E_{x,d}(z) &= E_{0,d}\, e^{ik_{\mathrm{spp}}x}\, e^{-k_{z,d}z} \quad \text{for } z > 0 \\ E_{x,m}(z) &= E_{0,m}\, e^{ik_{\mathrm{spp}}x}\, e^{k_{z,m}z} \quad \text{for } z < 0 \end{aligned} \tag{2.11}$$

where $E_{0,i}$ is an amplitude depending on the frequency of the field and the permittivity of each medium [6]. The last factor establishes the evanescent decay in the

z-direction for both media. An experimental demonstration of the confinement of an SPP propagating at an air/silver interface is shown in Figure 2.5b, in which the field intensity was probed with a photon scanning tunneling microscope. The evanescent decay length is

$$\tilde{z}_i = k_{z,i}^{-1} = \left[ k_{\text{spp}}^2 - \varepsilon_i \left( \frac{\omega}{c} \right)^2 \right]^{-1/2} \tag{2.12}$$

where $k_{\text{spp}}$ encloses the dispersion relation:

$$k_{\text{spp}}(\omega) = \frac{\omega}{c} \sqrt{\frac{\varepsilon_d \varepsilon_m}{\varepsilon_d + \varepsilon_m}} \tag{2.13}$$

Importantly, metals have significant damping caused by ohmic losses of the electrons driven by the SPP field. Therefore $\varepsilon_m$ is complex, and consequently, the surface plasmon propagation is finite. Explicitly, the intensity of the SPP along a direction $x$ is $I(x,z) = I_0(z) e^{-2\,\text{Im}(k_{\text{spp}})x}$, and the propagation length is

$$\mathscr{L}(\omega) = \frac{1}{2\,\text{Im}\{k_{\text{spp}}(\omega)\}} \tag{2.14}$$

For example, an SPP propagating at an air/silver interface at 445 nm has a propagation length of 13.0 $\mu$m if one assumes that the ohmic losses are the only source of damping. In the reciprocal or wavevector space, the SPP field has a Lorentzian distribution [3; 7] and the dissipation translates into a finite width for the resonance:

$$\begin{aligned} \mathscr{I}(k_x, k_y) &\propto \frac{I_0(k_y, z_0)}{(k_x - k_{\text{spp}})^2 + (\Delta k)^2/4} \\ \Delta k(\omega) &= \frac{2}{\mathscr{L}(\omega)} \end{aligned} \tag{2.15}$$

for an SPP propagating along the $x$ direction.

### 2.2.2 SPP at an air/Ag interface

Let us examine the physical properties of SPPs propagating at an air/silver interface. The dielectric constant of air is $\varepsilon_{\text{air}} = 1$. For the silver permittivity $\varepsilon_{\text{Ag}}$, we obtained the data from the tool PhotonicsDB: Optical Constants [8]. Figure 2.6a shows the

dispersion relation of the SPP and figure 2.6b shows the extension of the evanescent field in both media for three wavelengths.

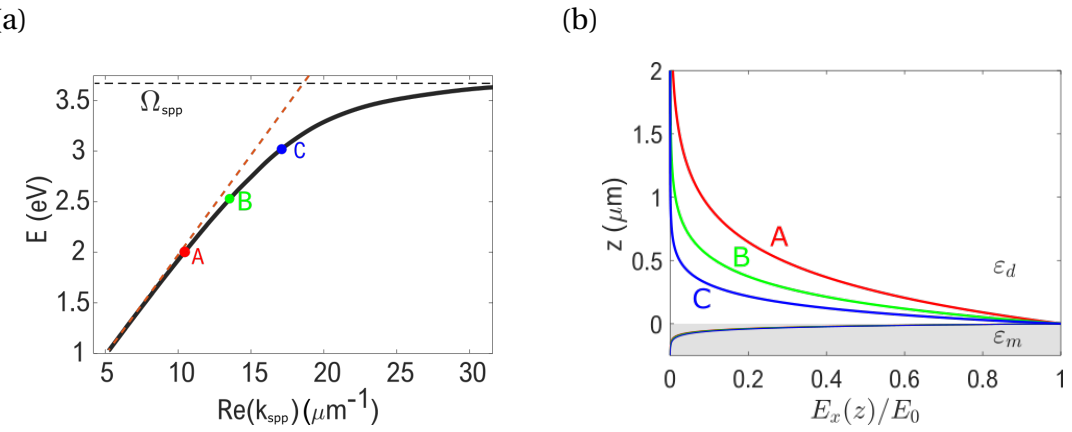


Figure 2.6 – a) Dispersion relation for an SPP propagating at an air/silver interface. The dashed red line indicates the light cone $k = \omega/c$. b) SPP electric field $E_x(z)$ in the propagation direction for the photon energies of points A: 2 eV ($\lambda$ = 619.9 nm), B: 2.5 eV ($\lambda$ = 495.9 nm), and C: 3 eV ($\lambda$ = 413.28 nm). The decay lengths within air (silver) are 400 (23), 232 (24), and 135 (26) nm, respectively.

First, we can observe the evanescent character of SPPs since their dispersion line lies outside to the right of the light cone in free space, implying that they can't be directly coupled to the far-field. Their excitation and observation through evanescent waves created in a medium with a higher refractive index than air are detailed in the next chapter. Second, we can notice that the dispersion relation is close to the light cone for low frequencies. In figure 2.6b, we can observe that in this range, the SPP penetrates more inside the dielectric medium (curve A) than for higher frequencies. We can also tell that the penetration depth inside the metal does not depend strongly on the frequency.

At high frequencies, the field has higher confinement near the dielectric. In this range, the dispersion approaches asymptotically to the characteristic SPP frequency $\Omega_{spp}$. The bending of the curve determines the group velocity $v_g = \partial\omega/\partial k$ of the surface wave. Since the group velocity is proportional to the Poynting vector, the total energy flux and, therefore the propagation, tend to zero near $\Omega_{spp}$. As shown in figure 2.7a, the SPP propagation varies between a few to near one hundred microns long the

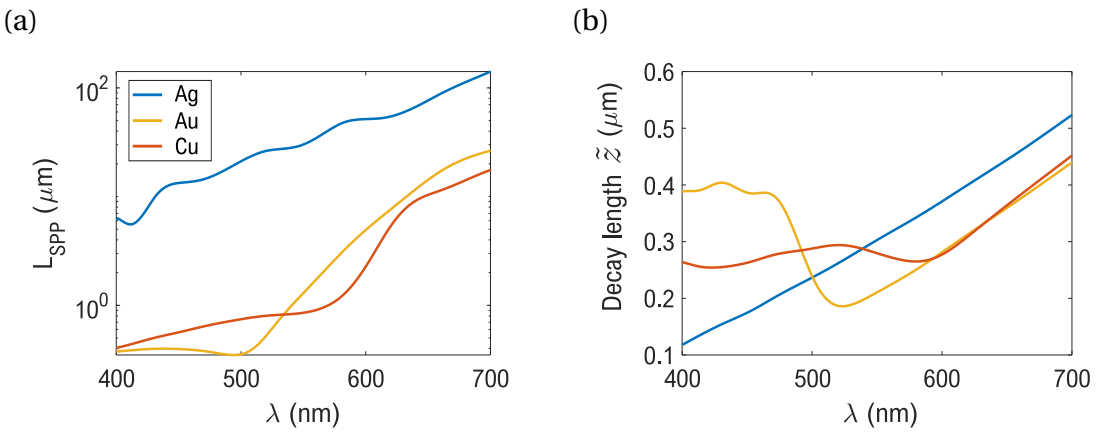


Figure 2.7 – Comparison of the a) propagation length and b) evanescent decay length of a surface plasmon polariton propagating at the interface between air and silver (blue), gold (yellow) and copper (orange).

visible spectrum.

Figure 2.7 shows the propagation length and the evanescent decay length as a function of wavelength for several metals. As it can be seen, the difference of propagation length comparing silver with gold and copper is of one order magnitude. Figure 2.7b shows that the confinement in $z$ in air is of the same order of magnitude for all three. For this reason, we use thin layers of silver to exploit the large propagation length of the SPPs while maintaining high field confinement in the vicinity of the surface. In the next section, we explain a Fresnel approach to calculate the optical properties of surface plasmons propagating in layers of finite thickness.

## 2.3 Strong Coupling with SPPs

Light-matter interactions were vastly developed by studying atoms inside optical cavities. Considering the system's specificities, the results of these studies can be extended to the interaction between an emitter and a plasmonic mode, acting as an optical resonator. As in any cavity, this confined mode can be coupled to other excitations, such as excitons in luminescent materials. Moreover, the sub-wavelength confinement of surface plasmons makes metallic structures suitable environments for strong coupling observation despite their low-quality factor. In this section, we examine the interaction of SPPs with fluorescent emitters, which concerns Chapters 4 and 5 of this thesis. We summarize a macroscopic approach to characterize strong coupling phenomena in thin films through the oscillator strength of the fluorescent transition. Then, we end this chapter by describing how we calculate stratified media's optical response using the Transfer-Matrix Method.

### 2.3.1 Coupling of SPPs and fluorescent emitters

We are interested in the strong coupling between fluorescent emitters that lie on top of a silver film supporting SPPs, and in this section we follow the electromagnetic approach to analyze this phenomenon found in [4]. For the experiments that we realize, we deposit thin films containing the emitters on top of the silver. These are homogeneous dielectric materials where the charges are bound to their respective molecules and cannot flow indefinitely in response to an electric field. We can consider then that particles oscillate around their sites in response to external fields. In this perspective, the luminescent transition is a resonance of the charges at a given $\omega_0$. Under an electric field $\mathbf{E}(t) = E_0\, e^{i\omega t}\hat{\mathbf{x}}$ parallel to the dipole moment of the molecule, we can model the motion of these charges as:

$$m(\ddot{x} + \gamma\dot{x} + \omega_0^2 x) = f e E_0\, e^{i\omega t} \tag{2.16}$$

Where $f$ is the oscillator strength of the transition, and it is considered a quantum correction to a electron elastically bound within a molecule. Specifically, it is

$$f = \frac{2m\, d_{g,e}^2 \omega_0}{\hbar} \tag{2.17}$$

where $m$ is the free electron mass and $d$ is the transition dipole moment between an excited and a ground state, previously described in section 2.1 [9]. The solution of equation 2.16 is given by

$$x = \frac{f\, eE_0 e^{i\omega t}}{m(\omega_0^2 - \omega^2 - i\gamma\omega)} \tag{2.18}$$

The dipole moment associated to the bound electron is a function of time $p = -ex$. We consider the set of relations:

$$\begin{aligned} P &= \frac{N}{V}p \qquad & P &= \frac{fNe^2E_0e^{i\omega t}}{Vm(\omega_0^2 - \omega^2 - i\gamma\omega)} \\ P &= \chi\varepsilon_0 E(t) \qquad & \chi &= \frac{fNe^2}{V\varepsilon_0 m(\omega_0^2 - \omega^2 - i\gamma\omega)} \\ D &= \varepsilon_0 E_0 e^{i\omega t} + P \qquad & D &= \varepsilon E_0 e^{i\omega t} \end{aligned} \tag{2.19}$$

where $N$ is the of number of dipoles parallel to the electric field in the medium, and $V$ is the volume affected by such a field mode. Then, the permittivity of the dielectric medium is:

$$\varepsilon_d = 1 + \frac{Ne^2}{V\varepsilon_0 m}\frac{f}{(\omega_0^2 - \omega^2 - i\gamma\omega)} \tag{2.20}$$

which shows a Lorentzian shape. By setting $A = Ne^2 f / V\varepsilon_0 m$, and adding a background dielectric constant $\varepsilon_b$ [3], we obtain

$$\varepsilon_d = \varepsilon_b + \frac{A}{(\omega_0^2 - \omega^2 - i\gamma\omega)} = \varepsilon_b + \varepsilon_L \tag{2.21}$$

Usually, the constant $A$ is referred as a generalized oscillator strength of the whole medium showing a Lorentzian permittivity [10]. This simplifies the consideration of properties such as concentration, effective mass and charges corresponding to a transition.

In a macroscopic approach, we can insert the permittivity in eq. 2.21 in the dispersion relation in (2.13) for the dielectric medium and observe the effect on the frequency:

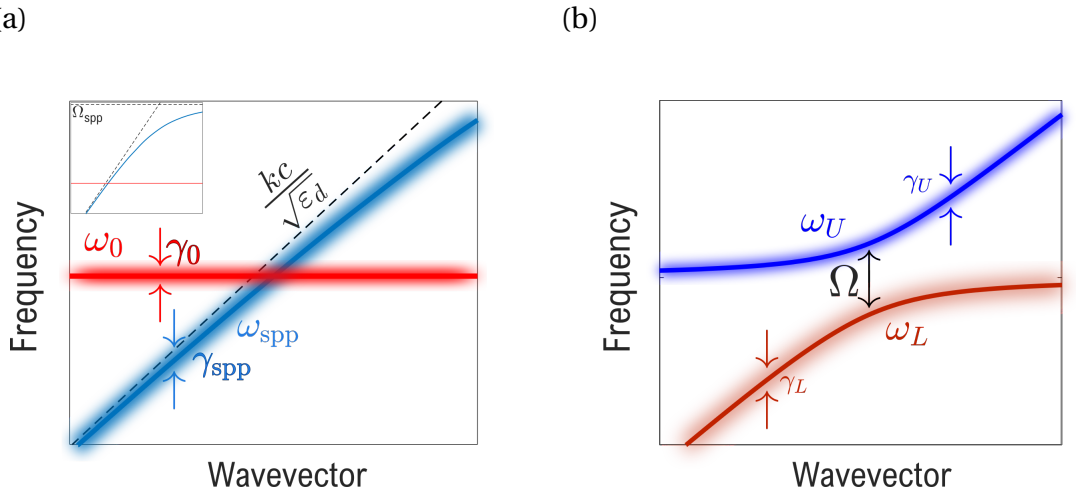


Figure 2.8 – a) Dispersion relation for the uncoupled emitter $\omega_0$ and the SPP $\omega_{spp}$ with their respective linewidths. The inset shows that the coupling is at a frequency far from the SPP resonance, and the dashed blue line the projection of the light cone in the dielectric medium. b) Coupled system showing the Upper and Lower Polariton branches $\omega_{U,L}$ split by the Rabi frequency $\Omega$ with their new respective linewidths $\gamma_{U,L}$.

$$\omega = kc\sqrt{\frac{\varepsilon_m + \varepsilon_b + \varepsilon_L}{\varepsilon_m\varepsilon_b + \varepsilon_m\varepsilon_L}} \tag{2.22}$$

where $\varepsilon_L$ is the Lorentzian term of equation (2.21). Developing the last expression, we get at:

$$\omega^2 = k^2c^2\frac{\varepsilon_m + \varepsilon_b}{\varepsilon_m\varepsilon_b} - \frac{k^2c^2}{\varepsilon_b}\frac{\varepsilon_L}{\varepsilon_b + \varepsilon_L} = \omega_{spp}^2 - \omega_d^2\frac{\varepsilon_L}{\varepsilon_b + \varepsilon_L} \tag{2.23}$$

We observe that the first term corresponds to the SPP dispersion in the interface between the metal and a dielectric $\varepsilon_b$. We also observe that $kc/\sqrt{\varepsilon_b} = \omega_d$ is the frequency of light propagating in the dielectric. Now, we assume that the modification of the frequency is small compared to that of the emitters in the dielectric $\omega_0$, and that of the uncoupled SPP $\omega_{spp}$. Moreover, we assume that we are in a range of frequencies far from the frequency of the horizontal asymptote of the SPP dispersion relation $\Omega_{spp}$ (Figure 2.6) so we can consider $\omega \approx \omega_0 \approx \omega_d \approx \omega_{spp}$. The analysis window is illustrated in figure 2.8a. Under these approximations, eq.2.23 can be reduced

to:

$$(\omega - \omega_{\text{spp}})(\omega - \omega_0) = \frac{A}{4\varepsilon_b} \tag{2.24}$$

By solving for $\omega$ and multiplying by $\hbar$,

$$E_{U,L} = \frac{\hbar}{2}(\omega_{\text{spp}} + \omega_0) \pm \frac{\hbar}{2}\sqrt{(\omega_{\text{spp}} - \omega_0)^2 + \frac{A}{\varepsilon_b}} \tag{2.25}$$

we obtain an expression identical to (2.8) for the upper and lower polaritonic branches. The anticrossing of the SPP and the Lorentzian emitter is illustrated in figure 2.8b.

With this approach, we observe that the strong coupling behavior can be retrieved through Maxwell's equations, and the information of the coupling is contained in the refractive index $n = \sqrt{\varepsilon_d}$ of the dielectric medium. Namely, the vacuum Rabi frequency is determined by:

$$\Omega = \sqrt{\frac{A}{\varepsilon_b}} = \sqrt{\frac{Ne^2 f}{V\varepsilon_0 \varepsilon_b m}} \tag{2.26}$$

We observe that the coupling depends on the intrinsic properties of the medium. In the context of thin films, we can experimentally tune some of these properties. Usually, an optically active layer is made of a polymer matrix containing the active emitters. In this way, the dependence scaling with $\sqrt{N}$ opens an additional degree of freedom since the concentration of the emitters can be modified. Additionally, it is possible to deactivate the fluorescence of molecules through lithography techniques, as detailed in chapter 3. Also, the background permittivity $\varepsilon_b$ can be tuned by controlling the polymer concentration in the film.

Up to this point, we have neglected dissipation in this section. To retrieve expression (2.9), it is necessary to include the imaginary terms in the permittivities. Figure 2.8 sketches the linewidths of the frequencies of the uncoupled and coupled systems.

Regarding the fluorescent emitter, the linewidth $\gamma_0$ is an intrinsic property of the molecule at a given temperature. However, if the luminescent material is composed of many emitters that are not identical, the different linewidths can broaden the total mode corresponding to the material. This effect is called inhomogeneous broadening. Typical values for $\gamma_0^{-1}$ vary from the pico to the nanosecond range.

In contrast, the linewidth of the SPP depends on several factors. An ideal surface plasmon loses energy due to the absorbing character of the metal ($\mathrm{Im}\{\varepsilon_m\} > 0$), which tells us that the motion of the electrons partially dissipates into heat giving rise to ohmic losses. Additionally, properties of the surface, as roughness and oxidation, contribute to the diffusion of energy out of the plasmon. Considering these factors, the values of $\gamma_{\mathrm{spp}}$ are of the order of tens of femtoseconds [11] so that the observation of Rabi oscillations in exciton-plasmon coupled environments requires pump-probe spectroscopy with femtosecond pulses, as in [12].

### 2.3.2 Transfer-Matrix Method

In the previous section, we considered the dispersion of an SPP propagating at the interface of two semi-infinite media, characterized by their dielectric constants. In section 2.2, we observed that the penetration of the field in the metal side is limited to $\sim 20\,\mathrm{nm}$ so this medium can be safely approximated to semi-infinite regions even for thin films. Contrarily, the decay length of the field in the dielectric extends over hundreds of nanometers. We can choose an effective permittivity for this region, averaging the material's properties with the immersion medium (e.g., air). However, an exact optical response of thin-film multilayers can be evaluated by calculating the Fresnel coefficients in a $2 \times 2$ matrix configuration. This approach is called the Transfer-Matrix Method (TMM), and we will summarize its results in the following, based on the derivation in [13; 14].

We can obtain the electromagnetic modes of the 2D system shown in Figure 2.9 by studying the propagation of a plane wave through it. When monochromatic light couples to a mode, a dip in the reflectance and the transmittance is observed as the in-plane wavevector (angle of incidence $\theta_{\mathrm{inc}}$) is scanned. Let us start considering the system in figure 2.9a consisting of a stratified media with $p$ layers. We shine light $\mathbf{E}_{\mathrm{inc}}, \mathbf{H}_{\mathrm{inc}}$ with a given wavevector and polarization from the medium $n_0$ to our sample, and we are interested on knowing the reflected $\mathbf{E}_{\mathrm{r}}, \mathbf{H}_{\mathrm{r}}$ and the transmitted $\mathbf{E}_{\mathrm{t}}, \mathbf{H}_{\mathrm{t}}$ fields.

Due to the multiple interfaces, there will be infinite reflected rays within every layer. In the transfer-matrix method, we consider one layer at a time and write the overall field accounting for the sum of all contributions at the interfaces $i$ and $i+1$.

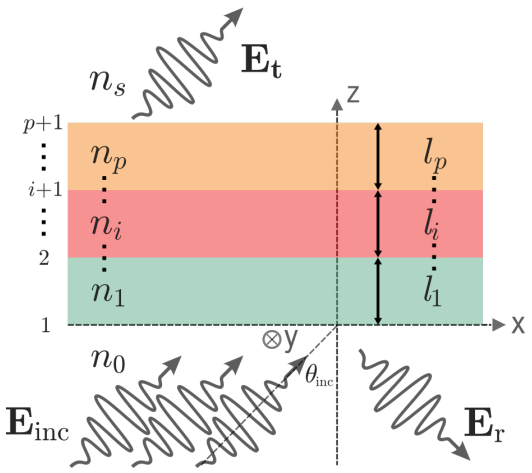


Figure 2.9 – Stratified system composed by $p$ layers and $p+1$ interfaces. Each layer $i$ is characterized by a refractive index $n_i$ and a thickness $l_i$. With the transfer-matrix method we search the reflected field $\mathbf{E}_\mathrm{r}$ by knowing the layers refractive index and the angle of incidence $\theta_\mathrm{inc}$ on the incident field $\mathbf{E}_\mathrm{inc}$.

Moreover, at each interface, we can separate the field in the following way,

$$\mathbf{H}_i = \mathbf{H}_{r,i} + \mathbf{H}_{t,i} \tag{2.27}$$

where the subscripts *r, t* indicate reflected and transmitted field, respectively. For the first medium $i = 1$, the transmitted field is replaced by the incident probe field, and for the last one $i = p+1$, there is no reflected field.

Acknowledging that the fields in consecutive interfaces can be related in a matrix form, we have:

$$\begin{pmatrix} \mathbf{E}_i \\ \mathbf{H}_i \end{pmatrix} = \mathscr{M}_i \begin{pmatrix} \mathbf{E}_{i+1} \\ \mathbf{H}_{i+1} \end{pmatrix} \tag{2.28}$$

and so,

$$\begin{pmatrix} \mathbf{E}_{i+1} \\ \mathbf{H}_{i+1} \end{pmatrix} = \mathscr{M}_{i+1} \begin{pmatrix} \mathbf{E}_{i+2} \\ \mathbf{H}_{i+2} \end{pmatrix} \tag{2.29}$$

therefore, it follows that:

$$\begin{pmatrix} \mathbf{E}_1 \\ \mathbf{H}_1 \end{pmatrix} = \mathscr{M}_1 \mathscr{M}_2 .... \mathscr{M}_p \begin{pmatrix} \mathbf{E}_{p+1} \\ \mathbf{H}_{p+1} \end{pmatrix} \tag{2.30}$$

where

$$\mathscr{M} = \mathscr{M}_1 \mathscr{M}_2 .... \mathscr{M}_p = \begin{pmatrix} m_{11} & m_{12} \\ m_{21} & m_{22} \end{pmatrix} \tag{2.31}$$

is the global transfer matrix.

We are specifically interested in the reflectance $R$ and transmission $T$, defined for TM polarization as:

$$R = |r|^2 = \left| \frac{\mathbf{H}_{\mathrm{r},1}}{\mathbf{H}_{\mathrm{inc},1}} \right|^2 , \quad T = \frac{\mathscr{Y}_s}{\mathscr{Y}_0} |t|^2 = \frac{\mathscr{Y}_s}{\mathscr{Y}_0} \left| \frac{\mathbf{H}_{\mathrm{t},p+1}}{\mathbf{H}_{\mathrm{inc},1}} \right|^2 \tag{2.32}$$

where we have set:

$$\begin{aligned} \mathscr{Y}_0 &= \sqrt{\frac{\varepsilon_0}{\mu_0}} n_0 / \cos\theta_{\mathrm{inc},1} \\ \mathscr{Y}_s &= \sqrt{\frac{\varepsilon_0}{\mu_0}} n_s / \cos\theta_{\mathrm{t},p+1} \end{aligned} \tag{2.33}$$

Assuming that the media are non-magnetic, the electric and magnetic fields are related by:

$$\mathbf{H}_i = \sqrt{\frac{\varepsilon_0}{\mu_0}} n_i \hat{\mathbf{k}} \times \mathbf{E}_i \tag{2.34}$$

so we can write

$$\begin{pmatrix} H_{i,1} + H_{r,1} \\ (H_{i,1} - H_{r,1}) \mathscr{Y}_0 \end{pmatrix} = \mathscr{M} \begin{pmatrix} H_{p+1} \\ H_{p+1} \mathscr{Y}_s \end{pmatrix} \tag{2.35}$$

Developing algebraically the last expression, and using (2.32) we obtain:

$$r = \frac{\mathscr{Y}_0 m_{11} + \mathscr{Y}_0 \mathscr{Y}_s m_{12} - m_{21} - \mathscr{Y}_s m_{22}}{\mathscr{Y}_0 m_{11} + \mathscr{Y}_0 \mathscr{Y}_s m_{12} + m_{21} + \mathscr{Y}_s m_{22}} \tag{2.36}$$

$$t = \frac{2\mathscr{Y}_0}{\mathscr{Y}_0 m_{11} + \mathscr{Y}_0 \mathscr{Y}_s m_{12} + m_{21} + \mathscr{Y}_s m_{22}} \tag{2.37}$$

Finally, to find the coefficients $\mathscr{M}$, we exploit the continuity of the tangential components of the electric and magnetic field at the interfaces. We also consider the propagation of the fields within the medium $i$, $\mathbf{E_{i+1}} = \mathbf{E_i} \exp(ik_0 h_i)$ where,

$$h_i = n_i l_i \cos\theta_{\text{inc},i+1} \tag{2.38}$$

Then, the matrix $\mathscr{M}_i$, in the TM polarization,

$$\mathscr{M}_i = \begin{pmatrix} \cos(k_0 h_i) & -\mathscr{Y}_i\, i \sin(k_0 h_i) \\ -i \sin(k_0 h_i)/\mathscr{Y}_i & \cos(k_0 h_i) \end{pmatrix} \tag{2.39}$$

where

$$\mathscr{Y}_i = \sqrt{\frac{\varepsilon_0}{\mu_0}} n_i / \cos\theta_{\text{inc},i+1} \tag{2.40}$$

With this method, we can study strong coupling phenomena by observing the existence of an anticrossing in the reflectance and on the transmission of a stratified media containing at least one metallic layer supporting SPPs at the interface. In the following chapters, we explain how we experimentally measure and control the angle of incidence $\theta_{\text{inc}}$ and the thickness $l$ of each layer. By knowing these parameters, we can use the TMM to compute the dispersion and the Rabi splitting of strongly coupled modes and then compare this computation with experimental results. In Figure 2.10 we show the TMM reflectance calculation for a system composed by a layer with a Lorentzian resonance at $E = 2090\,\text{meV}$ on top of a 50 nm silver film. In Figure 2.10(a) the generalized oscillator strength $A$ was set to zero and the dispersion of an SPP can be observed. In contrast, Figure 2.10(b) shows a strong coupling behavior when setting $A = Ne^2 f / V\varepsilon_0 m = 5.0 \times 10^5$.

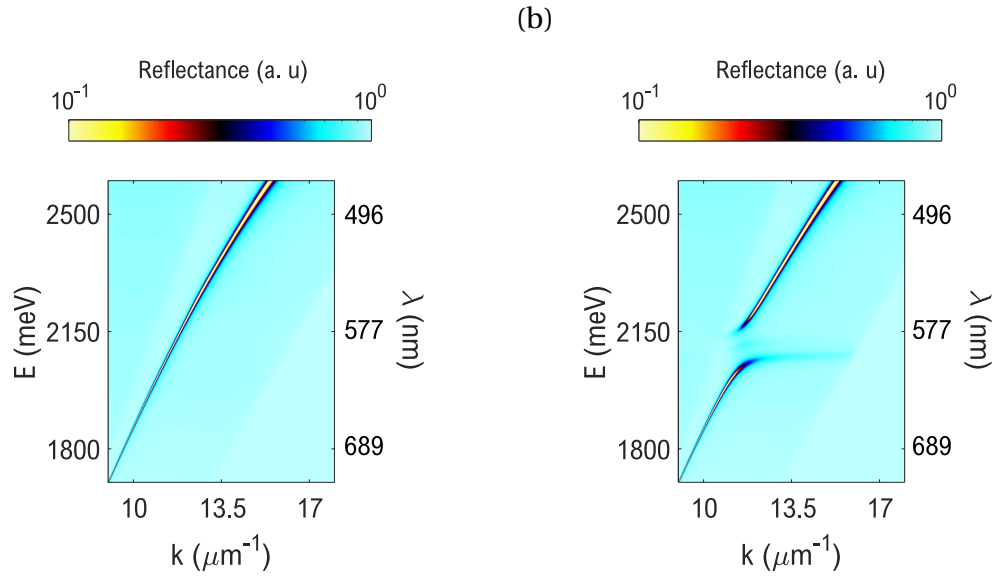


Figure 2.10 – TMM calculated reflectance for a system composed of glass substrate $n_0 = 1.5$, a 50 nm silver thin film and a dielectric layer with thickness $l = 15$ nm and a background refractive index $n_b = 1.72$. In (a) we set the generalized oscillator strength of the dielectric layer to $A = 0$ and in (b) to $A = 5.0 \times 10^5$.

## 2.4 Conclusion

This chapter described the physics related to the coupling between SPPs and fluorescent emitters embedded in a dielectric medium. We observed the coupling mechanism between an electromagnetic mode and a fluorescent emitter inside an optical resonator. Within this interaction, the total dissipation of the system hinders the effects of the coupling. In the strong coupling regime, energy exchange overcomes the losses, and the optical response of the system is characterized by the Rabi oscillations in the time domain and an energy splitting in the spectral domain. In the weak coupling regime, the system's response is characterized by a modification of the emitter's decay rate.

We observed that surface plasmons at the interface between a metal and a dielectric can give rise to strongly enhanced optical near-fields, which are spatially confined near the metal surface to lengths smaller than the diffraction limit. By virtue of this high confinement, they make good candidates the observation of strong coupling phenomena. Specifically, we examined the properties of silver SPPs, which

represent the best compromise between propagation length and field confinement among noble metals.

We observed that classic electromagnetism predicted strong coupling by including the dielectric permittivity of a Lorentzian emitter within the SPP dispersion. A significant result is the dependence of the coupling with the concentration of emitters coupled to the electric field and the emitter's oscillator strength. Moreover, we examined the Transfer-Matrix Method to obtain the reflectance and transmittance of stratified media. Through this method, we calculated the reflectivity of a sample with a Lorentzian transition and we retrieved a strong coupling behavior between SPPs and fluorescent emitters.

# References

[1] S. R.-K. Rodriguez, *European Journal of Physics* **37**, 025802 (2016). 19

[2] A. Kavokin, J. Baumberg, G. Malpuech, and F. Laussy, *Microcavities* (2008). 24, 25

[3] K. Chevrier, *Cohérence dans les systèmes métal/organique en couplage fort états étendus et métasurfaces*, Ph.D. thesis, Université Claude Bernard - Lyon I (2019). 24, 27, 31

[4] P. Törmä and W. L. Barnes, *Reports on Progress in Physics* **78**, 013901 (2014). 25, 30

[5] P. Dawson, F. de Fornel, and J.-P. Goudonnet, *Phys. Rev. Lett.* **72**, 2927–2930 (1994). 26

[6] S. Maier, *Plasmonics: Fundamentals And Applications*, page 245 (2007). 26

[7] J. Grandidier, G. Colas Des Francs, S. Massenot, A. Bouhelier, L. Markey, J.-C. Weeber, C. Finot, and A. Dereux, *Nano Letters* **9**, 2935–2939 (2009). 27

[8] X. Ni, Z. Liu, and A. V. Kildishev, Photonicsdb: Optical constants (2008). 27

[9] G. Grynberg, A. Aspect, and C. Fabre, *Introduction to Quantum Optics: From the Semi-classical Approach to Quantized Light*, Cambridge University Press (2010). 31

[10] I. Shlesinger, H. Monin, J. Moreau, J.-P. Hugonin, M. Dufour, S. Ithurria, B. Vest, and J.-J. Greffet, *ACS photonics* **6**, 2643–2648 (2019). 31

[11] M. van Exter and A. Lagendijk, *Phys. Rev. Lett.* **60**, 49–52 (1988). 34

[12] P. Vasa, W. Wang, R. Pomraenke, M. Lammers, M. Maiuri, C. Manzoni, G. Cerullo, and C. Lienau, *Nature Photonics* **7**, 128–132 (2013). 34

[13] M. Born, E. Wolf, A. B. Bhatia, P. C. Clemmow, D. Gabor, A. R. Stokes, A. M. Taylor, P. A. Wayman, and W. L. Wilcock, *Principles of Optics: Electromagnetic Theory of*

*Propagation, Interference and Diffraction of Light*, Cambridge University Press, 7 edition (1999). 34

[14] E. Hecht, *Optics*, Pearson (2012). 34

# Chapter 3

# Optical Setup

## Contents

This chapter describes the optical setup based on an inverted fluorescence microscope that we have modified to characterize in detail the behavior of fluorophores in plasmonic environments and to study the coupling between them. Our samples consist of multilayered structures with lithographed patterns in the micron scale. To characterize them rigorously, we control the position of the optical excitation and detection by means of a high precision fluorescence microscopy setup. We implemented a detection path to observe the emission in the reciprocal wavevector space to study the propagating modes that arise at the interface between dielectric and metallic media. We complemented the spatial dependence information by measuring fluorescence decay times with a Time-Correlated Single-Photon Counting (TCSPC) module.

In the first part of this chapter, the generalities of the fluorescence microscopy setup that we used for this thesis's experiments are presented. It allowed one to perform local investigations which were complementary to the global studies that had been led by the group of J. Bellessa at ILM before my thesis. The light sources that we use and the optics for shaping the excitation beams are detailed. The microscope objectives are described, and the difference between air-side and substrate-side excitation is discussed. Then, the detection path is outlined, and relevant specifications of the instruments are detailed.

The second part describes the setup for measuring the spectral and temporal response of the sample's fluorescence in the direct space. The precision to aim the excitation and detection to a determined spot on the sample plane is quantitatively presented. We detail the ray tracing of the real-space image from the objective to the detectors. In one detection branch, we perform a spectral analysis of the signal. On the other, we measure the fluorescence decay rate of the emitters employing a single-photon avalanche diode (SPAD). The principle for measuring temporal fluorescence relaxation is summarized. As a perspective for future experiments, a simple setup extension to study single emitters (Hanbury Brown-Twiss configuration) in similar systems is shown.

Finally, the third part of the chapter contains the description of the imaging and spectroscopy of the reciprocal or Fourier space. The angular dependency of the leaky propagating modes carries essential information about the electromagnetic modes in a given environment. By adding a Bertrand lens, we can conveniently switch our

imaging setup from real to reciprocal space and characterize the fluorescent emission as a function of the sample in-plane wavevector. In addition, we included a white light illumination path to perform reflectometry measurements in the Fourier space. In both photoluminescence and reflectometry configurations, we employ similar optical paths that are reported in respective sections.

## 3.1 General Description of the Setup

We performed the experiments presented in this thesis on an inverted microscope (IX83, Olympus) laying on a pneumatically stabilized optical table. In order to properly set the sample plane on the focal plane of the microscope objective, precise control of elements along the optical axis $z$ is necessary. For this, the sample holder is mounted on a linear piezoelectric actuator (SLC-2430, Smaract) with a range of 150 $\mu$m and a resolution of 1 nm in closed-loop mode. Similarly, the transverse XY plane is controlled by an actuator stage (PXY 200, Piezojena System) with a resolution of 0.16 nm on each axis. Light is coupled to the microscope through two ports which allow configuring the excitation and the detection of the sample.

### 3.1.1 Excitation Path

We use different light sources for the excitation depending on the experiment. For fluorescence microscopy, we dispose of a supercontinuum pulsed laser (SuperK Extreme EXB-6, NKT) filtered through a tunable bandpass filter (SuperK VARIA, NKT), a pulsed laser diode at 405 nm (PDL 800-B, PicoQuant), and a continuous laser diode at 532 nm (CPS532, Thorlabs). For reflectometry measurements, we use an incandescent white lamp (EK-1, Euromex).

The excitation path for the laser beams is shown in Figure 3.1, with a specific example for the supercontinuum laser. A non-linear fiber generates a broad spectrum expanding in all the visible range of the electromagnetic spectrum after being pumped with a 1064 nm laser. Then, the laser is filtered at a designed wavelength, and the output has a narrow spectrum of 10 nm of full width at half maximum (FWHM). The fibered output is collimated, and a telescope enlarges the beam to fill the back pupil of the microscope objective. Before entering the microscope, a variable neu-

tral density filter attenuates the beam to avoid photobleaching of the sample fluorophores.

The beam enters the microscope and is reflected by a dichroic mirror mounted on a microscope cube containing a fluorescence filter to block any reflected laser in the detection path. These cubes are exchanged using an automatic turret. Dichroic mirrors are used for lasers and a 50/50 beam splitter for the white lamp.

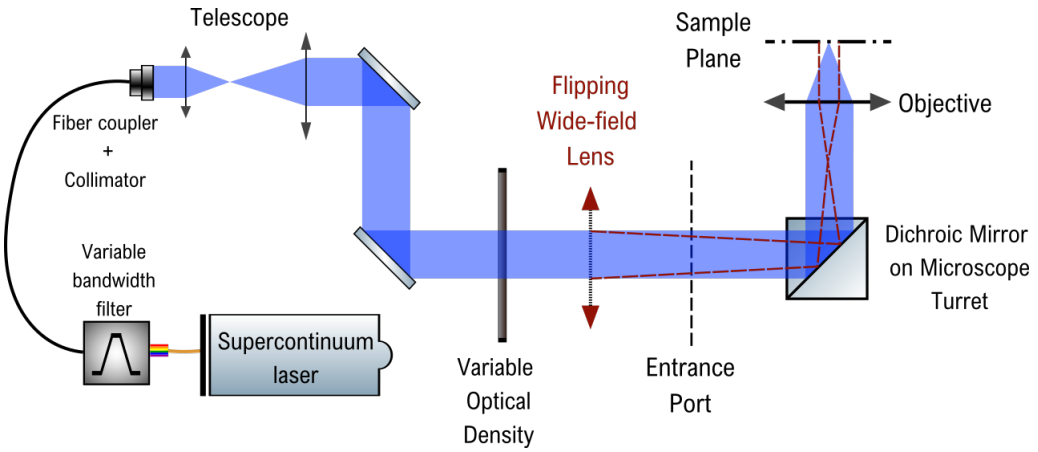


Figure 3.1 – Scheme of the excitation path starting from a supercontinuum laser to the focal plane of a microscope objective. The laser beam is reshaped by a telescope and directed by two mirrors. Then it enters the microscope, where it is focused on the sample plane by the objective. If the wide-field lens is placed, the beam is focused on the objective's back focal plane and sent to infinity as sketched by the red dashed line.

Figure 3.1 shows the ray-tracing for a collimated beam. If it completely fills the objective's pupil, the size of the laser spot at the sample plane will be diffraction limited by $d \sim \lambda/2\text{NA}$, where NA is the nominal numerical aperture of the microscope objective. For a laser excitation of 445 nm and a NA of 1.50, the excitation spot will be $\sim 150$ nm. Contrastingly, to illuminate with a wide-field excitation, we add a flipping lens that focuses the laser on the objective's back focal plane producing a collimated beam after the objective. For our setup, the diameter of wide-field excitation is set to 30 $\mu$m on the sample plane.

The path for the other light sources is similar. The 405 nm diode is set in the same way as the supercontinuum, while the 532 nm diode is not fibered and has a different mount and an incorporated collimator. The fiber of the white lamp is 8 mm in diameter. In order to control the size of the excitation spot, we add a pinhole close to the

fiber output and a collimation lens. In this way, the excitation size corresponds to the pinhole image at the sample plane.

The excitation produced on a sample with a metallic thin film not only depends on the light source but also on the microscope objective. We use an air objective (MPLN100X, Olympus) with a NA = 0.90 and an oil immersion objective (UPLAPO100 XOHR, Olympus) with a NA = 1.50. As previously discussed in Chapter 2, a propagating plasmon does not couple to the far-field of the dielectric medium forming the interface such that the choice of the objective is relevant.

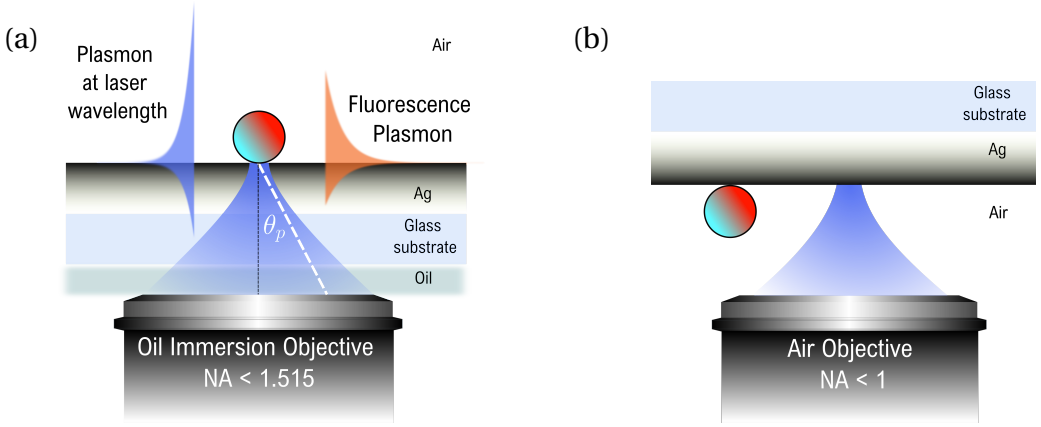


Figure 3.2 – (a) Laser excitation of a fluorescent bead on top of a silver layer through the substrate. An index-matching oil is added between the front lens of the objective and the bottom of the substrate. The laser excites the bead (which launches a surface plasmon) and a surface plasmon at the laser's wavelength by coupling the ray entering at an angle $\theta_p$. (b) By illuminating the surface through the air, there are no plasmons produced at the excitation wavelength.

Figure 3.2(a) depicts the excitation through the oil immersion objective. We consider here the simple example of a sample made of a 100 nm fluorescent bead deposited on a silver film on a glass coverslip. The laser beams focus on the bead through the substrate. It excites the fluorophore, which can couple to a surface plasmon at the fluorescent bead's wavelength or emit in the far-field. A surface plasmon at the laser's wavelength can be excited in two ways: the laser's ray propagating at the angle of the plasmon $\theta_p$ can couple directly to the surface, or the laser light can be scattered by the bead and match the plasmon momentum. In the case of an excitation by the air objective on the air-side of the sample, as shown in Figure 3.2(b), the

laser focuses through the air and, if it does not hit the bead directly, it is unable to excite a plasmon at its wavelength because the phase matching condition cannot be fulfilled.

The choice of the objective also determines the light detection. As explained in section 3.3, we can collect the radiation of the leaky modes with the oil immersion objective, while this is not possible with the air objective. Another difference is that observing the sample through the substrate side involves attenuating the signal, an effect which is particularly pronounced when the silver layer is present, due to the absorption by the metal. On the contrary, the signal collected through the air side is not attenuated.

### 3.1.2 Detection Path

Once the signal goes through the microscope, it is focused by a $f$ = 180 mm tube lens. Inside the microscope, an automatic flipping mirror directs the light through an output port to optics mounted on the optical table or to an EM-CCD (iXon 897, Andor) fixed to the right side of the microscope. The latter has a square chip of 512 x 512 pixels and a quantum efficiency > 95%. It is used mainly for position reference of the excitation. Figure 3.3 shows images of samples taken with room illumination (a) and in wide-field fluorescence (b). The size of each pixel is 16 $\mu$m, which means that the camera chip, with a magnification of $M = 100$, corresponds to a zone of 81.92 $\mu$m × 81.92 $\mu$m in the sample plane.

The detection path on the left side of the microscope is used for spectral and lifetime measurements. The following sections describe the corresponding instruments and ray-tracing in detail. The left and right ports of the microscope are not represented in the schemes of this chapter.

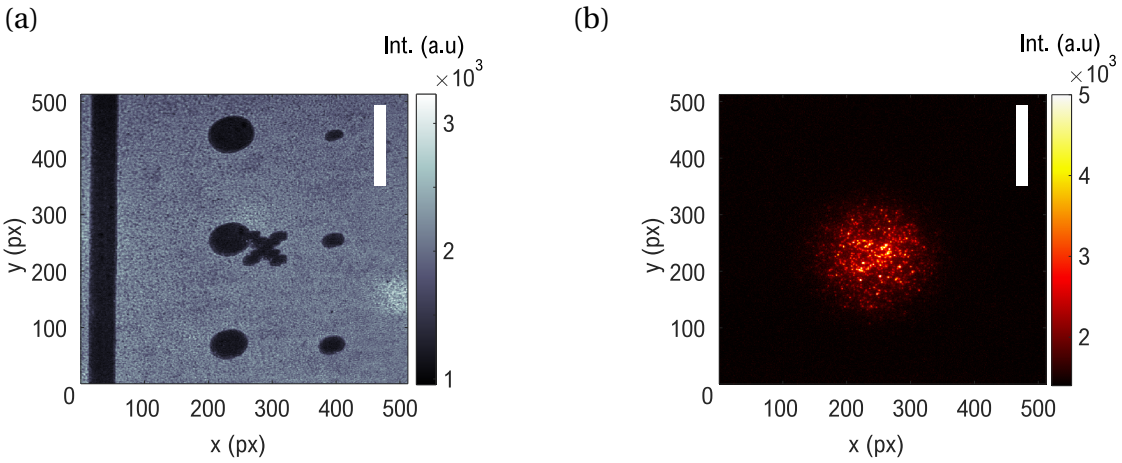


Figure 3.3 – Images taken with the iXon EMCCD camera at the right port of the microscope. (a) Transmission of the room's light of a lithographed dye layer on a thin silver film. (b) Fluorescence of a quantum dot layer deposited on a glass substrate, illuminated by a laser with a wide-field excitation of 30 $\mu$m diameter. The scale bars in the upper right corner of the images represent a length of 20 $\mu$m.

## 3.2 Real-Space Characterization

In this section, we describe the real-space imaging of fluorescence emission on two different detectors. Figure 3.4 shows a scheme of the ray tracing for the fluorescent emission coming from a single point in the sample plane. The microscope tube lens focuses the parallel rays coming from the objective on the EM-CDD camera or, by flipping an internal mirror, to an intermediate image on the left side of the microscope. Then, a relay lens sends the light to infinity, and it is refocused on the detectors. In one branch of the setup, the image coincides with the spectrometer's aperture slit and in the other with an avalanche photodiode. The intermediate direct image allows performing confocal microscopy by placing a pinhole that filters the signal spatially.

### 3.2.1 Spatial-Spectral Imaging

The spectrometer showed in Figure 3.4 consists of a Czerny-Turner spectrograph (Kymera 328i, Andor) equipped with an EM-CCD camera (iXon Ultra 888, Andor) with a square chip of 1024 × 1024 pixels and a pixel size of 13 $\mu$m. The spectro-

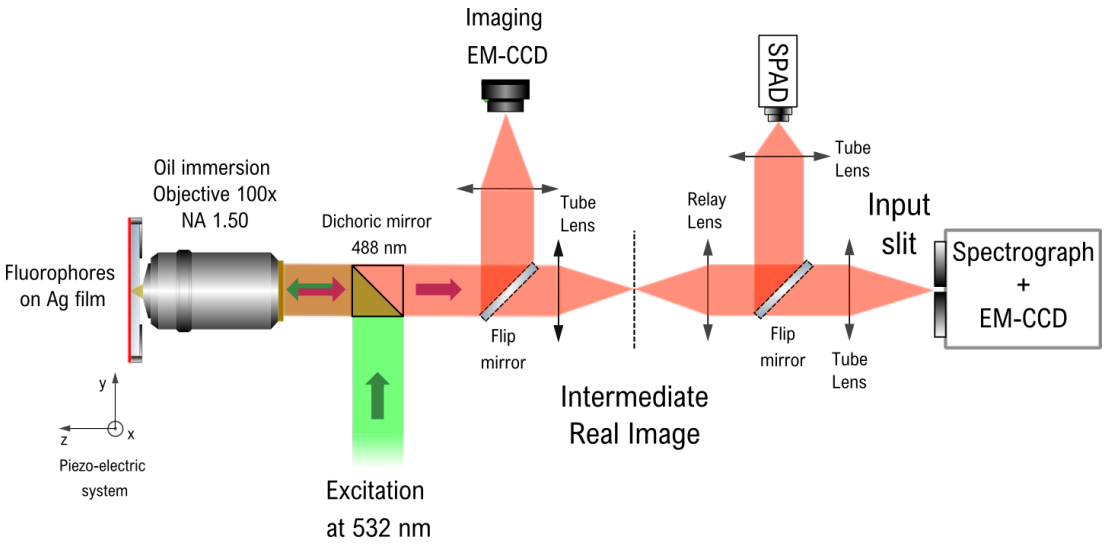


Figure 3.4 – Scheme of the setup and ray-tracing for spectroscopy and lifetime measurements of the real-space image of fluorescent samples. The incoming laser is focused on a determined spot on the sample, which is on a holder controlled by piezo actuators. The emission can be directed to an EM-CCD camera, a single-photon avalanche diode (SPAD), and a spectrometer, made of a spectrograph and an EM-CCD. After the microscope tube lens, on the left side of the microscope, an intermediate image that can be filtered is formed before the last two detectors. For this setup configuration, air and oil immersion objectives can be used.

graph is equipped with two interchangeable blazed gratings, one with 150 lines/mm (spectral bandwidth 545 nm, spectral resolution 0.89 → 0.62 nm) and another with 300 lines/mm (spectral bandwidth 271 nm, spectral resolution 0.41 → 0.33 nm). Also, the input aperture has a motorized slit assembly for controlled spatial filtering of the signal.

The combination of the spectrograph and the square chip of the camera allows the acquisition of large areas of a sample and disperses them in wavelength. Figure 3.5(a) shows the wide-field fluorescence from a structured system, detected with the spectrometer at order 0 with the slit fully opened (2500 $\mu$m). The sample, that will be described in detail in Chapter 5, contains one dye (emission peak at $\lambda \sim 590$ nm) with circular holes, in which pillars composed of another dye (emission peak at $\lambda \sim 625$ nm) are inserted. By closing the slit and centering the grating of 150 lines/mm to 590 nm, the image in Figure 3.5(b) is obtained, and the spectral difference between the dyes is clear. In contrast to spectrometers with narrow rectangular chips, these measurements have the advantage of distinguishing features in direct imaging and

relate them to the spectral distribution.

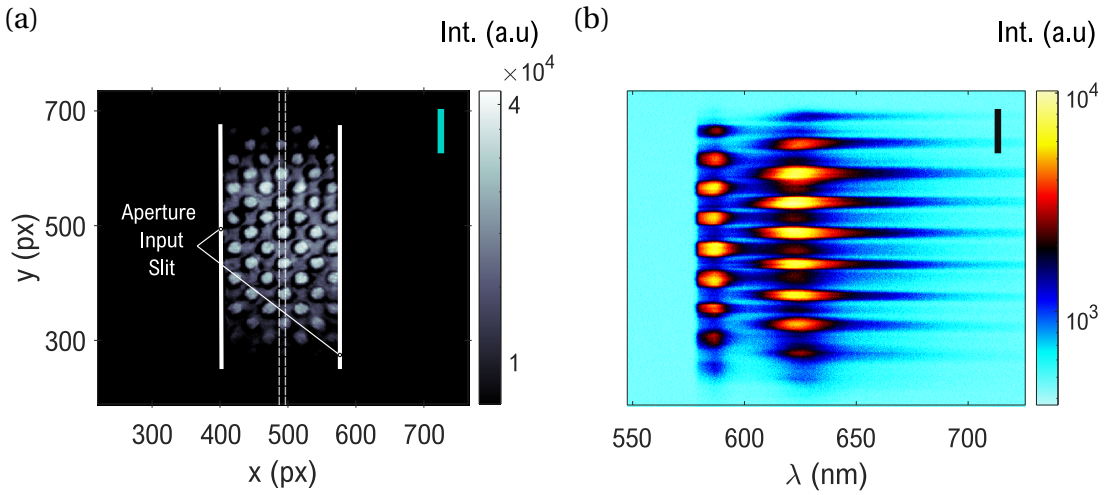


Figure 3.5 – Images of the fluorescence of a structured sample under wide-field excitation. The sample consists of a thin silver film covered by a layer of TDBC with circular holes and micropillars of S2278. (a) The slit of the spectrometer is entirely open, and the micropillars of S2278 are brighter than the TDBC. The dotted white lines show the width of the slit when it is closed (opening width of $\Delta x = 91\,\mu$m) for the spectral measurement. (b) The spectral dispersion shows that one dye emits around 590 nm, and the other is broader, with an emission centered around 625 nm. (a) and (b) have the same spatial vertical scale, and the bars in the upper right corner of the images represent a length of 10 $\mu$m in the sample plane. The study of this sample corresponds to Chapter 5 of this thesis.

For a focused beam excitation, the laser is aligned at the center of the slit. When it is dispersed, the whole image can be integrated to observe the overall spectral response. However, in spatially inhomogeneous environments, an analysis of the spectrum along the slit is more convenient.

For samples supporting surface plasmons or, more generally, polarization-dependent emission, a polarizer can be installed before the spectrometer. Its relative orientation with respect to the slit's axis defines a preferential polarization of observation. In the case of SPPs, a polarizer with an orientation along the slit allows the detection of leaky plasmons traveling in the same direction of the slit while a perpendicular orientation blocks their detection.

### 3.2.2 Time-Correlated Single Photon Counting for Lifetime Measurements

The exchange of energy between an emitter and the environment modifies its fluorescence lifetime. The observation of this modification in the temporal dynamics adds valuable information to understand light-matter interactions. Figure 3.4 shows that the light in the detection path can be directed to a SPAD (Single Photon Avalanche Diode PDM-Red, Micro Photon Devices) with an active area diameter of 50 $\mu$m. The lens in front of the SPAD has a focal length of $f$ = 100 mm. Considering the total magnification, the effective region that the SPAD observes in the sample plane has a diameter of 1 $\mu$m. Still, a pinhole can be added at the intermediate image plane if finer spatial filtering is required. To perform Time-Correlated Single-Photon Counting (TCSPC) measurements, we always excited the sample with a focused beam.

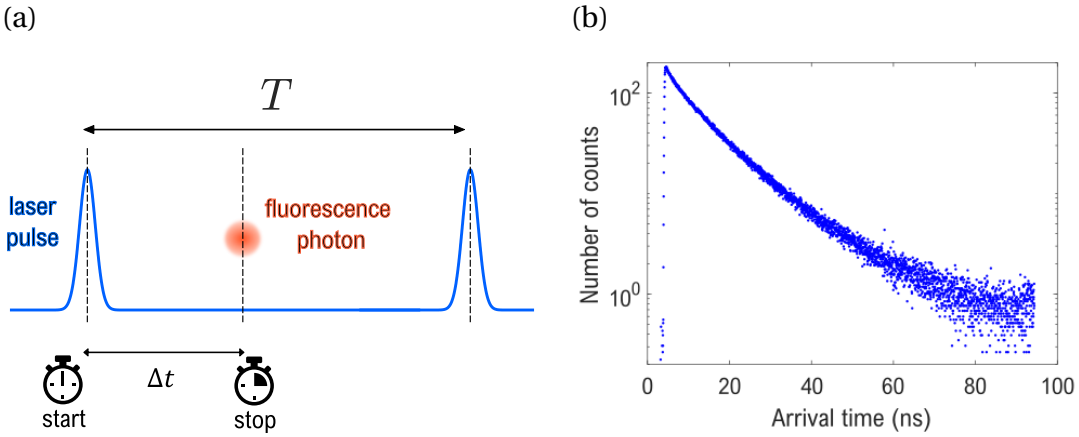


Figure 3.6 – (a) Illustration of a measurement of start-stop times in a time-resolved fluorescence measurement with TCSPC. The laser pulse marks the 'start' time and the fluorescence photon the 'stop' time. There is a time $T$ between each laser pulse. (b) Example of a histogram obtained for the arrival time of the fluorescent photons of a sample of quantum dots. Note that the number of counts is represented on a logarithmic scale.

Lifetime measurements are performed by measuring the duration that a fluorescent emitter passes in its excited state after receiving a pulsed signal from the laser. Each excitation pulse is emitted simultaneously with a logic signal which is used as a reference 'start' time by a time resolved photon counting module (HydraHarp400,

PicoQuant). When a fluorescence photon is detected by the SPAD, a logic signal is emitted. Its arrival time is measured by the TCSPC module and is considered as a 'stop' signal. The delay $\Delta t$ between the start and stop signal is then calculated. Figure 3.6(a) illustrates this process. Then, the histogram of the distribution of the measured delays, as shown in Figure 3.6 (b), is built over a large number of excitation/emission cycles. This histogram contains the probability distribution of the time that the fluorophore spends in its excited state. Considering that the distribution is composed of decaying exponential functions, the system's fluorescent decay rate(s) can be measured using a fitting procedure.

The measured fluorescence decay is the convolution of the physical process of exponential decays with the Instrument Response Function (IRF) of the TCSPC system. The IRF depends on the pulse width of the synchronized laser, the readout of the SPAD, and the time measurement electronics. By measuring the 'true' IRF of the setup, it is possible to enhance the accuracy of the fluorescence decay rate measurements.

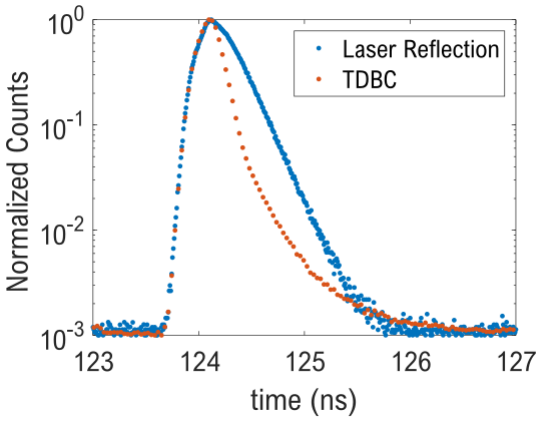


Figure 3.7 – Decay rate histograms for measuring the IRF of the setup. The blue curve was taken by directly collecting the reflection of the laser with the SPAD and has a (FWHM) of 432.8 ps. The red curve was obtained collecting the emission of TDBC dye (590 nm) excited with the same laser wavelength and has a FWHM of 158.6 ps.

Figure 3.7 shows two histograms of the IRF. Since the laser excitation occurs at 445 nm and the pulse duration depends on the selected wavelength, the IRF should be measured at this wavelength. However, the response of the SPAD is wavelength-dependent, as reported in Figure 3.7. The blue histogram is an attempt to measure

the IRF by detecting the reflection of the laser at 445 nm. A 50/50 beam splitter was used in the microscope cube to direct the laser to a silver layer and collect its reflection with the SPAD. The decay histogram gives then an IRF whose width is apparently ~ 430 ps at its FWHM*. The red histogram was obtained by exciting with the 445 nm laser a layer of aggregated TDBC and has a FWHM~ 160 ps. The difference between these two histograms arises mainly due to a chromatic response of the solid-state sensor of the SPAD. Since the TDBC lifetime (~ 15 ps, [1]) is significantly smaller than the pulse duration (specified pulse temporal width of ~ 90 ps), it is reasonable to use the red histogram as the IRF, which takes into account the chromatic response of the SPAD at the wavelength detected in all experiments presented in the manuscript.

The strongly coupled systems that we study include TDBC and a metallic resonator. Considering that the anticrossings that we expect are of the order of hundreds of meV, the corresponding Rabi oscillations have periods in the femtosecond timescale. Since our IRF is several orders of magnitude above this value, Rabi oscillations cannot be observed by TCSPC measurements. In our case, TCSPC measurements are a tool used to observe the interaction of quantum dots with their environment.

#### Hanbury Brown and Twiss detection setup

As a perspective for future experiments, including systems with single emitters, the Hanbury Brown and Twiss (HBT) configuration for the setup is explained. A single quantum emitter is characterized by a vanishing probability for the emission of two photons at the same time [2]. Its single-photon emission can be probed by using two SPADs in the HBT configuration, depicted in Figure 3.8(a), and its implementation in the setup of Figure 3.4 is straightforward.

*The FWHM of the curves shown in Figure 3.7 in semi-logarithmic plot is the difference between the two values of time at which the number of counts is equal to half of its maximum value.

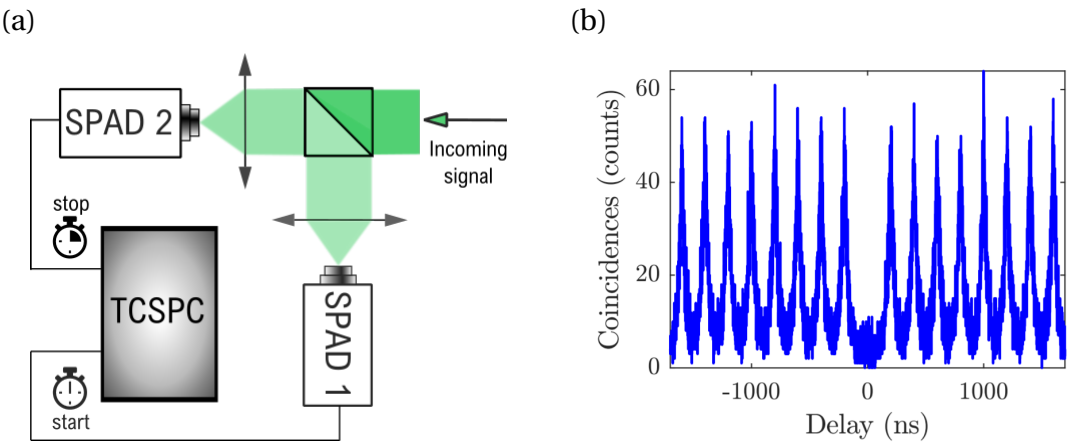


Figure 3.8 – (a) Hanbury Brown and Twiss (HBT) detection setup. The incoming signal is divided to two SPADs via a beam-splitter. The start-stop operation of the TCSPC module is determined by the delay between both detectors. (b) Histogram obtained with the HBT setup on single quantum dots [3].

Fluorescent photons impinge on a 50/50 beam splitter and are detected by the two SPADs. If the emitter emits only one photon at a given time, the two detectors cannot detect the photon simultaneously. It follows that the detection correlation between the two SPADs at zero delay will be zero. This effect is called *photon anti-bunching*. For delays longer than zero, the value of the correlation will go up and will reach its maximum value for a time equal to the period of the pulsed laser as the example shown in Figure 3.8(b), which has been obtained on single quantum dots. The temporal width of the peak is related to the lifetime of the emitter.

## 3.3 Reciprocal-Space Spectroscopy

The dispersive nature of surface plasmon polaritons requires studying the angular distribution of the emitted radiation from a plasmonic sample. Figure 3.9(a) shows the in-plane wavevector dispersion of a propagating surface plasmon on an air/silver interface. SPPs are mixed quasi-particles traveling as electromagnetic waves in the dielectric while driving the electrons on the metallic surface. For this reason, surface plasmons need additional momentum compared to pure light waves in the dielectric medium and, for a given frequency, the SPP momentum is always larger than the one

from the light line in air.

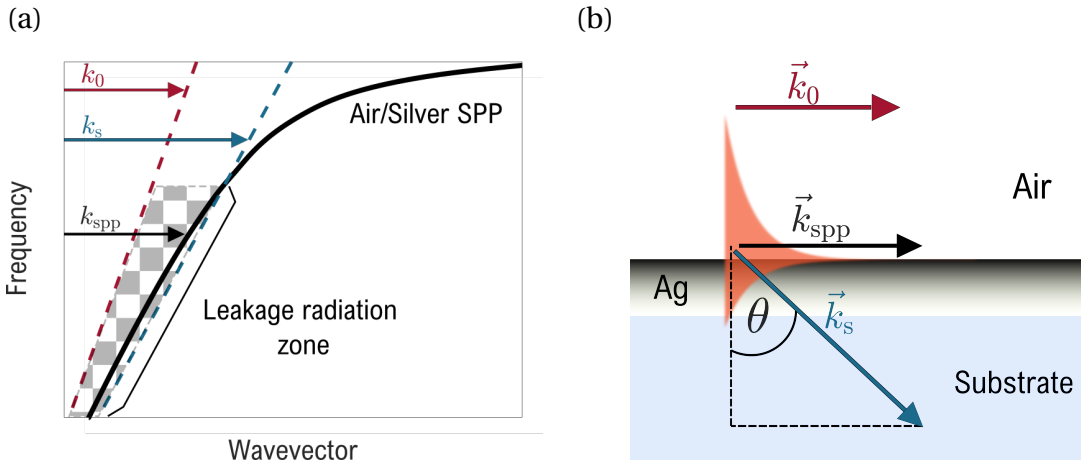


Figure 3.9 – (a) The dispersion diagram of energy as a function of the in-plane wavevector of a surface plasmon polariton from an air/silver interface. The dashed red and blue lines, correspond to the projection on the plane of the light cone in air and in the substrate, respectively. The watermark limits the region in which the SPP can decouple to the far-field. (b) Sketch of a SPP with momentum $\vec{k}_{spp}$. The momentum of light in air $\vec{k}_0$ is too small to couple to the plasmon. On the contrary, the momentum of light in the glass substrate $\vec{k}_s$ is larger and allows radiation leaking at a given angle that satisfies the phase-matching condition, provided that the metallic film is thin enough.

On the contrary, the light line in the substrate ($n_s$ = 1.515) has a momentum $\vec{k}_s$ that is higher than $\vec{k}_{spp}$ for a limited range in frequencies. Within this window in the Energy - Wavevector space, the SPPs can leak through the metal and couple to the far-field in the substrate medium. The condition for this to happen is the momentum matching between the in-plane light propagation and the plasmon:

$$k_{spp} = k_s \sin(\theta) \tag{3.1}$$

where $\theta$ is the angle between the normal and the direction of propagation of light in the substrate, as illustrated in Figure 3.9(b). This condition is also called the phase-matching condition. The above definition of $\theta$ is maintained along all this thesis. Given that $k_s = n_s \omega / c$, equation 3.1 indicates that if we are able to spectrally resolve the angular emission of the leaky modes, we can obtain their dispersion relation.

### 3.3.1 Spatial Fourier Transform of the Real-Space Image

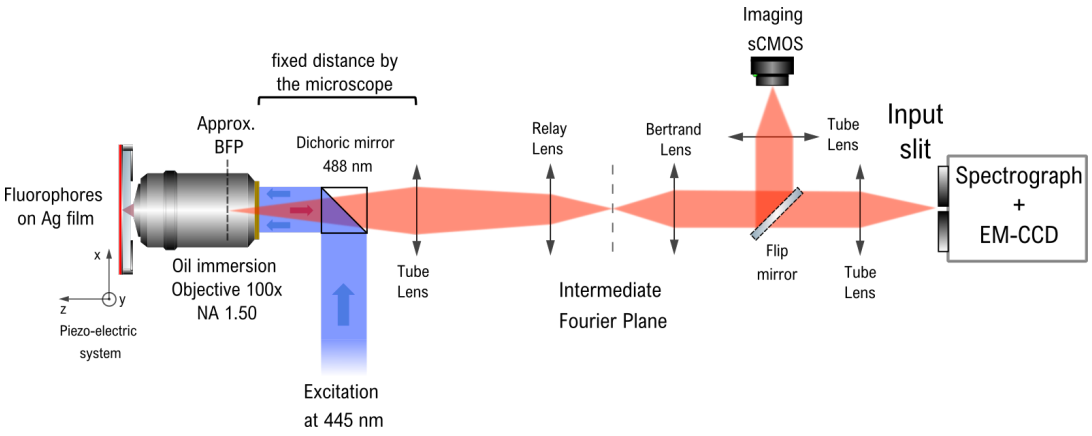


Figure 3.10 – Scheme of the setup and ray-tracing to perform spectroscopy of the reciprocal-space image of fluorescent samples. The incoming laser excitation is focused on the sample which position is controlled by piezoelectric actuators. The emission is directed either to the input slit aperture of the spectrometer, or an sCMOS camera (Zyla 5.5, Andor) used as a reference. In the microscope used during this thesis, it is impossible by construction to place the BFP on the focal plane of the tube lens. Since the tube lens is inaccessible by design, the intermediate Fourier Plane is not at a noticeable position within the detection path. A Bertrand lens is inserted to conjugate the Intermediate Fourier Plane image with the detectors. For this configuration, only oil immersion objectives are used.

In a microscopy setup, the information of the angular emission pattern of an image is contained in the back focal plane (BFP) of the microscope objective. The objective lens maps each direction $\theta$ of the light that enters it to a point $\mathbf{r}(\theta)$ onto the BFP. Figure 3.10 shows the configuration of the setup for imaging the objective's BFP at the slit of the spectrometer. The scheme presents the ray-tracing of the BFP's center, which corresponds to a converging spot for the rays that enter the objective's front lens at normal incidence.

After the relay lens, an intermediate image of the BFP is formed. A lens, called Bertrand lens, together with a second lens in front of the detector, is used to image the BFP either on an sCMOS camera or on the input slit of the spectrometer. Note that if the Bertrand lens is removed, the configuration for making a real-space image (Figure 3.4) at the spectrometer slit is retrieved.

Importantly, reciprocal-space imaging for surface plasmons is limited by the microscope objective numerical aperture. As shown in Figure 3.9(a), the leakage of SPPs

is collected above the critical angle $\theta_c = 41.3°$ for incidence at the glass-to-air boundary. Therefore, the collection must be performed through a medium with an index higher than the dielectric where the plasmon propagates and with an objective with a NA > 1. For these reasons, we only do reciprocal-imaging with high numerical aperture oil immersion microscope objectives (NA > 1.40). We match the index between the glass substrate and the microscope objective by covering the latter with a layer of immersion oil (Type A, Cargille).

Modern microscope objectives are aplanatic imaging systems, which are corrected to remove spherical and coma aberrations. For this, an objective with a focal length $f$ using an oil immersion of index $n$, has to fulfill the Abbe's sine condition:

$$\rho = nf\sin(\theta) \tag{3.2}$$

which states that a ray leaving the objective's focal plane at an angle $\theta$ with the optical axis intersects its conjugate ray on a sphere of radius $nf$, and arrives at the BFP parallel to the axis at the same height $\rho$ [4], as illustrated in Figure 3.11(a).

Figure 3.11(b) shows the intensity distribution at the BFP of the objective obtained with the sCMOS camera shown in Figure 3.10. The radiation pattern is independent on the azimuthal angle $\phi$, and we can clearly distinguish the maximal radius $\rho_{\mathrm{NA}}$, defined by the numerical aperture, and $\rho_c$ defined by the critical angle of incidence between air and the glass substrate. By taking one of these reference radii, we can calculate the angle of emission of every image point. Using the proportionality relation of (3.2) and by measuring the radius of the numerical aperture $\rho_{\mathrm{NA}}$ in Figure 3.11(b), we can establish:

$$\rho = \frac{\rho_{\mathrm{NA}}}{\sin(\theta_{\mathrm{NA}})}\sin(\theta) \tag{3.3}$$

With expression (3.3), we can determine the emission angle at any point of the BFP. Therefore, by dispersing the BFP image in the spectrometer, we can obtain the in-plane momentum corresponding to the propagating plasmon leaking from the sample (eq. 3.1). Figure 3.12(a) shows the image of a fluorescent sample made of a dense layer of emitters on top of a thin silver film. The slit is then closed down to $\Delta x = 91\,\mu$m (at FWHM on the slit plane), and the spectrometer grating disperses the light passing through the slit. The distribution in wavelength is shown in Figure

3.12(b).

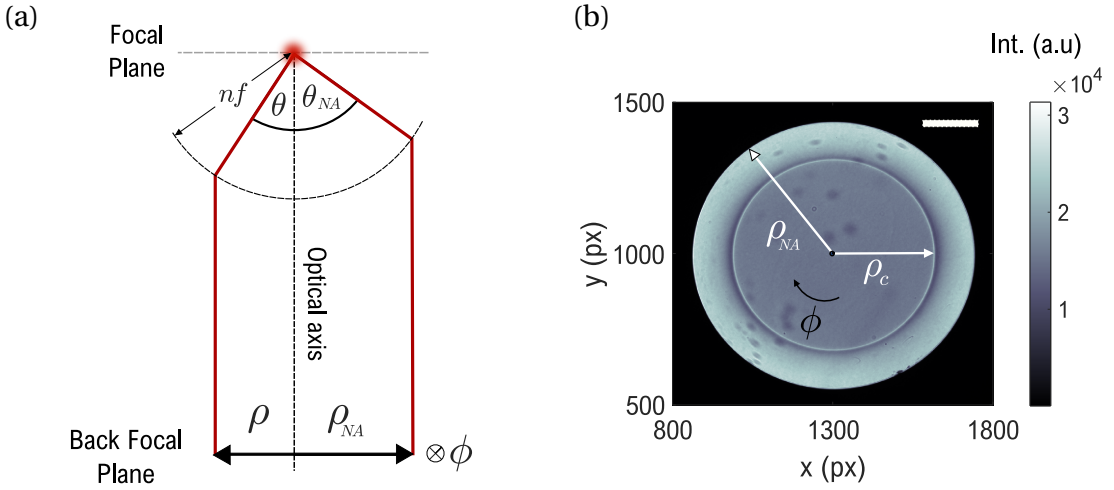


Figure 3.11 – (a) Ray-tracing for a source at the focal plane of an aplanatic microscope objective with immersion medium $n$. (b) Image of the BFP of an objective with NA = 1.4 of a layer of fluorescent emitters in glass. The maximum radius is $\rho_{\mathrm{NA}}$ and it is determined by the numerical aperture of the objective $\theta_{\mathrm{NA}} = 67.1°$. $\rho_c$ shows that there is an abrupt change in the emission at the critical angle between air and the glass substrate $\theta_c = 41.3°$. The scale bar in the upper right corner represents 1 mm in the objective's BFP.

The spectrometer slit makes a narrow diametrical slice of the entire image of the BFP when it is closed. In this way, each horizontal spectral dispersion is done in a reduced range of angles. The opening width of the slit represents a compromise between the amount of signal and the resolution in $\theta$. By closing the slit down to a width of 91 $\mu$m, we have that $\Delta\theta < 1°$ for angles greater than 20°.

Relating the angle and the wavelength axis, we can obtain the corresponding in-plane wavevector (through equation 3.1) of all the points of images like the one presented Figure 3.12(b). Figure 3.13 shows the $E$ vs. $k$ diagrams for measurements performed in a system composed of a layer of quantum dots on top of a silver film. Figure 3.13(a) shows a reflectometry measurement in which the broad absorption band of the plasmon is observed. Figure 3.13(b) shows the luminescence of the system emitting through the SPP line and centered at the energy of the quantum dots ($\sim 2040$ meV).

Importantly, we image an intermediate plane of the detection path for both real

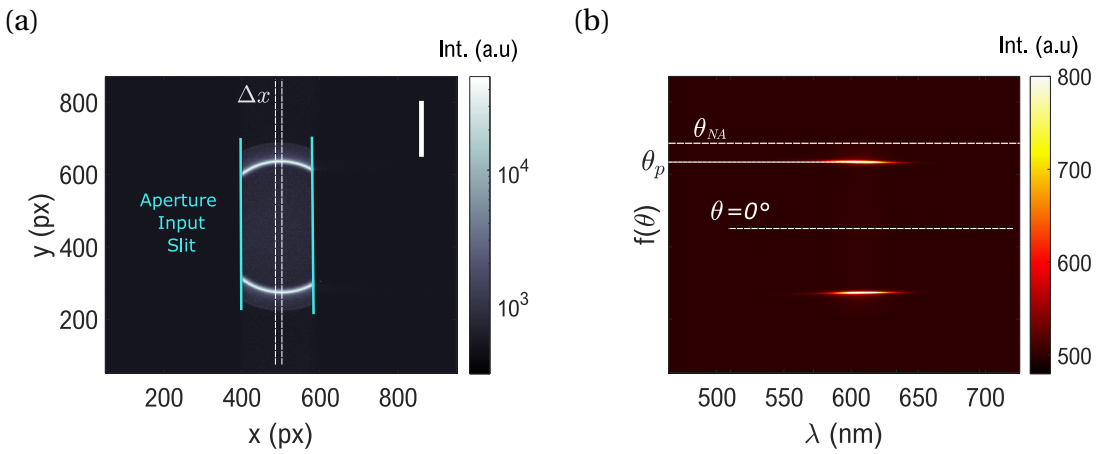


Figure 3.12 – Reciprocal-space image of the fluorescence of a sample consisting of quantum dots weakly coupled to a silver film, obtained with an objective with NA=1.50. (a) The spectrometer slit is open, and the strong intensity of the emission at the plasmon angle $\theta_p = 43.5°$ is clearly observed. The dotted white lines show the width of the slit when it is closed to $\Delta x = 91\,\mu$m (at FWHM on the slit plane) for the spectral measurement shown in (b). The bar in the upper right corner represents a length of 2 mm in the objective's BFP. The measured radius of the NA rays is $\rho_{\mathrm{NA}} = 3.012$ mm. The spectral dispersion of the emission of the quantum dots centered at 607 nm is highly directed in the leaking angle of the plasmon $\theta_p$.

and Fourier spaces, allowing us to filter the sample's emission. Figure 3.4 shows the position of the intermediate real image in which we can place a pinhole to filter spatially. In Figure 3.10 we observe the intermediate Fourier image plane, which adds a degree of freedom to our setup, considering that evanescent modes only couple to the far-field in supercritical angles. In this way, we can discriminate the emission coming from direct fluorescence from the one decoupling from evanescent modes. Also, we can use Fourier filtering to take dispersion measurements. For example, in a previous setup not shown in this chapter, we used 3D-printed circular masks to cover concentrically the BFP image. By closing an iris at the same plane, we selected a limited range of angles to be refocused at the input of a fibered spectrometer.

### 3.3.2 Reflectometry measurements

Figure 3.13 shows how reflectometry measurements complement the information of the luminescence dispersion of the same sample, in which the broad absorption band of the plasmon is observed. To perform reflectometry, we included an incan-

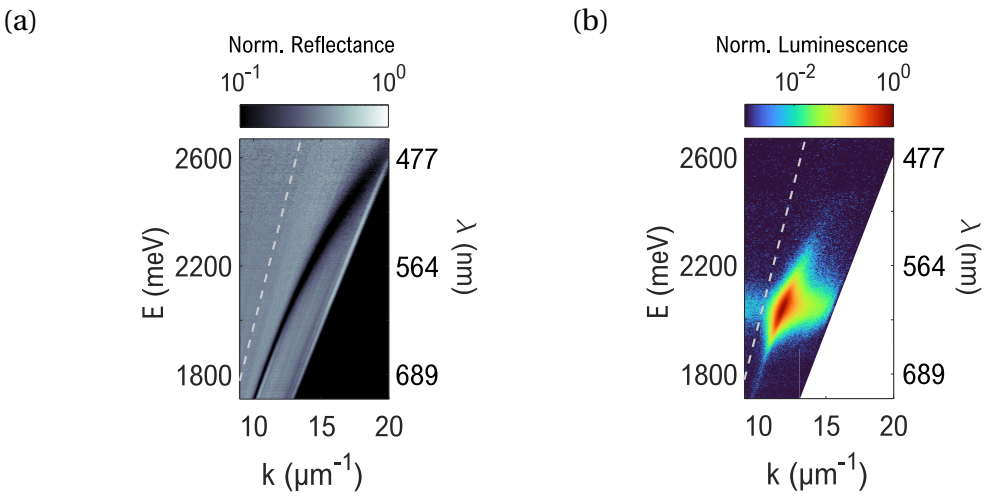


Figure 3.13 – $E$ vs. $k$ diagrams for (a) reflectometry and (b) luminescence measurements of a sample made of quantum dots lying on a thin film of silver. In (a) the broadband character of the plasmon is seen. In (b) the narrow band emission of the quantum dots can be observed along the plasmonic mode. The light line $E = \hbar c k$ (gray dashed line) indicates the critical angle $\theta_c$ between air and glass.

descent white lamp in the excitation path of our fluorescence microscopy setup. Figure 3.14 shows the optical scheme of this setup. A large diverging beam of white light is filtered by a pinhole of 150 $\mu$m before collimation. The optics in the excitation path and the objective produce a 6 $\mu$m image of the pinhole at the sample plane. The incoming light illuminates the sample and it is absorbed in function of the optical modes present in the system. In the scheme, a sample containing a silver thin film is sketched with the absorption dip at the plasmon angle. Concerning the imaging detection path, the setup is identical to the one for luminescence.

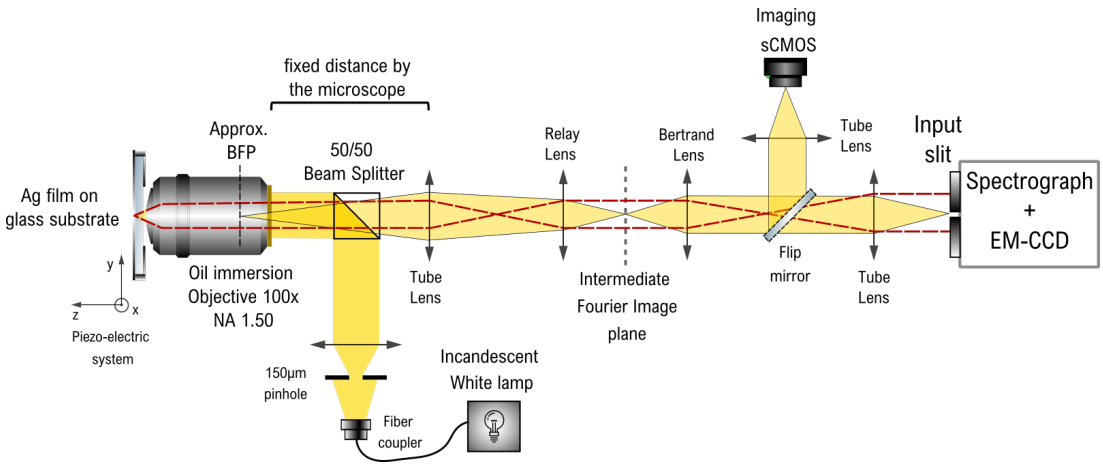


Figure 3.14 – Scheme of the setup for reflectometry measurements. The ray-tracing is similar as for spectroscopy of the reciprocal-space image in fluorescence. Contrarily to laser excitations, the incandescent white lamp is filtered by a pinhole, and then the latter is imaged at the sample plane. The reflected beam is represented with a gray contour. In the scheme, an Ag film is observed, and the red dashed lines represent (not on scale) the angles at which the SPP absorbs the white light. This is observed as a dip at an angle of 43.7° in the detectors.

## 3.4 Conclusion

In this chapter, we presented the microscopy setup that we use to characterize the samples described in this thesis. First, we outlined the excitation and detection paths, and remarked the difference between air-side and substrate-side excitation. Then, we showed characterization of the real-space fluorescence image. The combination of the spectrograph and a camera with a square chip allows us to acquire a determined region of a sample and disperse it in wavelength. Using an alternative path, we direct the real-space image to a SPAD connected to a TCSPC module to measure the decay rate of fluorescent emitters. Afterward, we described the spectroscopy technique used to study the reciprocal-space image of the samples' fluorescence and reflectance. By making an image of the microscope objective's back focal plane on the spectrometer slit, we spectrally disperse the radiation pattern to retrieve the energy of the modes propagating within the sample as a function of their in-plane wavevector.

# References

[1] X. Zhong, T. Chervy, L. Zhang, A. Thomas, J. George, C. Genet, J. A. Hutchison, and T. W. Ebbesen, *Angewandte Chemie International Edition* **56**, 9034–9038 (2017). 54

[2] L. Novotny and B. Hecht, *Principles of Nano-Optics*, Cambridge University Press (2006). 54

[3] D. Bouchet, *Transfert d'énergie engendré par plasmon et imagerie de super-résolution en champ proche de milieux nano-structurés*, Ph.D. thesis, PSL Research University (2017). 55

[4] R. Juškaitis, *Characterizing High Numerical Aperture Microscope Objective Lenses*, pages 21–43, Springer Berlin Heidelberg, Berlin, Heidelberg (2003). 58

# Chapter 4

# Quantum dots weakly coupled to a strongly coupled system

## Contents

This chapter presents the leading work of this thesis. We probed the electromagnetic environment created in the vicinity of a strongly coupled system composed of organic J-aggregates and an SPP. For this study, we used a continuous silver thin film in which nanocrystalline quantum dots (QDs) interact with the strongly coupled doublet via propagating modes, including SPPs and hybrid exciton/SPP polaritons. The QDs, which have a small oscillator strength compared to the organic dye, couple weakly to the near-field modes of the sample, allowing their use as a probe emitter. In order to exploit this property, we used three species of QDs whose emission overlap different energy regions of the strongly coupled polaritons. The work presented here takes place in the frame of a collaboration between the team Matériaux et Nanostructures Photoniques, led by Joel Bellessa at ILM Lyon, and our team at Institut Langevin. The optical lithography and the fabrication of some samples were performed at ILM Lyon, while the optical characterization of the samples were done at Institut Langevin during my PhD. We acknowledge Alban Gassenq for the design and realization of the optical lithography detailed in section 4.1, and Jean-Michel Benoit, Clémentine Symonds, and Joel Bellessa for the sample fabrication process and the numerous very stimulating scientific discussions we had on all the subtilities of strong coupling.

This chapter is divided into four parts. The first part describes the composition and fabrication of the samples. We start by summarizing the physical properties of J-aggregates and semiconductor QDs. Then, we detail the fabrication process of three multilayered samples consisting of a thin film of silver evaporated on a silica substrate and spin-coated layers of the fluorescent emitters. For all samples, we performed an optical lithography in the layer of J-aggregates by producing circular photobleached areas (CPAs) with various diameters. After this process, we added QDs embedded in a PMMA layer with an emission wavelength which is different for each of the three samples. We end this part by showing the reflectance behavior of the samples and reporting their respective Rabi splitting.

In the second part, we study the coupling of the QDs to the propagating modes of the different samples. We present the Fourier spectroscopy of the luminescence of the multilayered structure. The resulting emission patterns show the contribution of both fluorescent layers: the J-aggregates strongly couple to the SPP and create polaritonic modes while the QDs weakly couple to such modes. We initially compare

two extreme cases. Firstly, the QDs emission in large regions with photobleached J-aggregates, and, secondly, when the QDs are directly on top of active J-aggregates. Afterward, we present the emission pattern of QDs excited in CPAs of different sizes, where the progressive modification of the coupling is observed.

In the third part, we present a model based on local Kirchhoff's law for photoluminescence and the corresponding simulations for the emission of one of the samples. The work shown in this section is performed in the frame of a collaboration with the team Plasmonics and Quantum Nanophotonics led by Jean-Jacques
Greffet at Laboratory Charles Fabry. The model reproduces the system's behavior, assuming that the emitters' excitations are thermalized, and a chemical potential is introduced to account for each material's electronic resonance. By leaving the chemical potential difference between the QDs and the J-aggregates as a free parameter, the model is fitted to the experimental data. We acknowledge Elise Bailly who developed and optimized the code that lead to the simulations shown in this section, being supervised by Jean-Jacques Greffet and Benjamin Vest. A publication summarizing all these results is under preparation [1].

In the fourth part of this chapter, we show decay rate measurements that attempted to complement the continuous modification observed in the emission patterns. Despite observing an enhancement of the decay rate of the QDs when they are on active J-aggregates, the contribution of a long-lifetime component complicated quantitative results.

## 4.1 Sample Description

### 4.1.1 Fluorescent Emitters

We use a layer of J-aggregated TDBC as the active material to strongly couple to SPPs, and nanocrystal multishell quantum dots as a probe for the strongly coupled modes and their extension. The photophysical properties of both emitters are summarized below.

#### *J-aggregates*

We are interested in 5,6-Dichloro-2-[[5,6-dichoro-1-ethyl-3-(4-sulfobutyl)-benzimidazol-2 -ylidene]-propenyl]-1-ethyl-3-(4-sulfobutyl)-benzimidazolium hydroxide, inner salt, sodium salt (TDBC), which is an organic cyanine dye that has extraordinary optical properties. Figure 4.1a shows the chemical structure of TDBC and the dashed cyan curve of Figure 4.1b its monomer's absorption spectrum. The dashed yellow curve of Figure 4.1b shows a narrow red-shifted absorption peak of highly concentrated TDBC in an aqueous solution and the solid red curve its photoluminescence (PL) spectrum when deposited on a glass substrate featuring a small Stoke's shift. The narrow absorption band appears for concentrations $\sim 1\,\mu$M and overcomes the monomer's absorption for concentrations higher than $\sim 100\,\mu$M [2]. This phenomenon occurs because of the self-assembly ordering of the TDBC. This process is called J-aggregation, and its physical origin and effects are explained in the following.

Scheibe and Jelley (so the name *J*-aggregate) independently discovered in the 1930s the formation of a new absorption band (J-band) of the Pseudoisocyanine chloride (PIC) dye when raising its concentration in solution. This spectral property was soon attributed to the ordered arrangement of the dye monomers. Figure 4.2a shows two stacked cyanine monomers which self-assembly in high concentrations due to Van der Waals forces [3], where their dipole moments make an angle $\alpha$ with the vector $\mathbf{r}$ connecting the dipole centers. In J-aggregates, this angle is $\alpha < 32°$ [4] and for the specific case of TDBC has been calculated to be $\alpha = 23.15°$ [5]. This implies that the monomers stack in a linear chain following a head-tail configuration [6], and it has been found, based on linear dichroism experiments, that the total polarization of the molecular chains has a total dipole moment parallel to the aggregate

axis [7].

(a) (b)

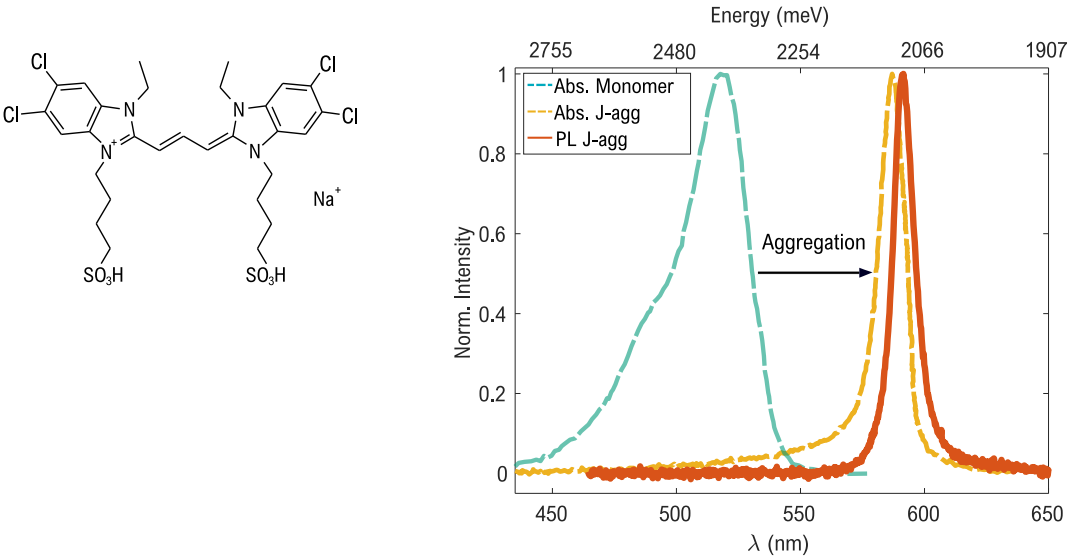


Figure 4.1 – (a) Chemical structure of the TDBC monomer. (b) Absorbance of the TDBC monomer (dashed cyan curve) obtained from the site of its manufacturer Few chemicals, and J-aggregate (dashed yellow curve) in aqueous solutions [2]. The absorption maximum shifts from 517 to 587 nm (2110 meV) through J-aggregation, and the FWHM narrows from 33 to 13 nm. The solid red curve shows the PL spectrum of a layer of J-aggregated TDBC deposited on glass, with a peak at 594 nm (2085 meV).

This molecular configuration determines the narrowing and a red-shift of J-aggregates relative to their corresponding monomers. Notably, the head-tail arrangement leads molecules to hybridize and form $\pi$-electron states coherently delocalized over part of the molecular aggregate [8]. In the case of a J-dimer, there is a splitting of the excited state energy level into two levels because of electronic hybridization, and energy band-like levels appear for an aggregate, as depicted in Figure 4.2b. Importantly, selection rules favor the radiative transition between the LUMO and the HOMO in J-aggregates. Let us consider the case of the dimer: if the vector sum of the transition dipole moments of aggregated monomers is zero (i.e., when the dipoles have opposing orientations), the electronic transition to the upper level is forbidden and cannot be spectrally observed. Instead, the transition to the upper level of the split excited

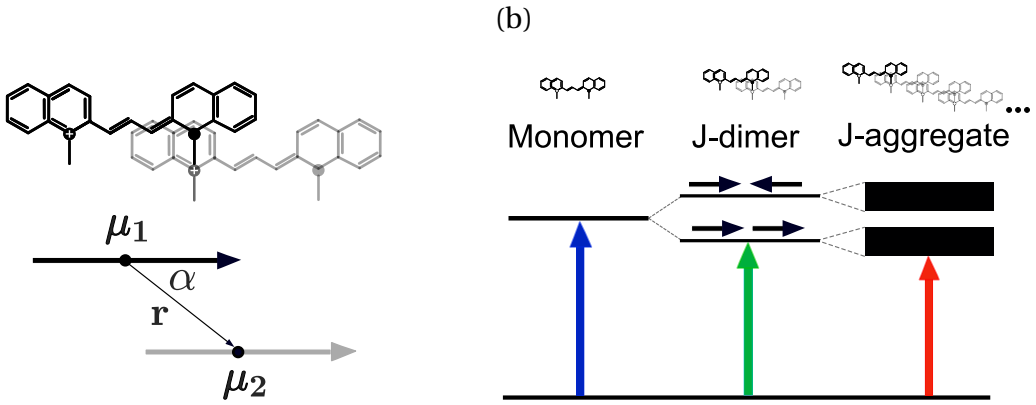


Figure 4.2 – (a) Sketch of the aggregation of two cyanine molecules into a dimer. The molecules are stacked together, and the direction parallel to their dipole moments makes an angle $\alpha$ with the vector **r** connecting the dipole centers of the neighboring molecules. In J-aggregates, they stack in a head-tail-like configuration in which $\alpha \sim 23°$ [5]. (b) Sketch of the electronic levels of a monomer, a J-dimer, and a J-aggregate. As the number of monomers increases, the difference between the LUMO and the HOMO becomes smaller. For simplicity, the ground state energy levels are shown to be the same for a monomer and aggregates.

levels is allowed, and the maximum absorption of the dimer will be red-shifted relative to the absorption of the monomer [3]. Similarly, in the J-aggregate, the oscillator strength will be concentrated on the HOMO-LUMO transition producing the spectral narrow peak characteristic of J-bands.

In this thesis, we used J-aggregates as the active material for strong coupling with an SPP mode. The high oscillator strength of J-aggregates has made them materials of choice for strong coupling observation at room temperatures. In this chapter, we used TDBC, and for the work presented in Chapter V, we used another dye named S2278 by its manufacturer. Both are anionic cyanine molecules in which conjugated double bonds containing amino groups are responsible for their fluorescence [9]. Importantly for the fabrication of samples, their basic structure allows achieving a high aggregate structural stability [3] and their anionic character plays a role in the adhesion to substrates in the sample fabrication process, as it will be shown later.

***Nanocrystalline Quantum Dots***

As optical probe emitters, we use semiconductor nanocrystals called quantum dots (QDs). In semiconductor materials with a direct bandgap, an impinging photon can be absorbed, and in this way, it promotes an electron of the valence band to the conduction band. This electron is bound to the vacancy hole left behind in the valence band (the *hole*) by a Coulombic interaction, and the electron-hole pair is called an exciton. The exciton recombination (the relaxation of the electron to the valence band) emits a photon with an energy that matches the bandgap. Since an exciton is delocalized within the crystalline structure in semiconductors, the optical properties of QDs are determined by the relation between the delocalization length and the nanocrystal size.

The exciton Bohr radius is defined as the average separation between the electron and the hole. For QDs, the nanocrystal size is of the same order as the exciton Bohr radius. At this scale, spatial confinement plays a role and can be exploited to modify the exciton energy states. As the size is reduced, the bandgap is increased, and the electronic excitation shifts to higher energies, as sketched in Figure 4.3a. We are interested in II-IV semiconductors, whose Bohr radii can be of the order of 10 nm within the bulk [10]. Specifically, we use QDs where the exciton recombination happens in CdSe, which has a bandgap of 1.74 eV [11] and a Bohr radius of 5.4 nm for its bulk crystalline structure [12].

The size reduction of the QDs entails a sensibility to a variety of surface effects. Small surface-to-volume ratios make the interaction between the surface atoms and environment relevant, significantly contributing to additional non-radiative decay paths for excitonic relaxation. These processes are detrimental to achieving a high luminescence quantum yield since any surface defect will increase the non-radiative decay pathways [10; 13]. For this reason, secondary semiconductor materials with a larger bandgap are used in QDs synthesis to cap the nanocrystal confining the exciton in the *core* material. This protective *shell* protects the core from interaction with the surface and also makes it possible to functionalize the QDs surface without disturbing its radiative properties. In this way, organic molecules, known as passivating ligands, are added to control the nucleation, growth kinetics, and stabilization of colloidal QDs [13; 14]. A sketch of the overall core/shell QD architecture is shown in

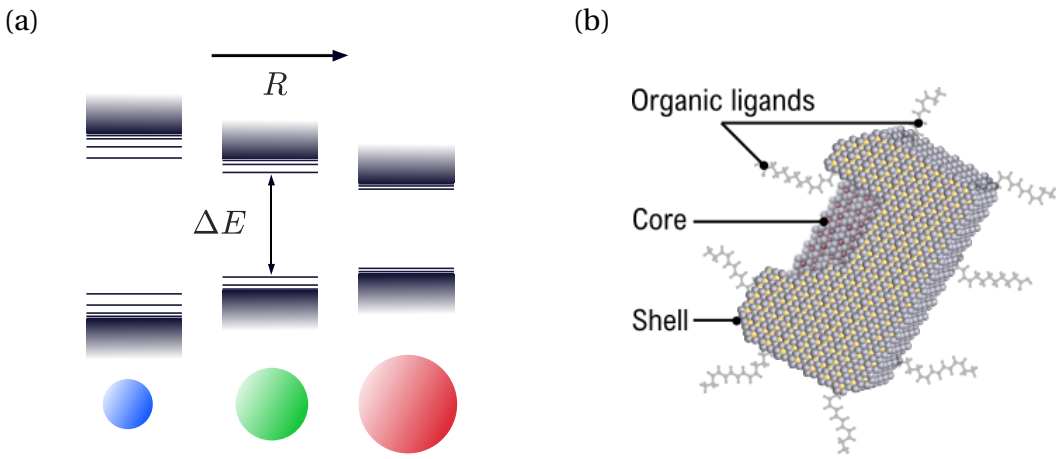


Figure 4.3 – Engineering the crystalline structure and size of QDs allows to span the emission wavelength of them along the complete visible spectrum and beyond. (a) Tuning the size of the quantum dot changes the semiconductor energy bands. As the nanocrystal gets smaller, the energy gap between the valence and the conduction bands becomes larger. (b) Sketch of a core-shell quantum dot showing the two different crystalline structures for the core and the shell. The organic ligands passivate the QD surface. Image reproduced from a representation in [10].

Figure 4.3b.

In practice, the exciton wavefunction can leak through the shell, implying that thicker layers (or larger bandgaps) are needed to prevent the exciton from probing the surface effectively. However, interfacial strain induced by lattice mismatch between the core and shell crystalline structures may limit the number of shell monolayers [13]. The solution is to grow multiple shells of different compositions around a central core so that the energy offsets progressively towards the surface but with small lattice mismatches between subsequent shells. In this thesis, we use CdSe core CdS/CdZnS/ZnS multishell QDs with a gradient alloy in the shell (CdZnS), smoothly varying the lattice parameters and energy offsets of the shell layers towards the outer ZnS structure.

We used three species of QDs with emission peaks at 544 nm, 575 nm and 607 nm, which were synthesized by Thomas Pons and Sandrine Ithurria at the Laboratoire de Physique et d'Étude des Matériaux (LPEM), ESPCI. Besides the QDs emitting at 544 nm, which is composed of a gradient alloy (Cd,Zn)(S,Se)), they are composed of a CdSe core and contain shell layers of CdS, the alloy CdSZnS, and ZnS. Table 4.1

| $\lambda_{PL}$ (nm) | CdSe ⌀ (nm) | # CdS Ml | # CdSZnS Ml | # ZnS Ml | $\varnothing_{tot}$ (nm) |
|---|---|---|---|---|---|
| 544 | - | - | - | - | 5.4 |
| 575 | 2 | 3 | 2 | 2 | ~ 8 |
| 607 | 4.1 | 3 | 2 | 2 | ~ 9 |

Table 4.1 – Summary of the composition and size of the QDs used in this thesis. They are ordered as a function of their central emission wavelength $\lambda_{PL}$. The table shows the diameter of the CdSe core, the number of monolayers (Ml) for the different shell materials, and the total diameter of the QD. The QDs emitting at 544 nm are composed of a gradient alloy (Cd,Zn)(S,Se)) and therefore columns 2-5 are empty. The organic passivating ligands used for the three species were oleic acid and oleylamine.

summarizes the composition and size of these QDs. The organic ligands used for the three species were oleic acid and oleylamine. Figure 4.4 shows the absorbance and PL spectra of the studied QDs. As it is observed in Figure 4.4a, the QDs have broad absorption spectra in which the first exciton peak can be distinguished. Advantageously, the increasing absorption of the QDs towards short wavelengths allows us to efficiently excite them by a single light source, for which we used a 445 nm laser. Figure 4.4b shows their PL spectra. The spectral distance between the PL peaks (FWHMs< 40 nm) is approximately 30 nm. These PL spectra show the energy range in which we can probe how the QDs couple to a given system, as the strongly coupled J-aggregates/SPP. Furthermore, they possess long decay lifetimes (~ 10 ns), which should in principle make it possible to observe modifications in their decay rate when interacting with an environment using TCSPC measurements.

### 4.1.2 Sample fabrication

During my PhD, we studied multilayered systems that consist of two fluorescent materials deposited on top of a glass substrate capped with silver. We deposited J-aggregated TDBC on top of a 50 nm film of silver and performed optical lithography containing circular photobleached areas. As the last step, we deposited on top a layer of QDs embedded in a polymer matrix. We fabricated three different samples, one for each of the QDs species described above. Figure 4.5 shows a sketch of the sample containing the elements described in this section. The thickness of each layer was measured by atomic force microscopy (AFM) topography analysis.

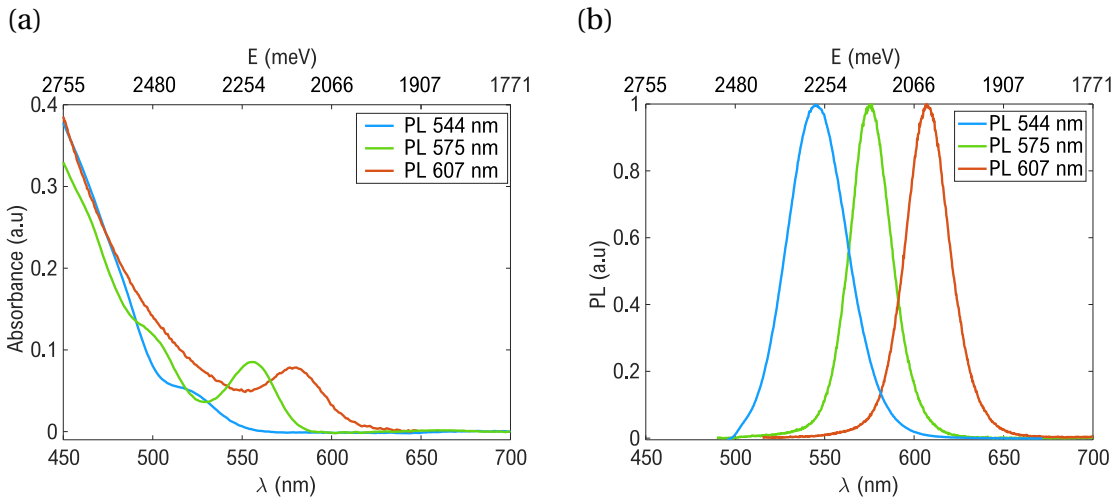


Figure 4.4 – Spectra of the three different QDs used in this thesis. (a) Absorbance of the QDs in solution. The spectra are characterized by a large absorption band at high energies and an exciton resonance at 522 nm (blue), 526 nm (green), and 580 nm (red). The curves are labeled by the central wavelength of their emission maxima. (b) Photoluminescence of the QDs deposited on a glass substrate. The center emission wavelengths of the spectra are 544 nm = 2279 meV (blue), 575 nm = 2156 meV (green), and 607 nm = 2042 meV (red). The corresponding FWHM are 38.9 nm (162.4 meV), 27.0 nm (100.2 meV), 28.3 nm (95.2 meV), respectively.

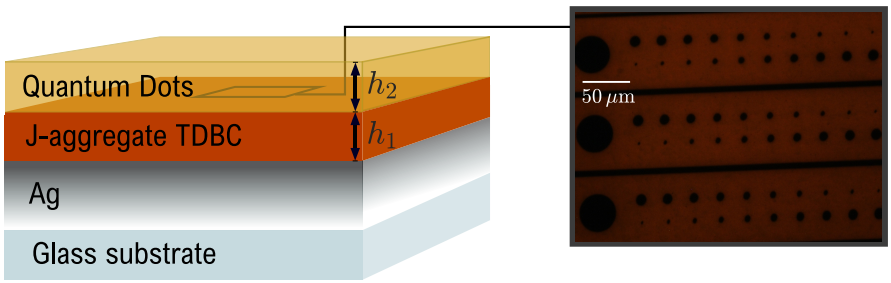


Figure 4.5 – Sketch of a multilayered sample consisting of two fluorescent thin films deposited on top of a 50 nm layer of silver evaporated on a glass substrate. The first deposited layer of thickness $h_1$ contains the J-aggregate TDBC. The dark-field microscopy image shows the optical lithography performed on this layer in which the exposition to a UV laser has photobleached the circular dark areas. After that, a second layer of thickness $h_2$ containing quantum dots is deposited.

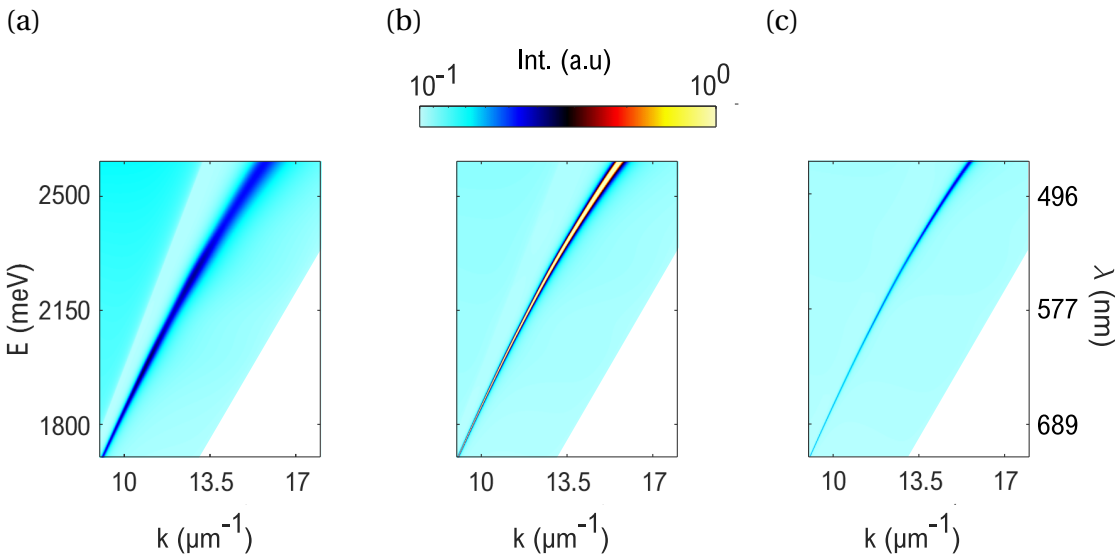


Figure 4.6 – TMM computation of the reflectance dispersion of a surface plasmon polariton propagating at the interface between the air and a silver layer of thickness a) 30 nm, b) 50 nm, and c) 70 nm.

### Substrate

We used standard glass coverslips (Menzel Gläser Microscope Coverslips, Thermo Scientific) for all our samples. It is made of pure white D 263 M borosilicate glass with a refractive index similar to the immersion oil used for the high-numerical aperture microscope objective ($n$ =1.5227 at 600 nm). The coverslips have a size of 24 × 24 mm and a thickness of ∼ 0.17 mm.

### Deposition of silver thin films

The thickness of the silver film on top of the glass substrate determines the coupling of light to propagating SPP mode. As shown by the calculated reflectance reported in Figure 4.6, increasing thickness narrows the plasmon linewidth, but at the same time, the absorption of the metal restricts the amount of light that couples to the SPP, which complicates experimental observations. We worked with a thickness of 50 nm, based on the optimization carried by K. Chevrier at ILM Lyon during his PhD [15]. The plasmon dispersion relations are calculated with the Transfer-Matrix Method (TMM), developed in Chapter 2.

For the silver film deposition, two different evaporation setups were used. The first was employed at ILM Lyon and the second in the cleanroom of Université Paris Diderot. In both cases, the deposition consists of striking a melting pot containing silver under high vacuum conditions ($< 10^{-7}$ mbar) with an electron beam. The collisions heat the silver to its melting point, and the evaporated particles follow a ballistic trajectory through the vacuum chamber to the depositing plate. The deposition is monitored by a quartz crystal microbalance placed in the vacuum chamber, close to the sample holder. During the deposition process, the same amount of metal adhere on the coverslip and on the quartz balance, by modifying the vibration frequency of the quartz. An accurate measurement of the variation of the frequency allows to determine the amount of deposited metal and therefore the average thickness. The addition of mass onto the film modifies the acoustic impedance of the whole system changing its vibration frequency [15; 16], allowing the determination of the thickness of the layer. Once the silver was deposited, we tested the sample reflectance with the setup described in Chapter 3, and the result is shown in Figure 4.7a). Figure 4.7b) shows a section of the reflectance at a wavelength of $\lambda = 600\,\text{nm}$ ($E = 2066.4\,\text{meV}$). By estimating the width of the dip, we calculate the propagation of the SPP $L_{\text{spp}} = 7.6\,\mu\text{m}$ around the emission of the strongly coupled system, as it will be shown later.

**Deposition of the TDBC J-aggregate layer**

The first optical active layer on top of silver consists of a thin film of J-aggregated TDBC. It has been observed that aqueous solutions with high concentrations of this dye ($> 1 \times 10^{-3}\,\text{M}$) do not attach to bare silver or glass surfaces due to hydrophobic effects [15]. Therefore, we capped the silver surface with an adhesion layer of poly(diallyldimethylamonium chloride) (PDAC) to assure a stable and homogeneous deposit of the J-aggregates. PDAC is a polymer optically neutral in the spectral regions of our interest, and its deposition has the only goal to improve the adhesion of the J-aggregates. We prepared an aqueous solution of PDAC (409014, Sigma Aldrich) at a mass concentration of 2%. Afterward, we filtered the solution through 0.8 $\mu$m syringe filters (P820.1, Carl Roth) to avoid the presence of inhomogeneous polymer chains. We placed the coverslip with the silver film in a chemical bath of the filtered solution. The process consists of a 2 minutes bath in the PDAC solution followed by

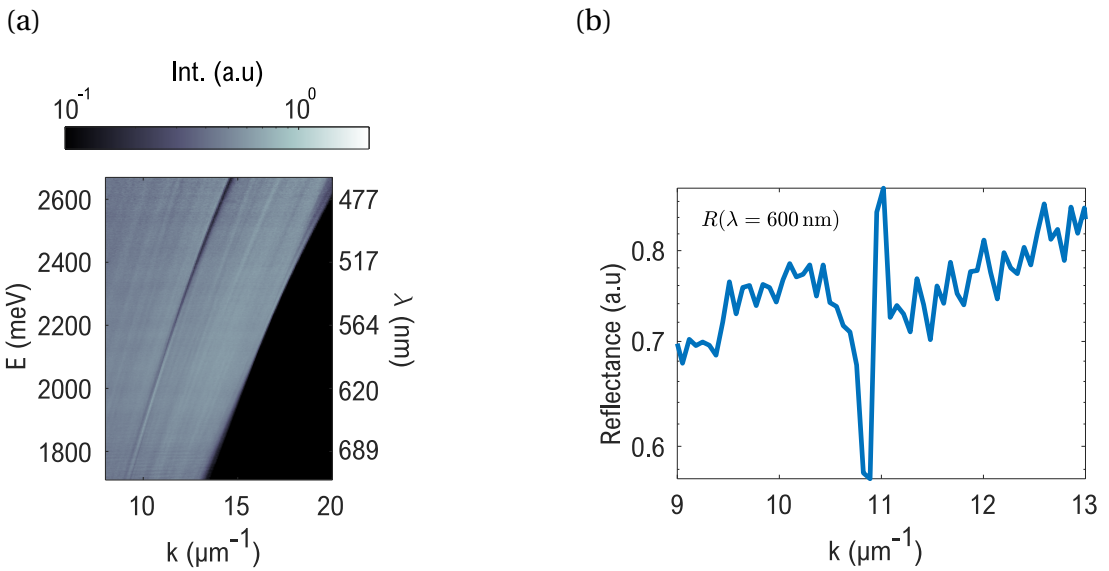


Figure 4.7 – (a) Reflectance dispersion measurement of a sample consisting of a glass substrate an a 50 nm thin silver film. The light couples to the SPP mode producing the sharp dip dispersion line. (b) Reflectance for a section of (a) at $\lambda = 600\,\text{nm}$ ($E = 2066.4\,\text{meV}$). The FWHM of the dip is $\Delta k \sim 0.26\,\mu\text{m}^{-1}$ corresponding to a propagation length of $7.6\,\mu$m at this wavelength.

two successive baths of 1 minute each on distilled water to rinse the excess of polymer, leaving a monolayer of PDAC on top of the silver. Finally, the samples were dried by blowing compressed air to remove the remaining water drops.

We prepared a solution of TDBC (S 0046, Few Chemicals) in distilled water with a concentration of 8.6 mM, in which the dye is in a J-aggregated phase (as described in the previous section). We spin-coated 300 $\mu$L of the solution on top of the silver film coated with PDAC, with the following program of two steps:
1) time = 7 seconds, speed = 600 rpm, acceleration = 600 rpm/sec
2) time = 53 seconds, speed = 7900 rpm, acceleration = 1000 rpm/sec
The resulting thickness of J-aggregates layers, measured by AFM, has an average value of $\bar{h}_1 = 18.2\,\text{nm}$. Figure 4.8 shows the reflectance of a sample with deposited J-aggregates on silver, in which the formation of polariton states with a corresponding Rabi splitting of 157 meV was observed. We concluded that the SPP and the J-aggregates enter in the strong coupling regime of interaction through these measurements. Moreover, they allowed us to monitor the effect of the later deposition of the second dielectric

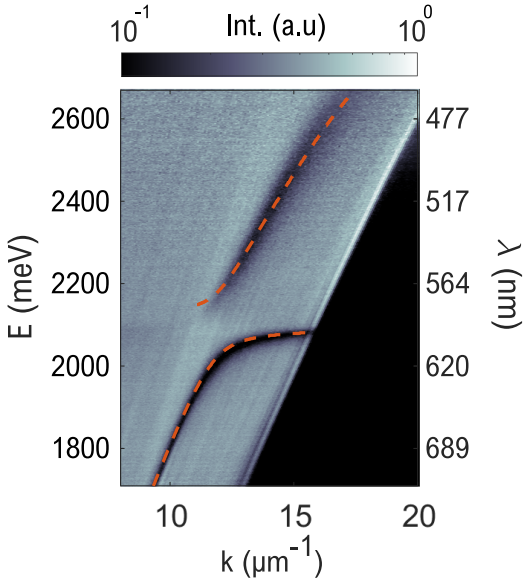


Figure 4.8 – Reflectometry measurement of a sample composed of a thin film of silver (50 nm) evaporated on glass with a layer of J-aggregates spin-coated on top. The formation of a polariton states separated by a Rabi splitting of 157 meV is observed. The red-dashed line shows the calculated reflectance minima for a dielectric layer of $h_1 = 23$ nm with a background refractive index of $n_b = 1.72$ and an oscillator strength of $A = 4.5 \times 10^5$.

layer containing the QDs.

**Patterning through UV-lithography**

In this chapter, we studied non-local phenomena mediated by propagating surface modes. For this purpose, we lithographed a geometrical motif on the J-aggregates layer to create zones in which the optical transition of the dye becomes inactive. In this way, we could probe the finite extension of the polaritonic modes, which are the product of strong coupling between the active J-aggregates and the SPP. We designed the motif with the circular photobleached areas (CPAs) shown in Figure 4.9b, so that an emitter placed at the center of them will be subject to a 2D isotropic medium. Considering the coherence length of the strongly coupled polaritons $\sim 7\,\mu$m reported on [17; 18], we created CPAs in which the radius spans around this value. The different CPAs have diameters from 1 to 10 $\mu$m (spaced by 1 $\mu$m) and two larger diameters of 20 and 40 $\mu$m. The lithography was performed in Lyon by Alban Gassenq with a Micro Pattern Generator ($\mu$PG101, Heidelberg Instruments) at an exposition wave-

length of $\lambda = 375\,\text{nm}$ with a head laser that lithographs with a resolution of $0.9\,\mu\text{m}$, following the method developed for the samples used in [18].

The photobleaching process consists of exposing the sample to a UV-high optical power laser to bring the J-aggregates in an inactive optical state. Intense exposure increases the total number of excitation cycles in which the molecules undergo a transition to the triplet state. The triplet state has a long decay lifetime relative to the singlet state, thus allowing excited molecules a much longer time frame to interact with the local environment. Generally, the most significant interaction is with singlet oxygen, created through triplet-triplet annihilation between the excited triplet-state fluorophores and the ground triplet state atmospheric triplet oxygen. Through the high-power laser irradiation, singlet oxygen reacts with the conjugated systems of the organic dyes, irreversibly degrading the fluorescent transition [19].

Figure 4.9a shows the spectral analysis of the lithographed areas in which we verified the suppression of the absorption peak of the J-aggregates around 590 nm. Figure 4.9c shows a reflectometry measurement performed on a $40\,\mu\text{m}$ CPA, in which the illuminated region is far from the strongly coupled surroundings. We fitted the reflectance with a TMM calculation of a dielectric layer of constant refractive index $n_b = 1.72$ and a thickness of 19 nm. Notably, AFM measurements revealed that the photobleaching of the samples reduces its thickness which explains the discrepancy between the thickness values of Figures 4.9c and 4.8. The CPA of diameter $\varnothing = 40\,\mu\text{m}$ is taken as a reference to observe the emission through plasmon far away from the strongly coupled system.

#### Deposition of the QDs layer

On top of the J-aggregates layer, we added a second active layer containing QDs embedded in a transparent Poly(methyl methacrylate) PMMA matrix. We prepared three different samples for each of the QDs whose spectra were shown in Figure 4.4. Figure 4.10a shows how the QDs emission of the three samples relate spectrally to the strongly coupled modes of the system. The QDs emitting at 607 nm are resonant with the lower polariton and their emission spectrum partially overlaps the gap between the polaritons. The sample with these QDs is labeled then RLP. Similarly, the sample with QDs emitting at 575 nm which are resonant with the low energy region of

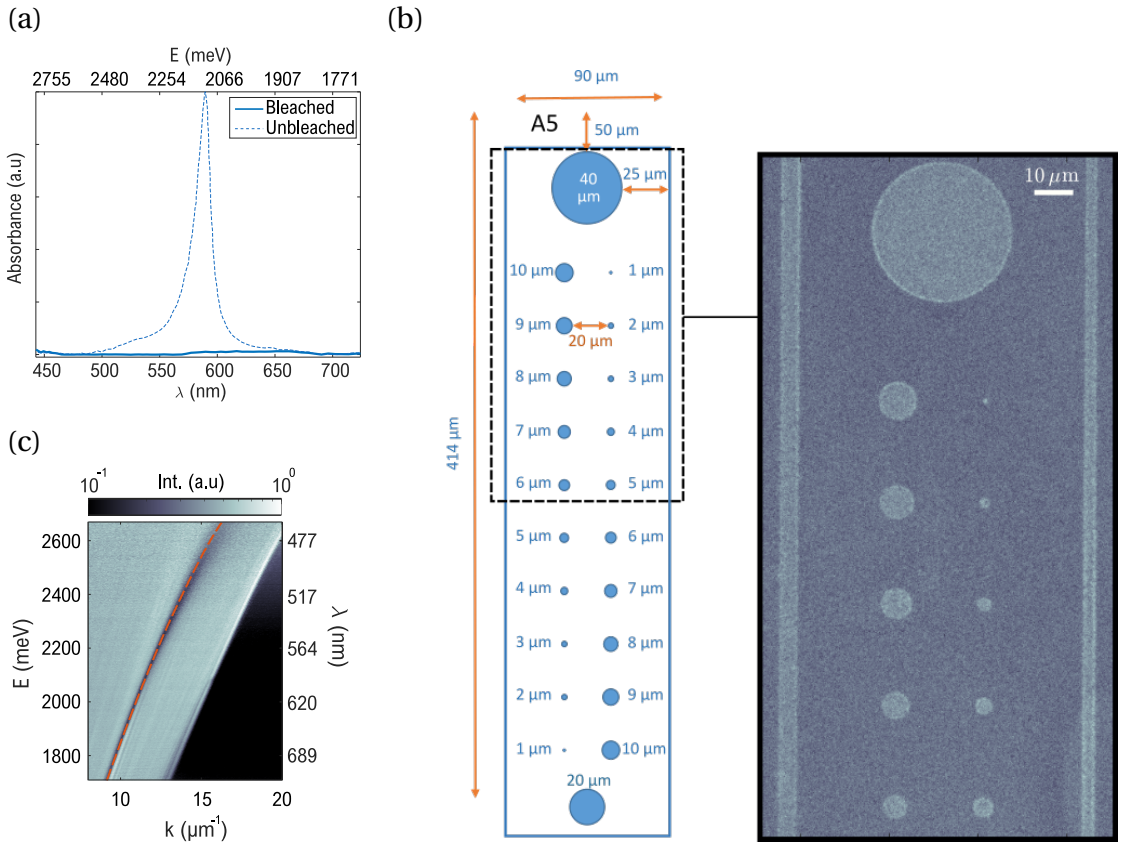


Figure 4.9 – (a) Absorbance spectra of a J-aggregate TDBC thin film before (dashed line), and after (solid line) being photobleached by a 375 nm laser irradiation. It is observed that the irradiated material has the same optical index as the non-irradiated one, except around the 590 nm (2100 meV) region where the sharp absorption peak is eliminated. Image reproduced from [15]. (b) Design of the lithography pattern containing circular photobleached areas (CPAs) with diameters ranging from 1 to 40 $\mu$m. The smallest separation distance between adjacent bleached regions is 20 $\mu$m to isolate them from each other. The pattern was repeated tens of times within the sample to test the reproducibility of the experimental results. Each motif is labeled with a letter and a number in the upper part. The dark-field microscopy image shows the lithography on a J-aggregate TDBC film deposited on silver. (c) Reflectometry measurement under a 6 $\mu$m illumination at the center of a circle of diameter $\varnothing = 40\,\mu$m. The red dashed line shows the reflectance minima of a TMM calculation. The fitted curve uses a layer of 20 nm and a constant refractive index of $n_b = 1.72$.

the upper polariton and with a spectrum which partially overlaps the gap, is labeled RUP1. Finally, the sample with QDs emitting at 544 nm are resonant with the upper polariton and are far from the gap is named RUP2.

The procedure for deposition of the layer is the following. First, we prepare a solution of QDs in toluene with a concentration of $\sim 1\,\mu$M. The concentration was fixed so that the deposited layer was continuous. For this, we first diluted the solution several times in order to spin-coat a low-density layer, observing one single QD for $\sim 10\,\mu m^2$. Then, we raised the concentration by a factor of $10^4$ to have a continuous and homogeneous layer, observed in wide-field fluorescence under the microscope. Transparent Poly(methyl methacrylate) PMMA was added to the solution at a mass concentration of 0.5%. This material determines the thickness of the layer and assures its reproducibility for the different QDs. The spin coating process for the QDs/PMMA solution consists of a single step:
1) time = 60 seconds, speed = 2000 rpm, acceleration = 1000 rpm/sec
Note that the solvent of this second layer is toluene so that the dye layer below does not dissolve during deposition.

After the deposition of the QDs/PMMA layers, the resulting thickness was measured by AFM, giving an average of $\bar{h}_2 = 14.5$ nm. The addition of the second dielectric layer moves the dispersion of the SPP towards higher wavevectors. This is illustrated in Figure 4.10b, in which the dispersion was calculated considering the respective thicknesses and background refractive index for the J-aggregates and QDs layers for each sample. The reflectometry measurements shown in Figures 4.10c, d, and e, were performed in unbleached areas of J-aggregates, where the lithographed disks are not present. We observe that the three samples behave qualitatively similar to a system composed only of J-aggregates and silver. A single anticrossing characterizes the reflectivity dispersions at the energy of the bare J-aggregated TDBC (2101 meV). For sample RUP2, this indicates that the QDs do not enter in strong coupling with the rest of the system. Indeed, if it was the case one would expect to see a second anticrossing around 2279 meV. In samples RLP and RUP1, the QDs have resonances that significantly overlap the gap for which these reflectometry measurements are not sufficient for establishing the coupling regime of the respective QDs. The Rabi splittings found for RLP, RUP1 and RUP2 are 230.3 meV, 152.7 meV and 171.9 meV respectively. The properties of the samples are summarized in table 4.2.

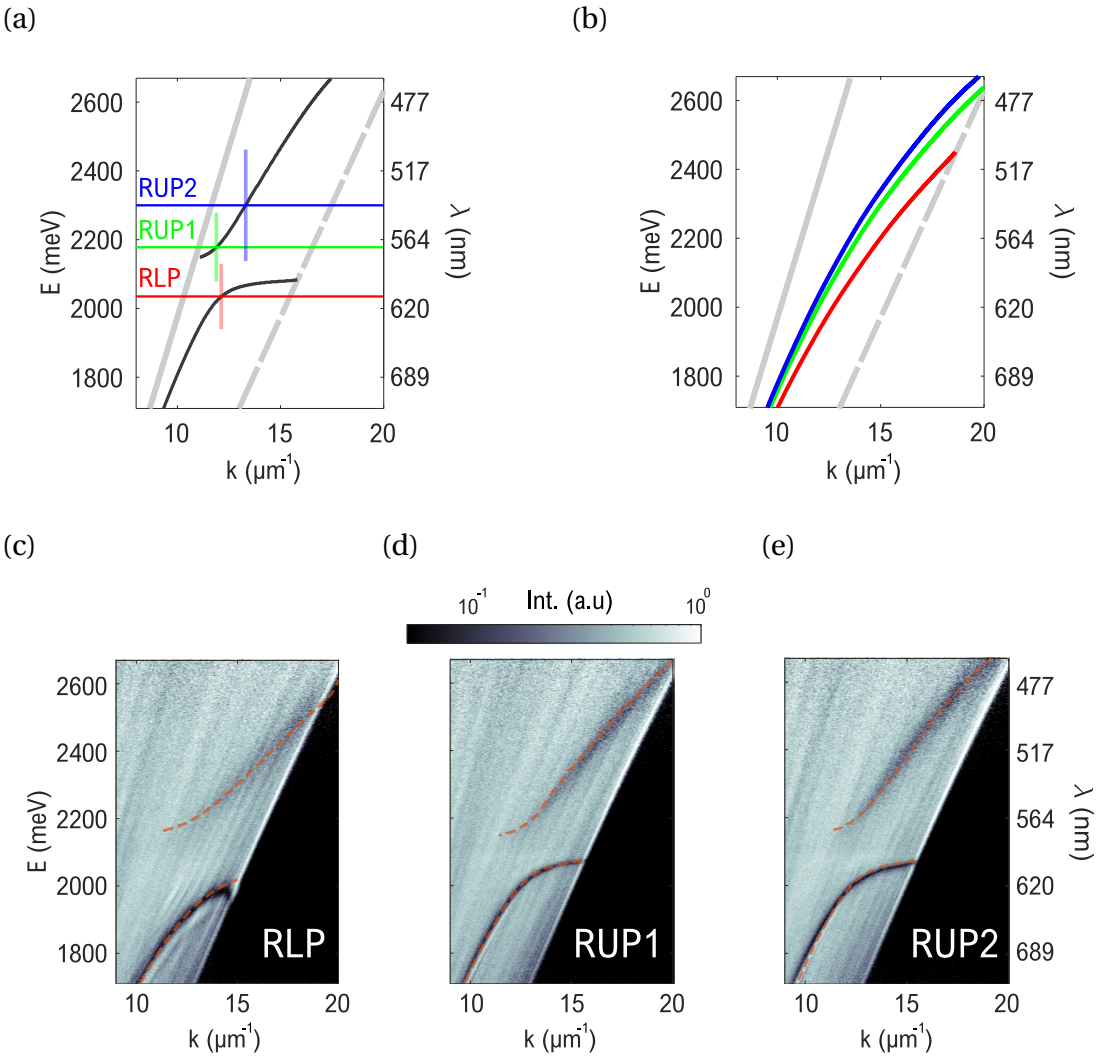


Figure 4.10 – (a) Representation of the spectral relation of the QDs regarding the strongly coupled modes existing in the J-aggregates/Ag system. The samples receive the name of the relative position of the QDs emission with respect to the polaritons: the QDs emitting at 2042 meV are resonant with the lower polariton (sample RLP), at 2156 meV resonant with the upper polariton near to the anticrossing (sample RUP1), and 2279 meV resonant with the upper polariton further away from the gap (sample RUP2). The vertical lines represent the FWHM of the emission peaks, which reveals that the samples RLP and RUP1 have a partial overlap with the gap. (b) Plasmon dispersion ignoring the Lorentzian transition of the J-aggregated TDBC, accounting for the background index of the J-aggregates and the QDs $n_{b1}$ and $n_{b2}$ for the three samples. (c), (d), and (e) show the reflectometry measurements with the respective TMM calculation for the three samples. The Rabi splittings in each sample are $\Omega_{\mathrm{RLP}} = 230.3\,\mathrm{meV}$, $\Omega_{\mathrm{RUP1}} = 152.7\,\mathrm{meV}$ and $\Omega_{\mathrm{RUP2}} = 171.9\,\mathrm{meV}$.

The substantial difference between the Rabi splitting measured in sample RLP and the ones in RUP1 and RUP2 is explained by dissimilar fabrication processes. Sample RLP was fabricated at ILM several months before the fabrication of samples RUP1 and RUP2, which was performed at Institut Langevin. For the same reason, in table 4.2 there are no available data for the AFM measurements to characterize the multiple layers of the sample. By comparing the fitted values of TMM reflectance, we observe that the thickness of the J-aggregates layer of sample RLP is 28 nm, while for the other samples is $\sim 20$ nm. This explains the difference in the observed Rabi splittings, since for thicker layers of J-aggregates the number of emitters that strongly coupled to the SPPs is higher.

| Sample | AFM $h_1$ (nm) | AFM $h_2$ (nm) | TMM $h_1$ (nm) | TMM $h_2$ ($nm$) | $\Omega_R$ (meV) |
|---|---|---|---|---|---|
| RLP | - | - | 28 | 18 | 230.3 |
| RUP1 | 17 | 15 | 20 | 17 | 152.7 |
| RUP2 | 17 | 14 | 19 | 14 | 171.9 |

Table 4.2 – Summary of the properties of the samples studied in this chapter. The thicknesses of the J-aggregates $h_1$ and QDs/PMMA $h_2$ layers, obtained by AFM measurements, are shown in columns 2 and 3. Columns 4 and 5 show the thicknesses used for the TMM reflectance computation of the modes. The AFM measurements for sample RLP are not shown since they were not implemented but several months after its fabrication. The last column shows the value of the Rabi splitting $\Omega_R$ obtained from the TMM calculations. The AFM measurements were performed by Kevin Chevrier.

## 4.2 QDs weakly coupled to polaritons

Besides the case of sample RLP, in which the QDs are resonant with the gap at the anticrossing, the absence of a second anticrossing in the reflectivity, suggests that the QDs are not in strong coupling with the rest of the system. However, the QDs are subject to an electromagnetic environment determined by the hybridization between the J-aggregates and the SPP. This section shows the weak coupling of the QDs to the strongly coupled polaritons through reciprocal-space spectroscopy of the sample luminescence. We explored the interaction of the QDs with the rest of the system by exciting different regions of the sample with a focused 445 nm laser excitation. First, we describe the emission of strongly coupled J-aggregates which relax through the lower polariton. Then, we study for each sample the PL behavior comparing the cases of QDs on large CPAs of $\varnothing = 40\,\mu$m to the situation in which the QDs lay on top of a region that has not been lithographed. Afterward, we show the progressive modification of the QDs radiation pattern from large to small CPAs. The transition from a pure plasmonic SPP towards the emission into the polaritons is determined by the available modes of the surroundings. All the $E(k)$ diagrams shown in this section are TM-polarized to increase the ratio of the signal coming from the polaritonic modes with respect to the uncoupled emission.

### 4.2.1 Luminescence of strongly coupled J-aggregates

To understand the contribution of the QDs to the samples' total luminescence, let us first discuss the emission of the active J-aggregates when they strongly couple to the SPP. Figure 4.11a shows the PL radiation pattern of a layer of J-aggregates excited with a focused 445 nm laser excitation. Remarkably, the luminescence relaxation is observable despite the detuning between the laser excitation wavelength and the absorption peak of the dye ($\lambda = 587$ nm). At subcritical angles, we observe a dispersionless line at the energy of the uncoupled J-aggregate ($E = 2085$ meV, $\lambda = 594$ nm). In the supercritical range, we detect the propagating modes of the system. Although the modes observed in reflectometry measurements presented in the previous section clearly showed the upper and lower polaritons (UP and LP, respectively), bright emission is only observable through the latter.

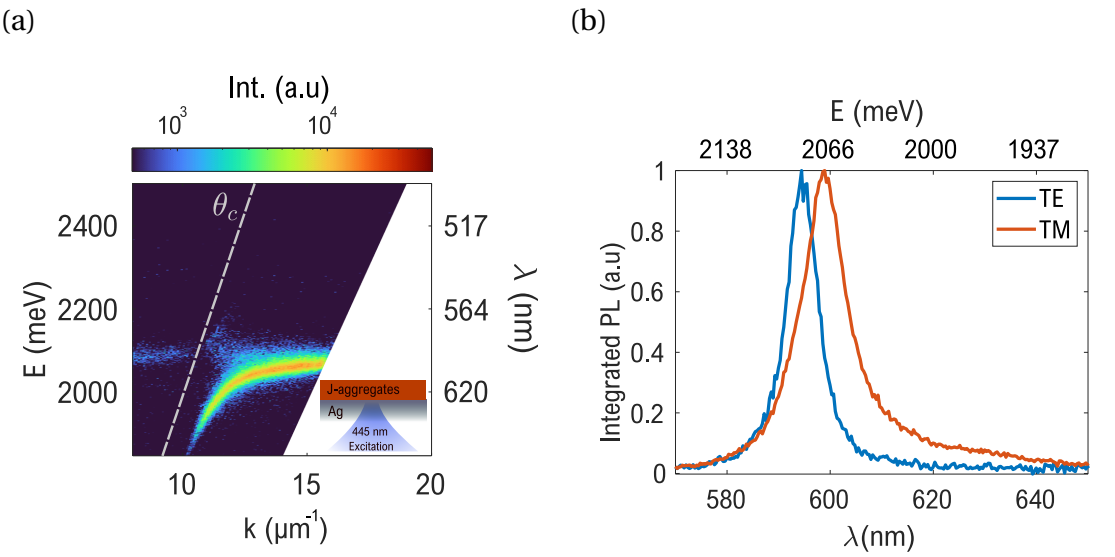


Figure 4.11 – (a) Photoluminescence of a layer of TDBC J-aggregates deposited on silver, excited by a 445 nm laser excitation, as sketched in the bottom right. The luminescence at the emission energy of the aggregates at 2085 meV, clearly observed under the critical angle $\theta_c$ is the so-called incoherent state, which is independent of the polarization detection. In the supercritical emission, light is only present on the coherent lower polariton mode. (b) Integrated supercritical emission spectra. The collected signal was polarized in TE (blue curve) and TM (red curve). Each curve has been normalized by its maximum.

The emission pattern of the strongly coupled system is determined by the interplay of two kinds of excited state within the system. The interaction of the SPP with the J-aggregates molecular excitations creates a coherent state in the medium, leading to their hybridization and to the observation of propagative modes, the lower and the upper polariton.Therefore, the polaritons are called *coherent* states. However, a large part of the excited molecules, emit over a large span of wavevectors, giving rise to non-dispersive, so-called *incoherent*, excited states [20]. The distinction between coherent and incoherent states is a common terminology in the field of strong coupling between organic molecules with photonic modes, and we will adopt it for the rest of this manuscript.

Figure 4.11a shows that the upper polariton branch is not luminescent except in a limited range close to the exciton transition and the critical angle. A possible explanation for this, is that following the non-resonant laser excitation of the system, the upper branch population relaxes non-radiatively into incoherent states through

vibronic channels [21; 22]. In similar systems composed of microcavities containing J-aggregates, pump-probe spectroscopy measurements showed that the scattering of upper branch polaritons to the exciton reservoir occurred with a time constant of (~ 15 fs) [23], which is much faster than the fluorescence lifetime of J-aggregated TDBC (~ 15 ps) [24]. This large difference of two orders of magnitude in time scales could explain the dark character of the upper polariton states, when the only active material in the system are the J-aggregates.

Figure 4.11b shows the integrated PL spectra for supercritical emission. The propagating modes in the sample (e.g., the polaritons) are TM-polarized. For this reason, the TE-polarized spectrum shows the PL emission uncoupled to propagating modes, and it is centered at the wavelength of the bare J-aggregated TDBC. In contrast, the TM-polarized spectrum is red-shifted relative to this value due to the energy gap created at the anticrossing, which reduces the intensity around the excitonic transition. Moreover, the spectrum is broadened towards longer wavelengths since, once the excitations have thermalized to the reservoir of incoherent states, they weakly couple to the LP where their emission is observed [22].

### 4.2.2 QDs resonant with the lower polariton (RLP)

In the sample RLP, the QDs emit at 2042 meV with a spectral width of 95.2 meV (FWHM). Figure 4.12 shows the luminescence emission pattern of the sample for two opposite limiting cases. The first is presented in Figure 4.12a, which shows the emission of QDs excited at the center of a 40 $\mu$m CPA. We observed that the QDs emit efficiently through the SPP mode. The maximum emission is observed at the resonance between the emitters exciton and the SPP at $k = 12.45\,\mu\text{m}^{-1}$. As expected, there is no anticrossing, and the emission follows the SPP dispersion, which is a signature of QDs weak coupling to the plasmonic mode. Also, we observe that light uncoupled to the SPP is more intense in the supercritical range than in the subcritical. Away from the energy resonance, the signal is only detected within wavevectors close to the SPP dispersion.

Figure 4.12b shows the emission of QDs excited on top of a non-lithographed homogeneous zone. In this case, the emission is directed mainly through the LP created by the coupling of active J-aggregates. The intensity of the LP is higher around

(a) (b)

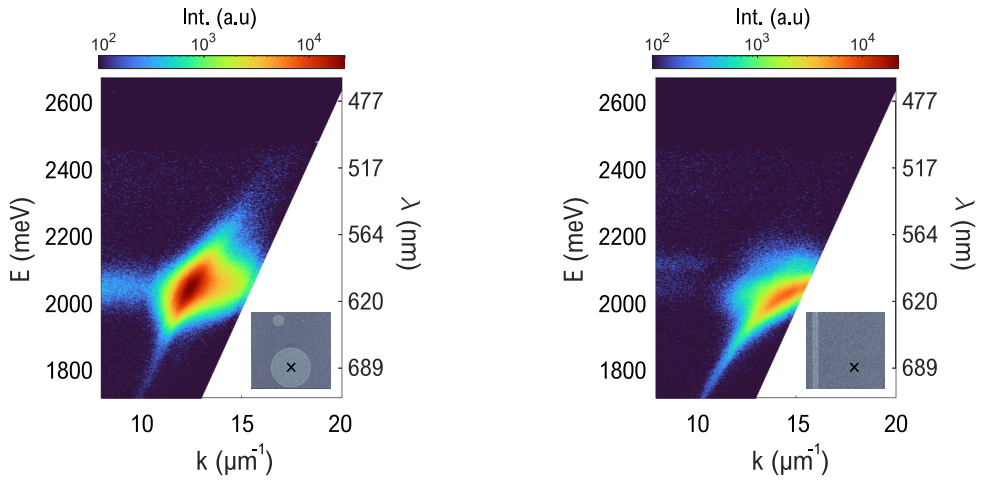


Figure 4.12 – Luminescence dispersion QDs excited on top of (a) a large CPA of $\varnothing = 40\,\mu$m emitting through the plasmonic mode and (b) an unbleached area with active J-aggregates in which the emission is channeled through the LP of the strongly coupled system. Note that the colormap has the same scale for both figures.

the QDs exciton, in contrast to Figure 4.11a, in which the intensity is more homogeneously distributed along the LP branch. The absorption of the J-aggregates at different wavelengths explains the reduced intensity of the polaritonic emission. First, the high energy tail of the QDs emission has a significant overlap with the absorption peak of the dye, for which energy transfer is possible. Second, as we observed in the previous section, the J-aggregates can fluoresce under the excitation of the 445 nm laser pump. Therefore, when the laser impinges in a region where the J-aggregates are active, both species of emitters absorb, while in the CPA of $\varnothing = 40\,\mu$m only the QDs get excited.

The transition of the QDs emission, from the SPP mode in the $40\,\mu$m CPA to the polariton weak coupling was investigated by observing the luminescence of the QDs in CPAs of different diameters. Figure 4.13 shows the progressive modification of the emission going from a large diameter CPA of $\varnothing = 20\,\mu$m down to the smallest CPA of $1\,\mu$m. Three effects can be distinguished by observing the luminescence behavior as the CPA diameter is reduced. The first is the progressive broadening of the SPP mode. As we previously noticed, the SPP is not defined outside the photobleached areas.

The reduction of the CPAs diameter spatially confines the SPP, and the wavevector distribution $\Delta k$ is increased. However, the emission maxima of the light coupled to the SPP is maintained around the same wavevector $k \sim 12.45\,\mu\text{m}^{-1}$ until the CPA of $7\,\mu m$. For smaller CPAs, the $k$-coordinate of the maxima starts to shift towards the lower polariton.

The second effect consists of the increasing intensity of the LP emission. For large CPAs $\varnothing > 6\,\mu\text{m}$, the observation of light coming from the LP is explained by the excitation of active J-aggregates in the surroundings. Scattered laser from the excitation focus and propagating SPPs at the laser wavelength reach the edge of the CPAs, therefore directly exciting the J-aggregates. Since the detection field-of-view is $20\,\mu\text{m}$ large, the luminescence coming from a spatially extended area located far-away from the excitation spot can be detected. For smaller diameters $\varnothing < 6\,\mu\text{m}$, there is an additional contribution. The broadening of the SPP emission reduces the momentum mismatch between the modes existing inside the CPA (e.g., the SPP) and outside (e.g., the LP). In this way, the high wavevector fraction of the SPP can go through the barrier and contribute to the LP emission.

The last effect observed in Figure 4.13 is the distribution of the PL emission within the $E(k)$ space. Besides the intensity relation between the SPP and LP modes discussed above, light emitted through the UP comprehended around $2100-2200\,\text{meV}$ is observed for diameters $\varnothing < 4\,\mu\text{m}$. Even though there is light at the same energy band for larger CPAs, the overlap with the SPP makes it impossible to distinguish the UP. In contrast, in the small CPAs, the bending, characteristic of the UP, is clearly defined. Moreover, the subcritical emission of the emitters is enhanced in the same areas.

To study the spectral behavior of the system as we reduce the CPA diameter, we integrated the TM-polarized $E(k)$ luminescence measurements, as shown in Figure 4.14a. The reference CPA of $\varnothing = 40\,\mu\text{m}$ shows the QDs spectra centered at their exciton wavelength $\lambda = 607\,\text{nm}$ (2042 meV). As the CPA diameter is reduced, the total PL intensity decreases, and the emission peak red-shifts up to 614 nm. The apparent spectral modifications are the consequence of two complementary effects. As the coupling between the QDs and the LP increases by reducing the CPA, the emission around 2042 meV is channeled through the high-wavevector range of the LP, which extends beyond the objective's numerical aperture (at $k = 15.42\,\mu\text{m}^{-1}$ for

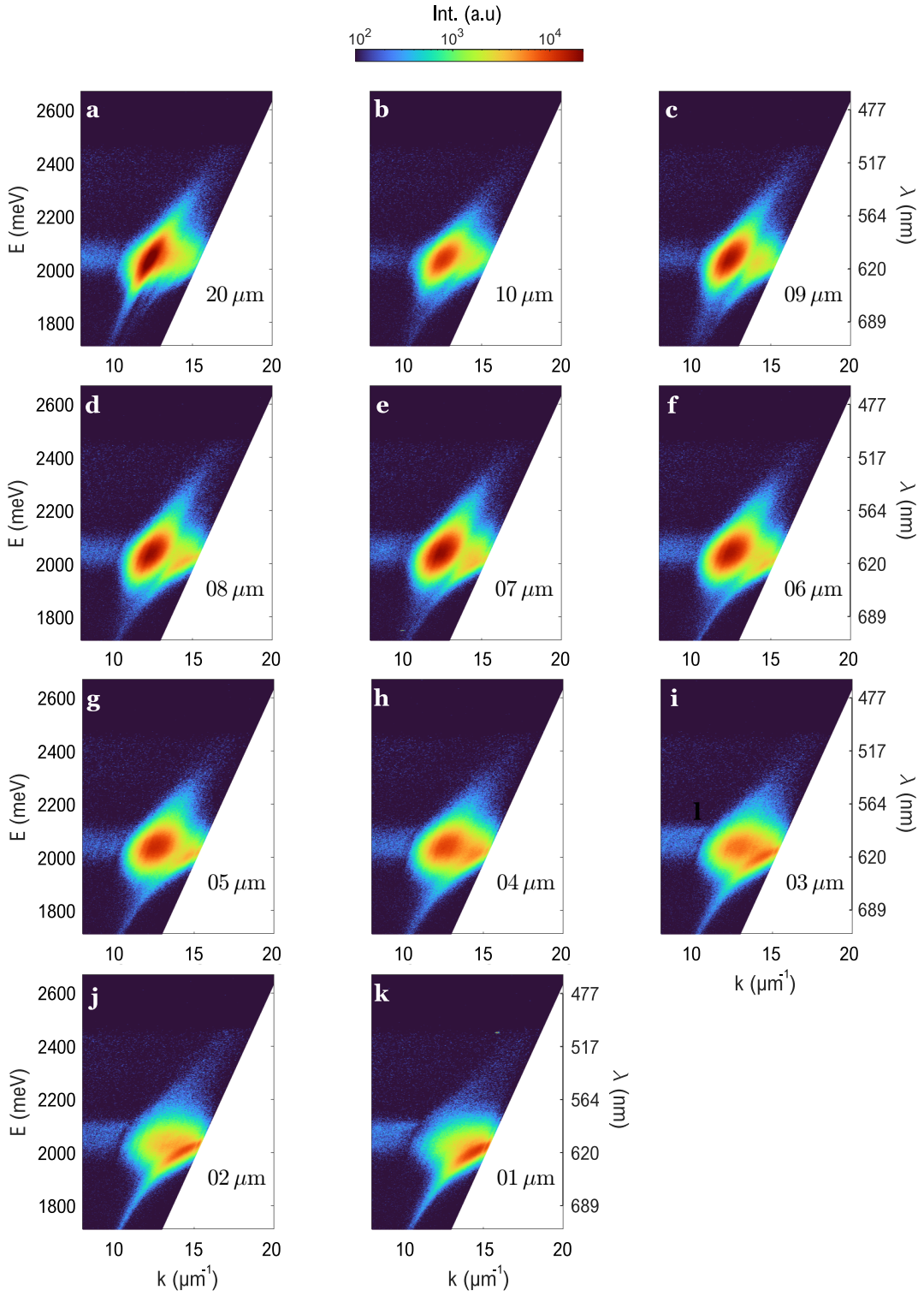


Figure 4.13 – (a)-(k) Luminescence dispersion observed by focusing the laser at the center of the circular photobleached areas (CPAs). The diameter is indicated in the lower right corner of each image. Note that the colormap scale is the same for all images.

(a) (b)

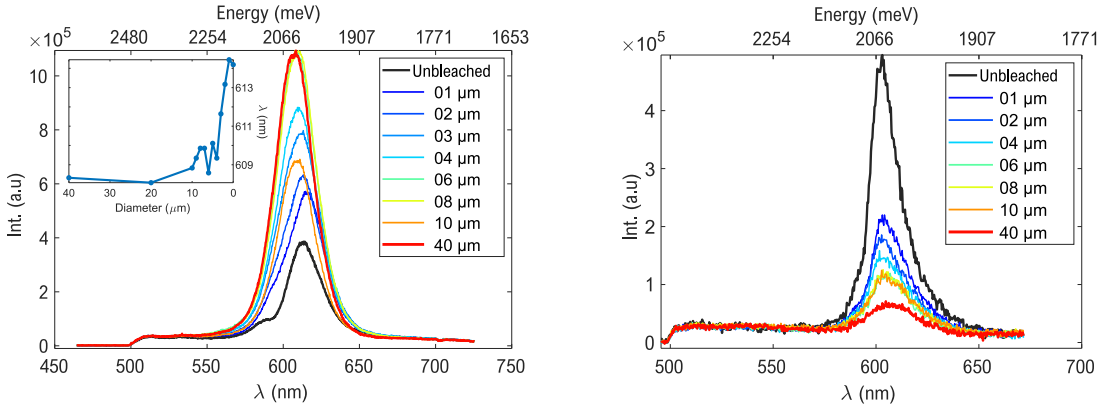


Figure 4.14 – (a) Integrated TM-polarized spectra showed for all CPAs diameters. The total intensity decreases as the size of the CPA is reduced. The inset shows the shift of the emission maxima of the QDs as a function of the diameter of the CPAs. (b) Integrated TE-polarized spectra. Reducing the diameter of the CPAs entails an increasing intensity for the emission peak.

$E = 2042\,\text{meV}$). At the same time, the QDs short-wavelength emission tail overlaps with the gap at the anticrossing, where the density of states at these wavelengths is reduced. As a result, the integrated spectrum of the system is red-shifted and smaller relative to the reference CPA of $\varnothing = 40\,\mu\text{m}$.

The integrated TE-polarized spectra, presented in Figure 4.14b, show the inverse behavior relative to the TM-polarization. The intensity dependence with the diameter of the CPA is inversed, and larger diameters showed smaller intensity peaks. This is produced because, in smaller CPAs, the J-aggregates are directly excited, and we observe the emission of the incoherent states. However, the impossibility of spectrally separating the QDs emission from the incoherent J-aggregates restrains the characterization of the QDs intensity as a function of the CPA size.

### 4.2.3 QDs resonant with the upper polariton (RUP1)

Now we show the results of the sample RUP1, in which the QDs emission is resonant with the low energy range of the upper polariton ($E = 2156\,\text{meV}$), and its spectral width overlaps with the gap. Figure 4.15a shows the emission of QDs excited at

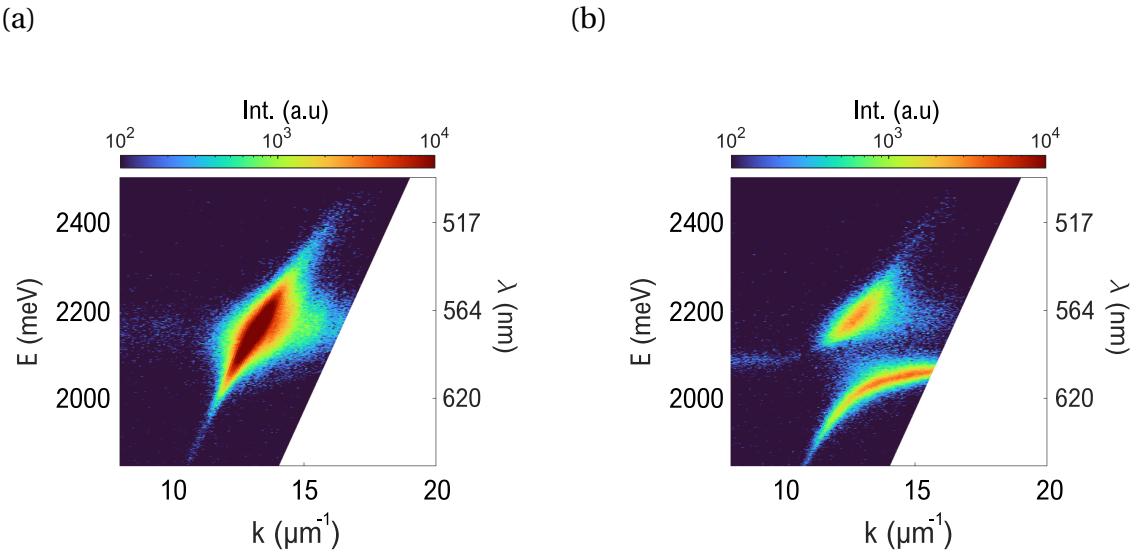


Figure 4.15 – Luminescence dispersion of the QDs (a) in a large CPA of $\varnothing = 40\,\mu$m emitting through the plasmonic mode and (b) where the J-aggregates are unbleached, in which the emission is channeled through the strongly coupled modes. Note that the spectrum of the QDs overlaps with the gap around the anticrossing and both polaritons.

the center of a $40\,\mu$m CPA. We observed the efficient channeling of the QDs radiation through the narrow SPP mode. Figure 4.15b shows the emission of QDs excited on top of a non-lithographed homogeneous zone. Remarkably, we observe that the emission of the QDs is partially channeled through the UP of the strongly coupled system. As discussed in the previous section, the UP state has a negligible PL when the only active emitters in the system are the J-aggregates.

Similar to the RLP sample, we observed the progressive modification of the QDs coupling to the sample modes, from Figure 4.15a to Figure 4.15b, by exploring CPAs of intermediate diameters. Figure 4.16 shows this progression. Again, we observe the broadening of the SPP-like mode while reducing the diameter of the CPAs. For large CPAs $\varnothing \leq 6\,\mu$m, diffracted modes can be observed at higher wavevectors. The separation of the central SPP and such modes in the wavevector axis $\delta k = 2\pi/(\varnothing/2)$ suggests that they are the result of SPPs leaking inside the CPA which are scattered at its edge. As the CPAs get smaller, the modes get much broader, and the QDs are better and better coupled to the upper polariton.

Figure 4.17a and 4.17b show the TM and TE-polarized integrated spectra, respec-

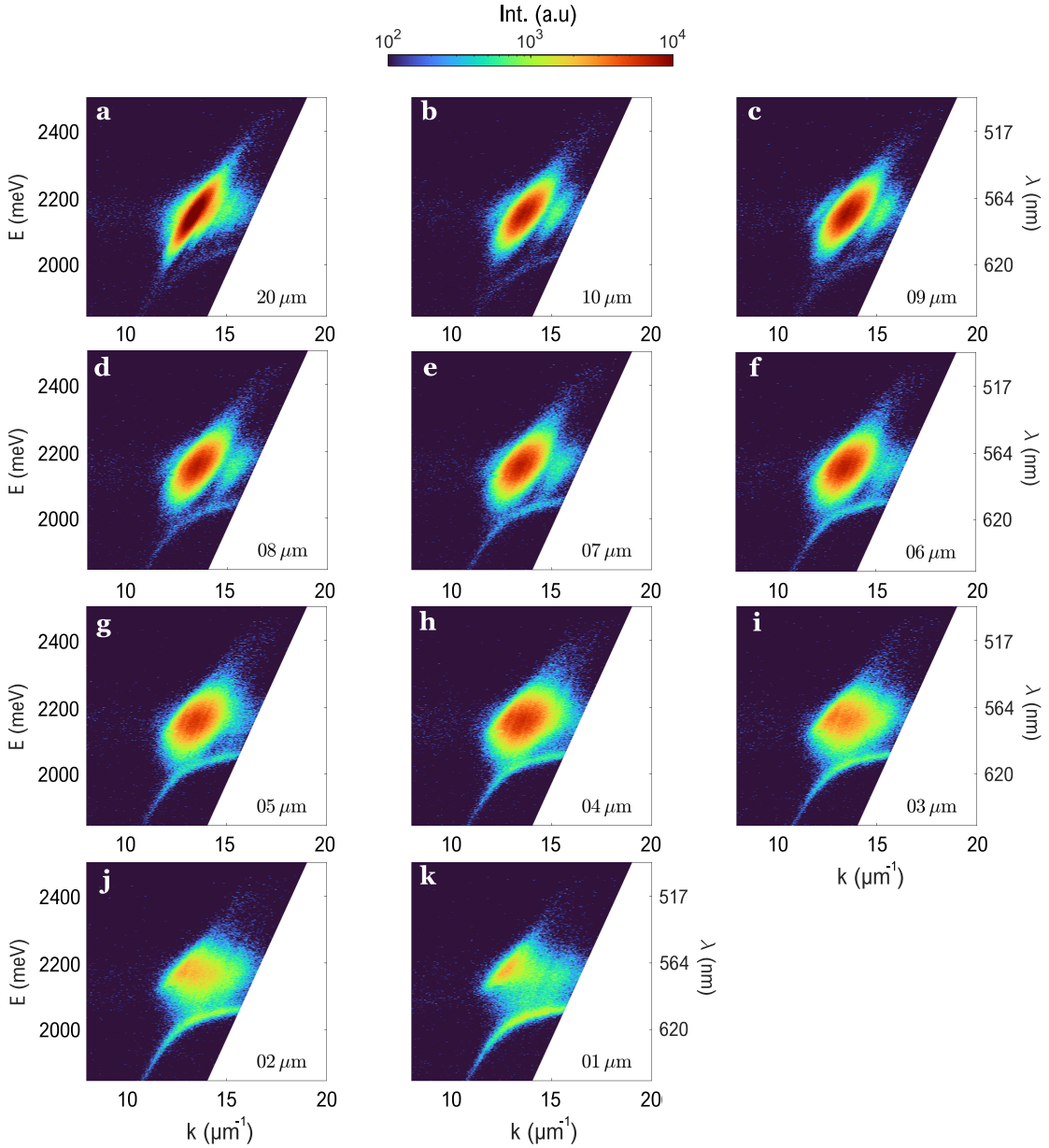


Figure 4.16 – (a)-(k) Luminescence dispersion observed by focusing the laser at the center of the CPAs. The diameter is indicated in the lower right corner of the dispersion images.

(a) (b)

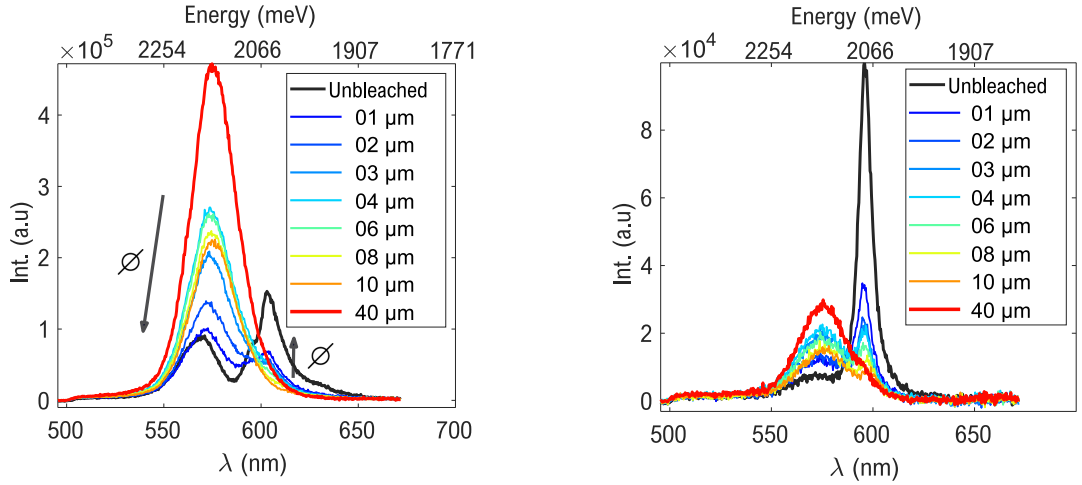


Figure 4.17 – Integrated (a) TM and (b) TE-polarized luminescence spectra. There is a shift of the emission of the QDs towards shorter wavelengths caused by the gap of the SC system.

tively. In both cases, the emission peak of the QDs is reduced in intensity as the CPAs diameter decreases. In Figure 4.16 the QDs progressively couple to the polaritonic states, so that we observe their emission going through this mode. However, the QDs emission can also be absorbed by the coherent UP states, which have efficient non-radiative relaxation pathways. Moreover, a blue shift is observed while reducing the CPA diameter. This is the result of the overlap of the QDs with the gap at the anticrossing, between (2060 – 2120 meV) where there are no available TM-polarized modes through which they could emit. Figure 4.17b shows a similar behavior, but the blue shift of the QDs can be due to the absorption of the uncoupled J-aggregates. The rich competition of effects present in this sample is examined more in-depth in section 4.3.

### 4.2.4 QDs resonant with the upper polariton (RUP2)

The last sample that we analyzed is RUP2, in which the top layer is constituted by QDs emitting at 2350 meV embedded in PMMA. This emission is resonant with the upper polariton and overlaps with the gap at only its low-energy range spectrum, beyond its FWHM. Figure 4.18a shows the emission of QDs excited at the center of a 40 $\mu$m CPA.

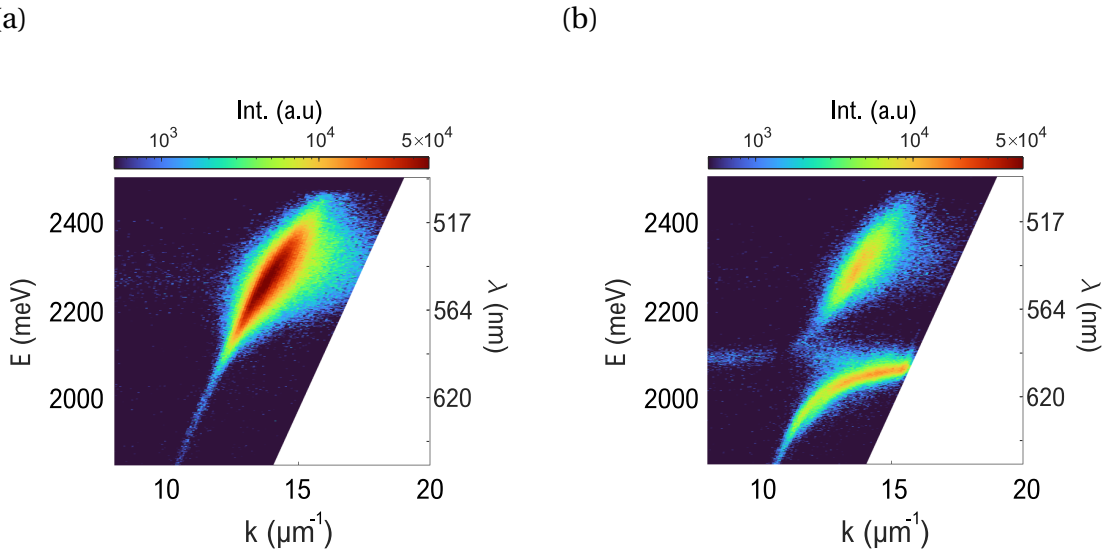


Figure 4.18 – Luminescence dispersion of the QDs (a) in a large CPA of $\varnothing = 40\,\mu$m emitting through the plasmonic mode and (b) where the J-aggregates are unbleached, in which the emission is channeled through the strongly coupled modes. Note that the spectrum of the QDs overlaps with the UP at their central emission wavelength, and the overlap with the gap is beyond its FWHM.

We observed the efficient channeling of the QDs radiation through the narrow SPP mode. Figure 4.18b shows the emission of QDs excited on top of a non-lithographed homogeneous zone. Once again, we observed the QDs emission channeled through the UP and a fraction of the spectrum that overlaps the gap between the UP and the LP.

The modification of the luminescence as a function of the CPA diameter is shown in Figure 4.19. As the CPA size is reduced, the main observed effect is the broadening of the mode. The transition of the SPP emission towards the upper polariton is less pronounced relative to samples RLP and RUP1 because the wavevector mismatch between the SPP and the upper polariton is smaller. In this way, the QDs maximal emission remains approximately at a constant wavevector as a function of the CPA diameter. However, since the low-energy tail of the QDs spectrum overlaps the gap, it is observed how the emission between (2060 – 2120 meV) is present for large diameters and gradually disappears at this range. Figure 4.20a shows the integrated TM-polarized spectra for different CPAs. As the CPAs become smaller, the QDs emis-

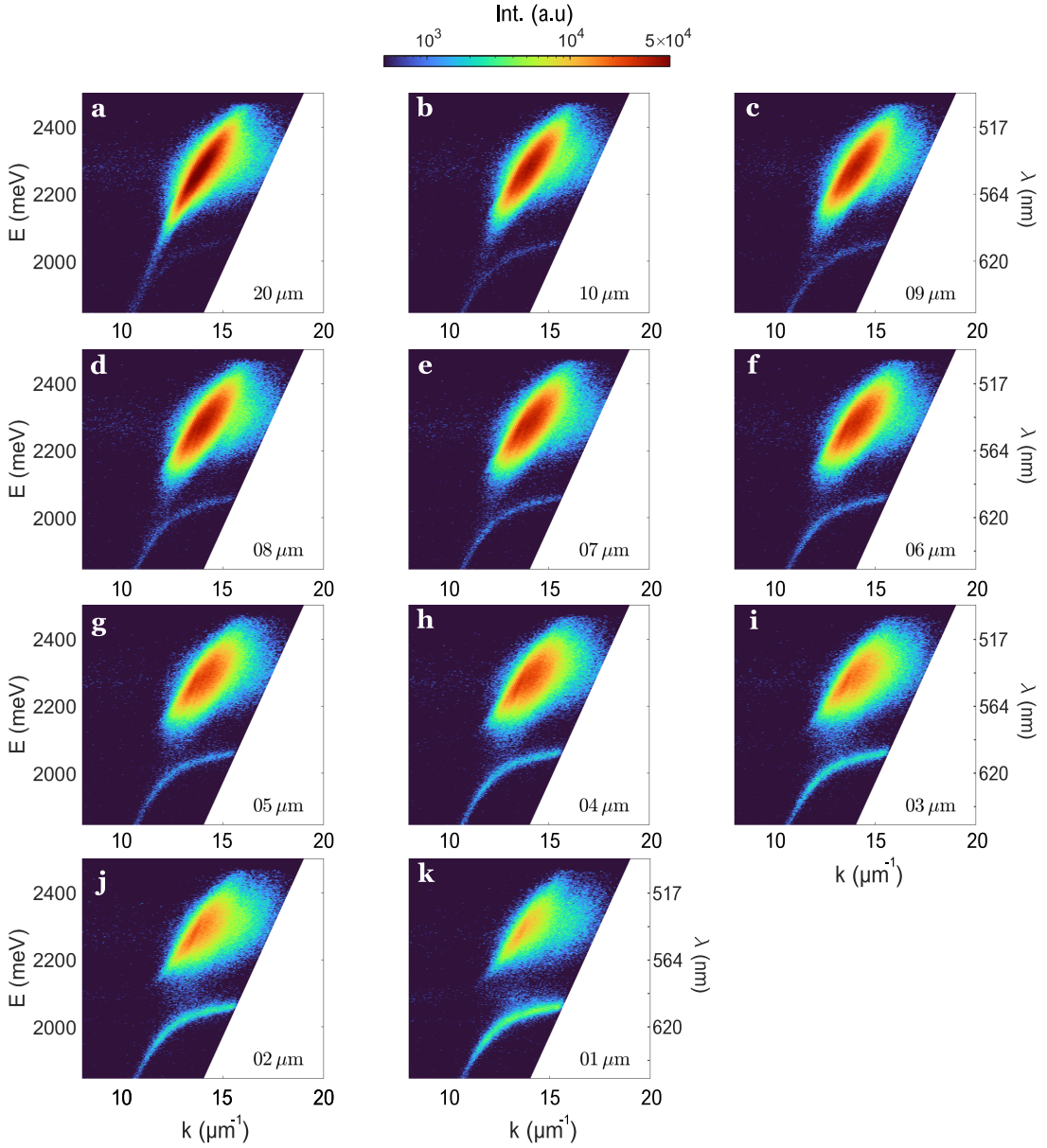


Figure 4.19 – (a)-(k) Luminescence dispersion observed by focusing the laser at the center of the CPAs. The diameter is indicated in the lower right corner of the dispersion images.

(a) (b)

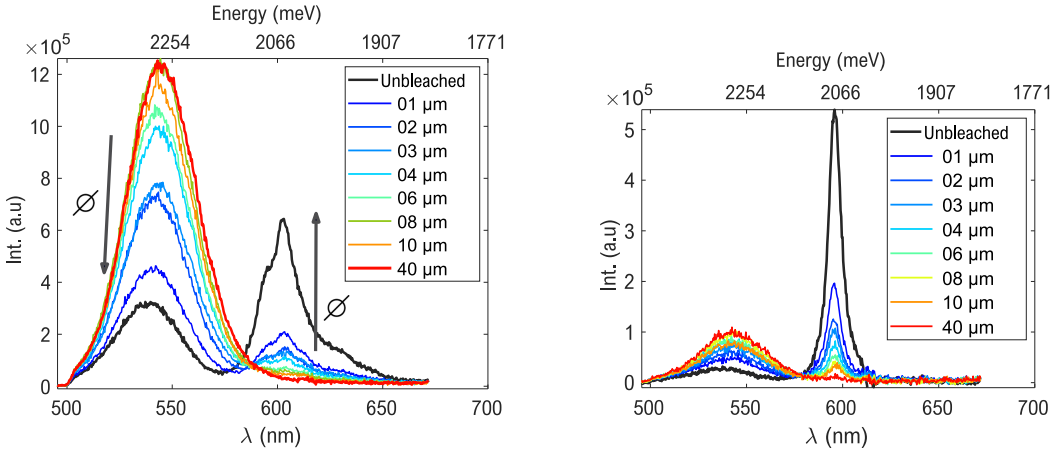


Figure 4.20 – Integrated (a) TM and (b) TE-polarized luminescence spectra. A shift of the emission of the QDs towards shorter wavelengths is caused by (a) the presence of the gap and (b) the direct absorption of the J-aggregates.

sion peak weakly coupled to the propagating modes presents a blue shift. Similar to sample RUP1, this is caused by the progressive coupling from the QDs to the polaritons and the concomitant appearance of the gap centered at ~ 2090 meV. In Figure 4.20b, the TE-polarized emission is shown, and a similar shift can be observed. In this case, the small shift is probably the result of the absorption of the uncoupled J-aggregates.

Through this section, we have observed that the coupling of the quantum dots to the strongly coupled system, follow similar tendencies in the three studied samples. For instance, the broadening of the propagating modes for small CPAs is always observed, as the progressive modification from the SPP to the polaritons emission. Also, by reducing the diameter of the CPA, we observe the decreasing amount of light detected at energies comprehended in the gap around the anticrossing of the strongly coupled system. However, a quantitative comprehension of the observed phenomenon is delicate mainly due to two issues. The first one is the repeatability of the J-aggregated deposition layer. Although careful attention is taken for the deposition procedure of the J-aggregates, it remains inevitable to observe areas with an inhomogeneous Rabi splitting within the same sample. If this point has a reduced

importance when the excitation is performed in wide-field, because the extension of the field averages over the inhomogeneity, attention must be payed with a focused excitation. However, it is important to notice that we repeated our measurements on several samples and that the qualitative behavior is very well reproduced. The second issue relies in a residual PL that can be observed on a control sample with CPAs and a J-aggregate layer before the deposition of the QDs layer. The experiment is performed in the same way as for the samples with the QDs layer. Data are reported in Appendix A. We notice that the signal coming from direct excitation is lower than the signal detected on the sample with QDs' layer, which is a proof that the majority of the signal is due to energy transfer.

In the next section we will show that a numerical modeling of the PL data is possible with a formalism based on the Kirchhoff's law. This approach has been developed and applied to our data by the team of Jean-Jacques Greffet at Laboratoire Charles Fabry (LCFIO).

## 4.3 Model based on local Kirchhoff's law for photoluminescence

This section shows how the multilayered system behavior composed of the silver film, the J-aggregates, and the QDs is reproduced by modeling its photoluminescence using the local form of Kirchhoff's law, which extends the validity of the Kirchhoff law to non-isothermal bodies with photons with non-zero chemical potential [25]. We used a local Kirchhoff's law establishing the equality between the local absorption rate and the local emission rate in a multilayered structure that accounts for the glass substrate, the silver thin film, and the layers of J-aggregates and QDs. It has been shown [25] that the local Kirchhoff's law can be used to model the photoluminescence of semiconductors (such as QDs) and dye molecules (such as TDBC). This theoretical frame is therefore well-adapted to the description of the samples studied in this manuscript. We started the study with the sample RUP1 containing QDs that emit at 2156 meV, assuming that in both active layers, the ensemble of emitters is thermalized.

The luminescence of such materials can be regarded as thermal emission, with

a finite chemical potential for photons $\mu$ accounting for the number of emitters in the excited state [26]. In this manner, the modified Kirchhoff law including the photon chemical potential is given by the product of the absorptivity by the generalized Planck's blackbody radiance $B(T,\omega-\mu/\hbar)=B(T,\omega,\mu)$ [25; 26]: Explicitly,

$$B(T,\omega,\mu)=\frac{\omega^2}{8\pi^3c^2}\frac{\hbar\omega}{\exp(\frac{\hbar\omega-\mu}{k_BT})-1} \tag{4.1}$$

where $T$ is the body temperature, $\omega$ the frequency, and $\hbar$ is the Planck constant. Therefore, the total power emitted by a thermalized system, in the solid angle $d\Omega$ within a spectral range $d\omega$ is

$$S(\Omega,\omega)=\frac{dP_e^{(l)}}{d\Omega\,d\omega}=\int_V d^3\mathbf{r}'\alpha_{abs}^{(l)}(-\mathbf{u},\mathbf{r}',\omega)\times B(T,\omega,\mu) \tag{4.2}$$

where $\alpha_{abs}^{(l)}$ is the absorption cross-section density which depends on the system shape and relative orientation to incident light, $\mathbf{u}$ the direction of the incident mode, $\mathbf{r}'$ the position coordinate of the absorber, and the superscript $l$ specifies the polarization [25]. Our sample consists of a system that is isotropic in a given plane. In order to establish the angular dependence with the axis normal to such plane, we write equation C.6 as a function of the solid angle $\Omega$:

$$S(\Omega,\omega)=A(\Omega,\omega)\times B(T,\omega,\mu) \tag{4.3}$$

To account for the emission of the J-aggregates and the QDs we consider the total emission as the sum of the individual photoluminescence of each layer:

$$\frac{S(\Omega,\omega)}{S(\Omega,\omega_0)}=\frac{A^{\text{Jagg}}(\Omega,\omega)\times B^{\text{Jagg}}(\omega,T,\mu_{\text{Jagg}})+A^{\text{QDs}}(\Omega,\omega)\times B^{\text{QDs}}(\omega,T,\mu_{\text{QDs}})}{A^{\text{Jagg}}(\Omega,\omega_0)\times B^{\text{Jagg}}(\omega_0,T,\mu_{\text{Jagg}})+A^{\text{QDs}}(\Omega,\omega_0)\times B^{\text{QDs}}(\omega_0,T,\mu_{\text{QDs}})} \tag{4.4}$$

where the magnitudes calculated at $\omega_0$ are an arbitrary normalization parameter used for all our calculations. The choice of $\omega_0$ is also arbitrary, with the only condition that $S(\Omega,\omega_0)\neq 0$ and $A(\Omega,\omega_0)\neq 0$.

By using Wien's approximation ($\hbar\omega >> k_BT$):

$$B(T,\omega,\mu) \approx \frac{\omega^2}{8\pi^3 c^2} \frac{\hbar\omega}{\exp(\frac{\hbar\omega-\mu}{k_B T})} = B'(\omega) \times \exp(\mu/k_B T) \tag{4.5}$$

we obtain a further simplication:

$$\frac{S(\Omega,\omega)}{S(\Omega,\omega_0)} = \frac{B'(\omega)}{B'(\omega_0)} \frac{A^{\text{Jagg}}(\Omega,\omega) + A^{\text{QDs}}(\Omega,\omega) \times \exp(\Delta\mu/k_B T)}{A^{\text{Jagg}}(\Omega,\omega_0) + A^{\text{QDs}}(\Omega,\omega_0) \times \exp(\Delta\mu/k_B T)} \tag{4.6}$$

which, by using a similar definition as in equation C.7, can also be written as a function of the power emitted by each layer $S^{\text{Jagg}}(\Omega,\omega,\mu_{\text{Jagg}})$ and $S^{\text{QDs}}(\Omega,\omega,\mu_{\text{QDs}})$ with a null chemical potential

$$\frac{S(\Omega,\omega)}{S(\Omega,\omega_0)} = \frac{S^{\text{Jagg}}(\Omega,\omega,\mu_{\text{Jagg}}=0) + S^{\text{QDs}}(\Omega,\omega,\mu_{\text{QDs}}=0) \times \exp(\Delta\mu/k_B T)}{S^{\text{Jagg}}(\Omega,\omega_0,\mu_{\text{Jagg}}=0) + S^{\text{QDs}}(\Omega,\omega_0,\mu_{\text{QDs}}=0) \times \exp(\Delta\mu/k_B T)} \tag{4.7}$$

We observe in the last expression that the photoluminescence of our system equals the sum of the thermal radiation of both layers, with the emission of the QDs weighted by the chemical potential difference of the emitters ensembles. Figure 4.21a and 4.21b show the independent emission of both type of emitters coupled to the polaritonic modes of the sample. Figure 4.21c is calculated using the free parameter $\Delta\mu$ to fit the relative intensity observed in the experimental data (Figure 4.15b).

The fitted value for the difference in the chemical potential is $\Delta\mu = \mu_{\text{QDs}} - \mu_{\text{Jagg}} = 192\,\text{meV}$, which is an estimate of the energy transfer between the QDs layer towards the J-aggregates. In fact, eq. 4.6 and 4.7 tell that when $\Delta\mu > 0$, the number of excited QDs is larger than the number of excited J-aggregates, since the chemical potential is a measurement of the number of emitters that are excited in a respective medium. In the case of the samples with CPAs, we would expect that the difference in the chemical potential increases with the size of the hole because the number of excited J-aggregates decreases. The value of $\Delta\mu$ is a relative measure that has to be compared with similar simulations for CPAs of different diameters. We may also note an important point. For the moment, this simulation does not account for the possible direct excitation of the J-aggregates by the laser. In the presence of a direct excitation, the number of J-aggregate molecules that are excited via an energy transfer from the QDs would then be smaller than without a direct excitation, which makes it delicate to have a quantitative estimate of the emitters that participate to the energy

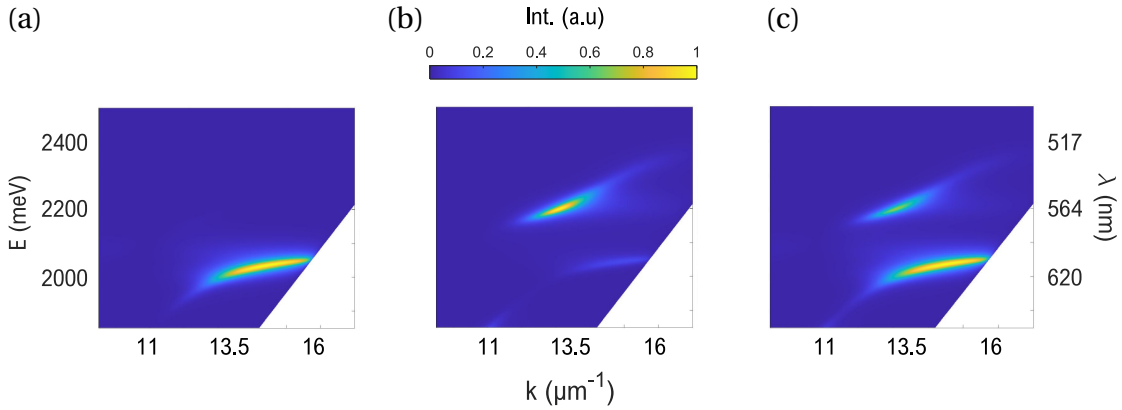


Figure 4.21 – Calculation of the emission pattern of a multilayered system composed by a glass substrate, a silver thin film $h = 50\,\text{nm}$, a layer of TDBC J-aggregates $h_1 = 18\,\text{nm}$ and a layer of QDs $h_1 = 15\,\text{nm}$ with a emission at 2156 meV. The method uses a Rigorous Coupled Wave Analysis (RCWA) algorithm with the Kirchhoff model described in the main text. The independent emission of the layers is shown in (a) for the J-aggregates and in (b) for the QDs layer. (c) shows the system intensity fitting the model to the experimental data shown in Figure 4.15(b). The obtained free parameter is $\Delta\mu = 192\,\text{meV}$.

transfer. Current development of these calculations is being carried on, at the time that this manuscript is being written.

## 4.4 Decay rate measurements

In the previous section, we observed the progressive modification of the emission pattern of QDs positioned by changing the amount of strongly coupled J-aggregates in their vicinity. The strongly coupled system modifies the electromagnetic environment, characterized by a given local density of states (LDOS). In turn, the LDOS determines the spontaneous decay rate $\Gamma$ of a dipole emitter, weakly coupled to the field, in a corresponding medium. This section shows an extract of a series of decay rate measurements of the QDs in different environments produced by the CPAs. Through these observations, we attempted to characterize the progressive modification of the modes to which the QDs couple and possible mechanisms of energy transfer among the J-aggregates and the QDs. However, the non-monoexponential character of the decay histograms and the presence of a long-lifetime component, made it difficult to draw strong conclusions from our experimental data. In this section we will summa-

rize some of the measurements that we performed.

We excited the system in the same way as in the experiments shown in the previous section. We pumped it by focusing the 445 nm laser in unbleached J-aggregates regions and afterward in the center of CPAs with different diameters. However, the detection field of view for the decay rate measurements corresponds to an area of the sample plane of a diameter of 1 $\mu$m. Therefore, when we observe the light coming of excited QDs at the CPAs centers, we exclude the contribution of the incoherent J-aggregates but we do not discard the possibility that the propagating coherent waves are detected. The luminescence of the latter is characterized by a fast decay rate $\sim 1/15\,\mathrm{ps}^{-1}$.

In the three different samples, we expected varied behaviors of the QDs decay rate. For example, in sample RLP where the QDs are resonant with the lower polariton, the number of polaritonic states resonant with the QDs energy is large, so that an enhancement of $\Gamma$ (which is the inverse of the lifetime) is expected when the size of the CPAs decreases. In contrast, in sample RUP2, the modification from the SPP to the polaritons is relatively smaller, and therefore the expected LDOS variation (and thus $\Gamma$ variation) as well.

Normalized decay rate histograms for the samples RLP, RUP1, and RUP2 are shown in Figures 4.22a, 4.22b, and 4.22c, respectively. The measurements of the three samples share general features. First, we note that the direct contribution of the J-aggregates is observed only for unbleached regions where the dye is active. Even though this fast component is characteristic of the J-aggregates, we are not able to discard that QDs with a large enhancement of their decay rate contribute to this component. Second, we observe a time when the histograms converge to the same decay slope, independently of the CPA at which the QDs are measured. For example, for the sample RLP (Figure 4.22a), this time is around 20 ns. Surprisingly, we observe that besides the direct contribution of the fast J-aggregate decay, the histograms for the large 40 $\mu$m CPA and the unbleached zone have a parallel slope. The histograms for 1 and 2 $\mu$m, show a different behavior for short times $t < 5$ ns. However, we could not identify a trend relating the size of the CPAs with the decay rates, and we concluded that the observed modifications are due to fluctuations of the sample homogeneity.

A similar result is observed for sample RUP1 in Figure 4.22b. The decay slopes are not significantly modified by changing the environment probed by the QDs. In

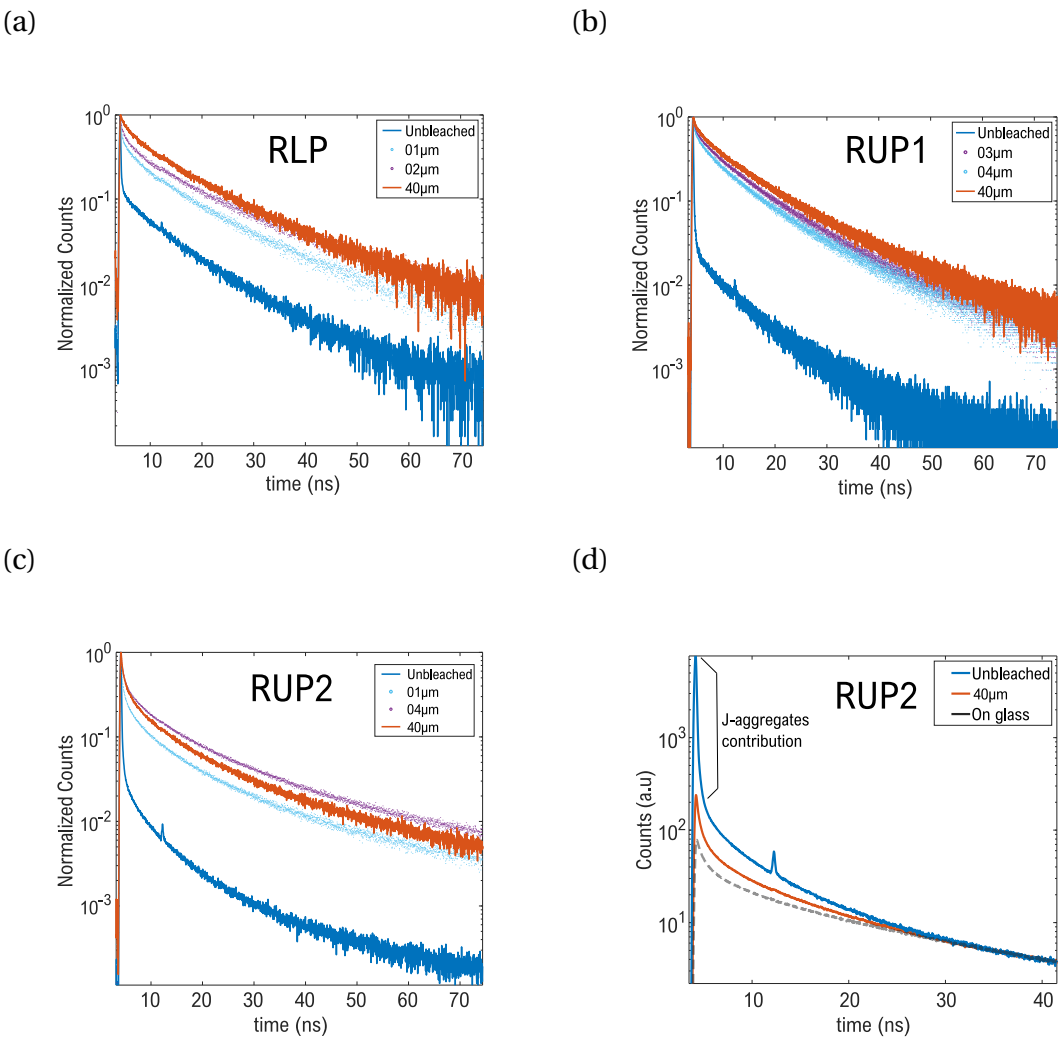


Figure 4.22 – Decay rate histograms for samples RLP, RUP1 and RUP2. In (a), (b) and (c) the normalized decay rates histograms are normalized at the maximum value. The histograms correspond to measurements obtained by exciting the QDs at unbleached zones where there are active J-aggregates (blue curve), large $\varnothing = 40\,\mu$m CPAs (red curve), and at small CPAs of different size depending on the sample (violet and light-blue curves). In (d) the decay histograms for RUP2 are shown normalized so that the convergence to the same decaying slope is observed. The gray curve shows a measurement performed in a layer of the QDs emitting at 2350 meV spin-coated on glass.

contrast, sample RUP2 (Figure 4.22c) shows an observable decay rate enhancement for times $t < 20\,\text{ns}$. This modification is better visualized in Figure 4.22d, where we normalized the unbleached and the $40\,\mu\text{m}$ CPA measurement with the values at long times. However, this is also an unexpected result since, as discussed above, the emission of QDs in RUP2 is the less modified by the transition between the SPP and the polaritons among the three samples.

Here we have done a qualitative analysis of a selected group of data performed in samples RLP, RUP1, and RUP2. For sake of completeness regarding these experiments for which a lot of efforts and time were invested, we present in Appendix B a compilation of experiments in which we attempt to understand the dependence of the QDs decay rate with the environment, observing small modifications of the histograms and analyzing the different components of the exponential decay. In addition, we discuss the peculiar response of the layer of QDs embedded in PMMA to the variation of the electromagnetic environment. Since an enhancement of two orders of magnitude was previously observed for QDs coupled to SPPs in our group [27], we explored the factors that inhibit the QDs decay rate acceleration. We analyzed low-concentration samples, and we found out that by adding the PMMA that we used in the samples studied in this chapter or by increasing the QDs concentration, a slow component $\Gamma \sim 0.03\,\text{ns}^{-1}$ has a major contribution to the histogram. This slow component has prevented us to perform a conclusive interpretation of the fluorescence decay rate measurements in terms of change of Purcell factor due to the coupling of the QDs with SPP or strongly coupled polaritonic modes.

## 4.5 Conclusion

In this chapter, we studied samples in which different propagating modes coexist due to photobleaching of a homogeneous layer of J-aggregates. The large oscillator strength of this material makes it suitable for the observation of strong coupling between fluorescent emitters and SPPs. By depositing J-aggregates on top of a silver film, we fabricated several samples in which the observed reflectance displayed polaritonic modes with Rabi splittings larger than 150 meV. Afterward, we observed how an optical lithography annihilated the absorption transition of the dye, eliminating, in turn, the strong coupling. We deposited QDs to probe the electromagnetic envi-

ronment in circular photobleached areas of different diameters to observe the non-local influence of the hybridized polaritons in their vicinities. We fabricated samples with QDs emitting at three different central wavelengths to probe different spectral ranges of the polaritons.

We observed the spectrally resolved emission pattern of the different samples. We showed the progressive modification of the luminescence of the QDs, from their emission through an SPP mode in large areas of unbleached J-aggregates towards their weak coupling to hybrid polaritons in areas where the organic dye is active. For this, we measured the photoluminescence emission pattern in 13 different CPAs. We also noticed that the presence of the hybrid states modifies the overall spectrum of the QDs. In TM polarization, the origin of this modification is the appearance of a gap at the resonance between the J-aggregates and the SPP that suppresses propagating modes at this band. In contrast, the TE-polarized spectrum is probably modified due to the direct absorption of uncoupled J-aggregates.

In this rich system, where the physical properties are determined by an interplay of energy transfer and near-field coupling, we took different approaches to characterize the interaction between the fluorescent emitters. Besides the reciprocal space spectroscopy performed at the center of the CPAs, we analyze the fluorescence decay rate of the QDs positioned in different environments. The attempt to characterize the LDOS with this technique failed due to the unexpected insensibility of the QDs to the environment when they are embedded in media as PMMA or in a highly concentrated QDs layer. Finally, in the frame of a collaboration with the Plasmonics and Quantum Nanophotonics team of LCFIO, we use a model considering the thermal emission of excited emitters that properly reproduced our observations. As the number of emitted photons is linked to the number of excited J-aggregate molecules and QDs, they acquire a non-zero chemical potential, unlike a regular blackbody. We extract a difference of the chemical potential of radiation as the parameter that allows matching the relative intensity of the two active materials of the sample with the corresponding experimental data. This analysis is still in progress at the time we submit this manuscript.

# References


[1] E. Bailly, K. Chevrier, C. Perez, A. Gassenq, J.-M. Benoit, C. Symonds, J. Bellessa, Y. de Wilde, V. Krachmalnicoff, B. Vest, and J.-J. Greffet, *In preparation* (2021). 67

[2] A. Herz, *Advances in Colloid and Interface Science* **8**, 237–298 (1977). 68, 69

[3] J. L. Bricks, Y. L. Slominskii, I. D. Panas, and A. P. Demchenko, *Methods and applications in fluorescence* **6**, 012001 (2017). 68, 70

[4] A. Mishra, R. K. Behera, P. K. Behera, B. K. Mishra, and G. B. Behera, *Chemical reviews* **100**, 1973–2012 (2000). 68

[5] S. Valleau, S. K. Saikin, M.-H. Yung, and A. A. Guzik, *The journal of chemical physics* **137**, 034109 (2012). 68, 70

[6] T. Kobayashi, *J-aggregates*, volume 2, World Scientific (2012). 68

[7] H. von Berlepsch, C. Böttcher, and L. Dähne, *The Journal of Physical Chemistry B* **104**, 8792–8799 (2000). 69

[8] D. M. Coles, A. J. Meijer, W. C. Tsoi, M. D. Charlton, J.-S. Kim, and D. G. Lidzey, *The journal of physical chemistry A* **114**, 11920–11927 (2010). 69

[9] H. Zollinger, *Color chemistry: syntheses, properties, and applications of organic dyes and pigments*, John Wiley & Sons (2003). 70

[10] L. Novotny and B. Hecht, *Principles of Nano-Optics*, Cambridge University Press (2006). 71, 72

[11] H. Yu, J. Li, R. A. Loomis, P. C. Gibbons, L.-W. Wang, and W. E. Buhro, *Journal of the American Chemical Society* **125**, 16168–16169 (2003). 71

[12] A. Brumberg, S. M. Harvey, J. P. Philbin, B. T. Diroll, B. Lee, S. A. Crooker, M. R. Wasielewski, E. Rabani, and R. D. Schaller, *ACS nano* **13**, 8589–8596 (2019). 71

[13] C. de Mello Donegá, *Chemical Society Reviews* **40**, 1512–1546 (2011). 71, 72

[14] T. M. Inerbaev, A. E. Masunov, S. I. Khondaker, A. Dobrinescu, A.-V. Plamadă, and Y. Kawazoe, *The Journal of chemical physics* **131**, 044106 (2009). 71

[15] K. Chevrier, *Cohérence dans les systèmes métal/organique en couplage fort états étendus et métasurfaces*, Ph.D. thesis, Université Claude Bernard - Lyon I (2019). 75, 76, 80

[16] C. Bonnand, *Couplage fort entre plasmons de surface et excitons de semiconducteur organique*, Ph.D. thesis, Université Claude Bernard - Lyon I (2006). 76

[17] S. A. Guebrou, C. Symonds, E. Homeyer, J. Plenet, Y. N. Gartstein, V. M. Agranovich, and J. Bellessa, *Physical review letters* **108**, 066401 (2012). 78

[18] K. Chevrier, J.-M. Benoit, C. Symonds, S. Saikin, J. Yuen-Zhou, and J. Bellessa, *Physical review letters* **122**, 173902 (2019). 78, 79

[19] A. P. Demchenko **8**, 022001 (2020). 79

[20] V. M. Agranovich, M. Litinskaia, and D. G. Lidzey, *Physical Review B* **67**, 085311 (2003). 85

[21] M. Litinskaya, P. Reineker, and V. Agranovich, *Journal of luminescence* **119**, 277–282 (2006). 86

[22] D. M. Coles, P. Michetti, C. Clark, W. C. Tsoi, A. M. Adawi, J.-S. Kim, and D. G. Lidzey, *Advanced Functional Materials* **21**, 3691–3696 (2011). 86

[23] T. Virgili, D. Coles, A. Adawi, C. Clark, P. Michetti, S. Rajendran, D. Brida, D. Polli, G. Cerullo, and D. Lidzey, *Physical Review B* **83**, 245309 (2011). 86

[24] X. Zhong, T. Chervy, L. Zhang, A. Thomas, J. George, C. Genet, J. A. Hutchison, and T. W. Ebbesen, *Angewandte Chemie International Edition* **56**, 9034–9038 (2017). 86

[25] J.-J. Greffet, P. Bouchon, G. Brucoli, and F. Marquier, *Physical Review X* **8**, 021008 (2018). 97, 98

[26] P. Wurfel, *Journal of Physics C: Solid State Physics* **15**, 3967 (1982). 98

[27] D. Bouchet, E. Lhuillier, S. Ithurria, A. Gulinatti, I. Rech, R. Carminati, Y. De Wilde, and V. Krachmalnicoff, *Physical Review A* **95**, 033828 (2017). 103

# Chapter 5

# Hybridization between two dyes strongly coupled to a plasmon

## Contents

In this chapter, we present the study of the hybridization between an SPP and two spatially separated species of fluorescent emitters. They consist of J-aggregated dyes that can enter independently in strong coupling with the SPP. The first one is TDBC, already introduced in Chapter 4, and the second is another cyanine dye with absorption and emission bands red-shifted with respect to the TDBC emission spectrum. The work presented here takes place in the frame of a collaboration between the team Matériaux et Nanostructures Photoniques, led by Joel Bellessa at ILM Lyon, and our team at Institut Langevin. Sample fabrication and wide-field optical characterization were performed at ILM Lyon, while complementary studies with focused excitation and local detection were performed at Institut Langevin during my Ph.D. We acknowledge Sylvain Minot, Antoine Bard, Alban Gassenq, Jean-Michel Benoit, and François Bessueille for the development and the optimization of the sample fabrication process, which will be described in section 5.1. We acknowledge Antoine Bard, Clémentine Symonds, and Joel Bellessa for the optical characterization of the samples in wide-field, which allowed us to prove mode hybridization in the sample. Wide-field studies will be described in sections 5.2 and 5.3. The optical characterization performed at Institut Langevin, which consisted in observing the system's behavior under a tightly focused excitation and probing the luminescent response locally, are discussed in section 5.3. A publication summarizing all these results is under preparation.

The chapter is divided into three parts. First, we describe the periodic structuration of the two dyes that compose the active optical layer of the sample. Each dye is patterned with a corresponding polymer stamp, and the two materials are deposited on a silver film with a soft lithography technique. We explain the deposition process and show how an overall structure with a Moiré pattern is produced by tilting the two arrays by a few degrees. We focus our attention on zones where the dyes are spatially separated. Second, we show the hybridization of the silver SPP with the emitters through wide-field reflectometry measurements. We observe the formation of three polaritonic branches in the energy dispersion as a function of the in-plane wavevector. We examine the coupled oscillators' Hamiltonian for the light-matter coupling between three elements, considering the resonance of both dyes and the SPP. By fitting the experimental values of the hybrid modes, we obtain the respective coupling energies between the plasmon with each emitter. We calculate the Hopfield coeffi-

cients to illustrate the hybridization between excitons and plasmons in this structure.

Third, we report on the polariton-assisted energy transfer observed through photoluminescent measurements. First, we discussed the distribution of the system emission under wide-field illumination, which is channeled through the polariton with the lowest energy. Afterward, we present the spatial imaging of the sample's fluorescence when the sample is excited with a tightly focused spot. We also analyze the spatial-spectral distribution of the fluorescence, measuring the sample's emission for two different sample orientations. Finally, we show a similar experiment with a detection far away from the excitation position and discuss the effect of the modes hybridization in our observations.

## 5.1 Sample Fabrication

The samples that we investigate in this chapter consist of periodic arrays of two J-aggregates deposited on a thin silver film of 50 nm. The properties of the glass substrate, as the process of the silver evaporation, are the same as described in Chapter 4. The first dye is J-aggregated TDBC (S0046, Few Chemicals). The second is the J-aggregated cyanine dye 5-Chloro-2-[2-[5-chloro-3-(4-sulfobutyl)-3H-benzothiazol-2-ylidenemethyl]-but-1-enyl]-3-(4-sulfobutyl)-benzothiazol-3-ium hydroxide, inner salt, triethylammonium salt, referred to as S2278 (S2278, Few Chemicals), whose monomer chemical structure is shown in Figure 5.1a. Figure 5.1b shows the spectral relation between both dyes, in which we observe that the absorption and emission maxima of J-aggregated S2278 are 610 and 625 nm, respectively. We notice that the emission maxima of the dyes are separated by ~ 39 nm (127 meV) and that the S2278 absorption spectrum has a non-negligible overlap with the emission of the TDBC.

The objective of the sample design is to create zones in which the two species of fluorescent dyes are spatially separated. For this purpose, two different thin films structured in periodic squared arrays are superimposed. Figure 5.2a shows the structuration of the TDBC layer, which consists of a homogeneous layer with a 2D hole array of diameter $\varnothing_h = 4.25\,\mu$m. The S2278 has a complementary shape consisting on disks of diameter $\varnothing_d = 3.75\,\mu$m, as shown in figure 5.2b. Both arrays have a spatial period of $5\,\mu$m.

Now, we summarize the deposition method of the structured dye layers, basing

(a) (b)

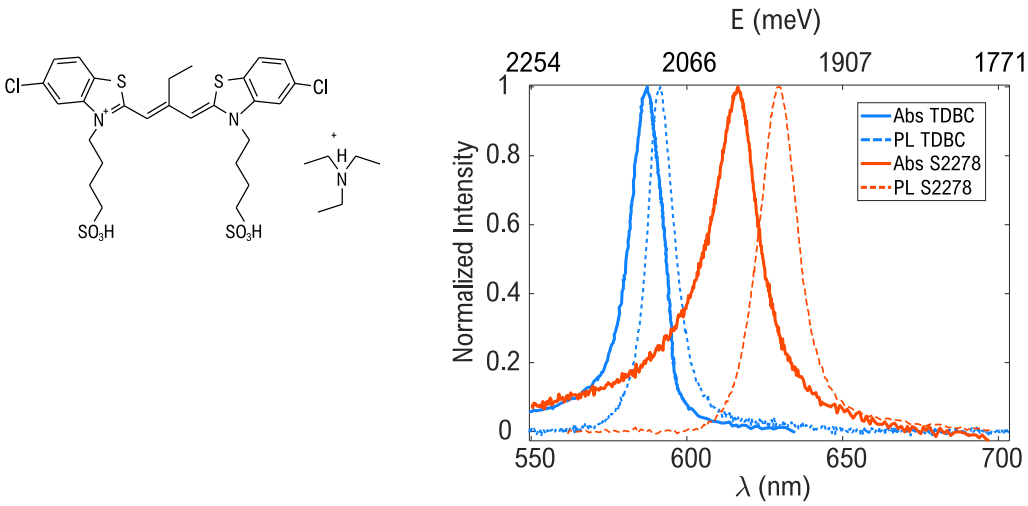


Figure 5.1 – (a) Chemical structure of the S2278 monomer. (b) Absorbance and emission spectra of the J-aggregated dyes TDBC (blue solid and dashed curves) and S2278 (red solid and dashed curves) composing the sample. The FWHM of the absorption (centered at 616.1 nm) and the emission (centered at 630.0 nm) of the S2278 is 19.8 nm and 14.6 nm, respectively. The emission spectra were taken independently for each dye spin-coated on glass, with a 532 nm laser excitation.

(a) (b)

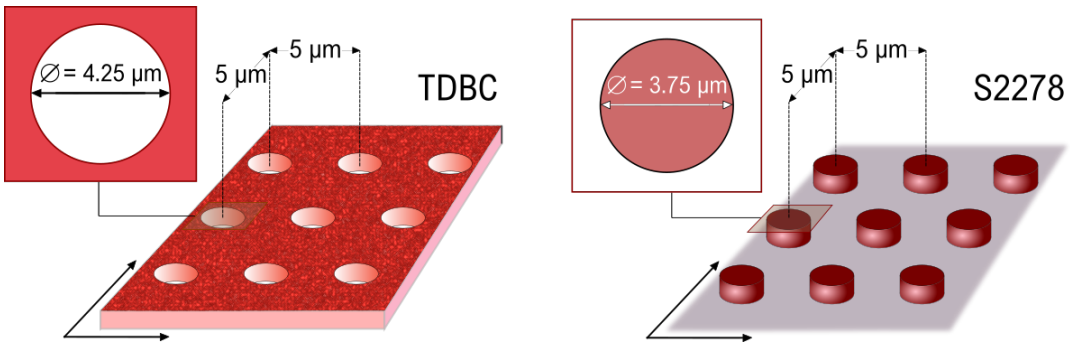


Figure 5.2 – Structure of the layers containing the two different dyes as the active optical media. In a), the pattern consists of a homogeneous layer of TDBC (dye-1) with a square periodic array of circular holes of diameter $\varnothing = 4.25\,\mu$m. In b), the pattern consists of a square periodic array of S2278 (dye-2) disks of diameter $\varnothing = 3.75\,\mu$m. The difference between diameters avoids the direct contact between the fluorescent materials. The spatial period for both arrays is $5\,\mu$m.

the description on the work performed by Li et al. [1] at ILM for an array of holes in a TDBC layer. This deposition technique exploits the dissimilar mechanical adhesion and electrostatic interactions at different interfaces. It consists of a layer-by-layer assembly of polyelectrolyte multilayer (PEMs), alternating oppositely charged species: anionic aggregated cyanine dyes and cationic PDAC, on molding stamps for later transfer to the silver-coated substrates. This method is called microcontact printing ($\mu$CP) and provides a versatile approach for patterning surfaces at the micrometer scale with a soft lithography technique. The soft-printing process is detailed in Ref. [2].

The first step of the deposition process consists of fabricating the stamps with the negative of the arrays of Figures 5.2a and 5.2b. An elastic polymer, poly(dimethylsiloxane) (PDMS), which has a low interfacial free energy and is chemically inert, was deposited onto a master molded by photolithography. Then, the PDMS was peeled off and used as a substrate for depositing the PEMs. The second step consists of coating the PDMS stamps with the PEMs. Since the process is similar for both structured dyes, we explain only the fabrication of the layer containing the TDBC.

Independent chemical baths were used to deposit multiple layers onto the stamps, alternating PDAC and TDBC to produce a strong adhesion between cationic and anionic species ensuring the sample stability. The PDMS stamps were first immersed in PDAC aqueous solution and then rinsed with deionized water to remove all material excess leaving a monolayer of PDAC. The stamps were then immersed into a TDBC solution followed by three additional rinses to remove the excess of dye, each washing being followed by drying under an argon stream. The process was repeated to assemble twelve bilayers of (PDAC/TDBC) and eight bilayers of (PDAC/S2278) in their corresponding stamps. The number of bilayers for each array is chosen so that at the end of the sample fabrication both dyes have the same thickness.

The last step of $\mu$CP is to transfer the PEMS to the silver-coated substrate. For this, a PDAC layer is first deposited on top of the silver film, so there is an electronic affinity with the PEMs' outer dye layer. Then, the coated PDMS is placed on top of the silver, as depicted in Figure 5.3. The transfer mechanism is based on the difference between the PDMS/PEMs and silver/PDAC interfaces' adhesion strengths. The adhesion strength between the multilayer and the stamp must be lower than the adhesion strength between the structured multilayer and the deposition surface. Because

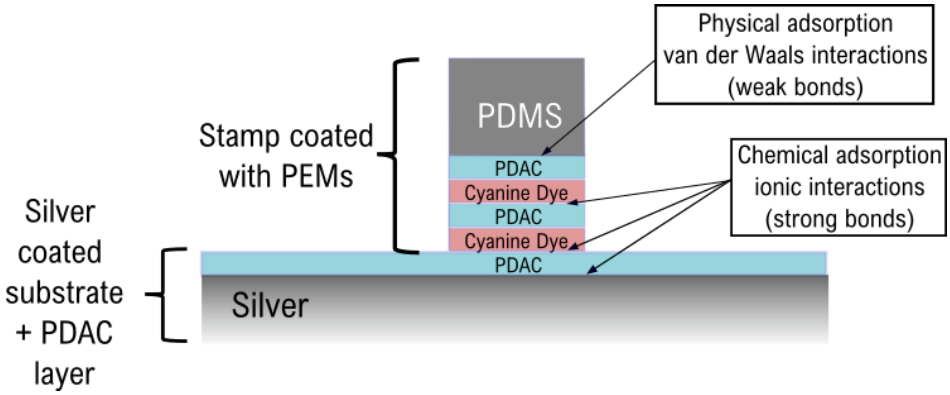


Figure 5.3 – Schematic representation of the different interactions during the stamping process. The coated PDMS is placed on top of a thin film of silver, covered by a layer of PDAC. Weak van der Waals interactions mediate the interaction between the stamp and the PEMs compared to the strong ionic bonds between the layers with alternated polarity. Since there is an ionic attraction between the outer layer of the PDMS stamp and the PDAC layer deposited on the silver, the stamp can be removed, leaving the structured PEMs on the sample. Image reproduced from [1].

of the low surface free energy of the PDMS mold, the adhesion between the PDMS surface and the multilayered film is poor. In contrast, the outer layer of the PEMs has strong chemical adhesion to the capped PDAC layer on silver. Therefore, placing the multilayer-coated stamp onto it led to adhesion between the two surfaces almost without the need to apply external pressure or heating treatment. After several hours of contact, careful removal of the PDMS stamp results in the localized transfer of the structured multilayers on the silver-coated substrate.

The $\mu$CP process was first performed for the TDBC holes array and afterward for the S2278 disk array. AFM measurements reported in Figure 5.4, demonstrate the successful deposition in an area in which both motifs perfectly overlap. In the work of Li et al., the thickness for a PDAC/TDBC bilayer was estimated to a value of $\sim 1.25$ nm. In the samples described in this section, the average thickness of the 12 deposited bilayers should be 16 nm. The regions displayed in Figure 5.4 show a good agreement with this value. However, the $\mu$CP of the second array can tear off the material of the surface, decreasing the effective thickness on some areas of the sample. Also, as the AFM images show, the S2278 disks have the same height showing that both structured layers have approximately the same thickness. Importantly, the displayed zones show a spatial separation between the two dyes with negligible contact be-

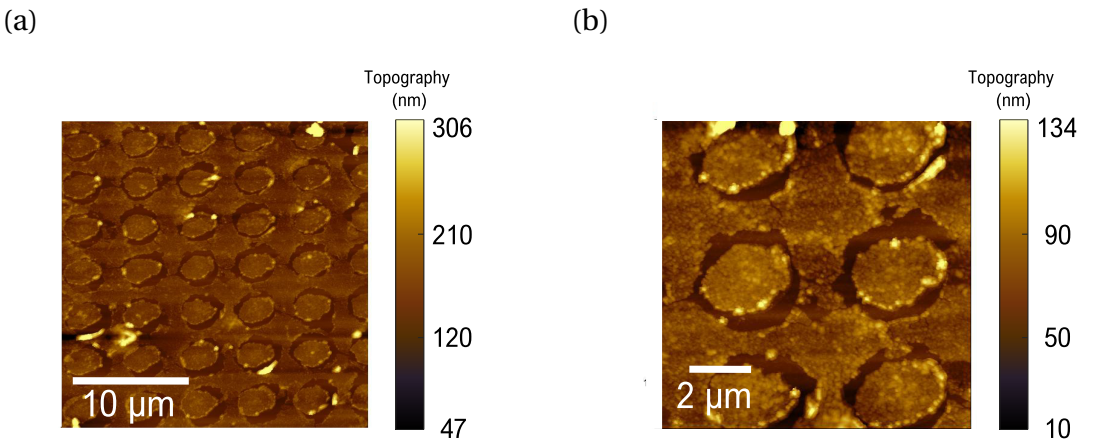


Figure 5.4 – AFM measurements with different magnification show the successful deposition of structured TDBC and S2278, with a layer thickness of ~ 16 nm for both cases. We observe that the spatial overlap between the dyes corresponding to the two motifs is negligible. Moreover, there are empty spaces in the crown comprehended between the disks of S2278 and the TDBC. Images realized at ILM by Antoine Bard.

tween their borders. Furthermore, the immediate surroundings of the disks are not covered by any material, meaning that there is a discontinuity of the dielectric layer. The implications in the propagation of modes are discussed in the following sections.

Due to the difficulty of perfectly matching one periodic motif with its complement so that all disks and holes are concentric in the sample, a slight tilt of a few degrees (~ 2°) is set between them. It is performed by tilting the stamp in the $\mu$CP process of the S2278 over the already deposited TDBC. In this way, a Moiré pattern with a larger scale appears, as represented in Figure 5.5a, where we have exaggerated the tilt angle for a better visibility of the periodicity of the Moiré pattern. In this sketch, we can identify zones in which the disks fall between two holes, and zones where the disks fit into the holes over a determined area. As mentioned before, we will focus on the latter, where the two dyes are spatially separated. Figure 5.5b shows a zone of interest illuminated with a 532 nm wide-field laser excitation. An example of a region where the arrays have a mismatch of half of the lattice parameter in both directions is shown in Figure 5.5c. In such regions, the disks of S2278 are entirely overlapped with the area covered by TDBC. Notably, there is a large number of the zones of interest among the sample since the lattice parameter of the stamps is 5 $\mu m$,

while the total area of the PDMS stamp is of the order of the cm. In the rest of the chapter, we will refer to the TDBC, as *dye-1* and to the S2278 as *dye-2*.

(a)

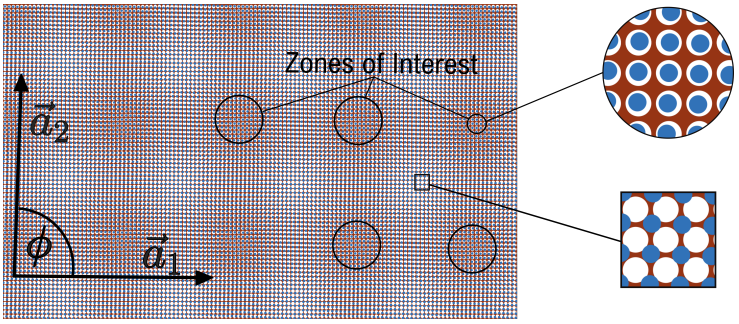


(b) (c)

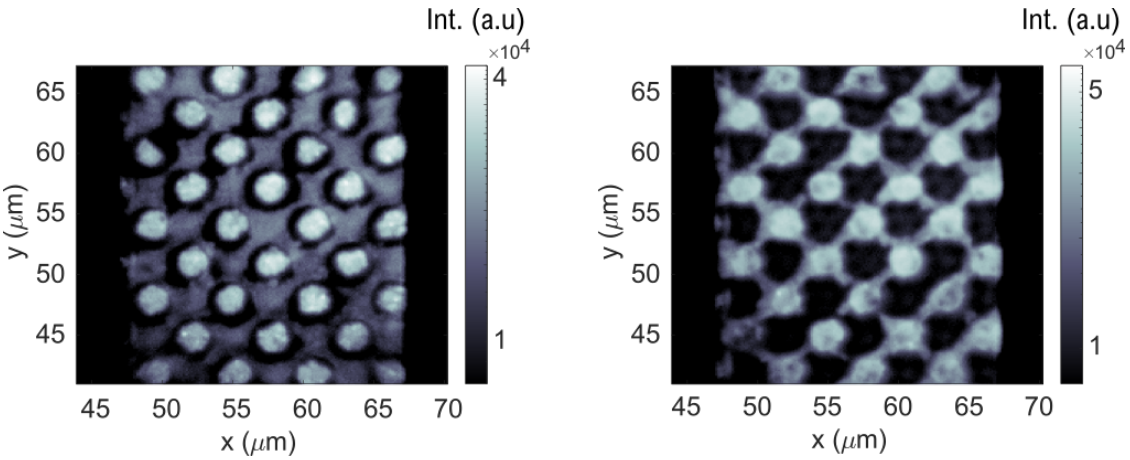


Figure 5.5 – a) Drawing illustrating of the Moiré pattern in the sample. The angle $\phi$ between the lattice vectors of the square arrays $a_i$ is slightly smaller than 90° (not on scale). Fluorescence images were taken with an EM-CCD of regions of the sample illuminated with a 532 nm wide-field laser excitation for regions in which the two individual patterns b) spatially match and are the areas that we studied, and c) have a mismatch in both directions.

## 5.2 Strong coupling with SPPs and two emitters

In the previous chapter, we observed that the strong coupling between an SPP and a fluorescent emitter modifies the electromagnetic environment, producing polari-

tonic modes. This chapter presents the coupling between the two J-aggregates of the sample described above and the surface plasmon propagating at the metal/dielectric interface. These molecules can enter in a strong coupling regime of interaction with the SPP independently. By depositing them on the top of the same silver film, in regions separated at distances smaller than the SPP propagation length, we aim to observe their simultaneous hybridization with the SPP. Figure 5.6 shows the elements that interact in this system, showing the Transfer-Matrix Method (TMM) calculation for the reflectivity of an SPP and the dispersionless excitonic lines for dye-1 at $E_1 = 2101.4\,\text{meV}$ and for dye-2 at $E_2 = 1968.0\,\text{meV}$.

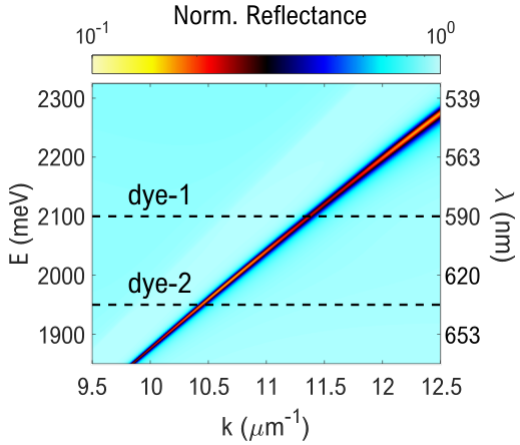


Figure 5.6 – The colormap shows the TMM reflectance calculation for an SPP mode created at the interface between a 50 nm silver layer and an inactive optical layer with a thickness of 12 nm. The constant refractive index of this layer is an average of the PDAC and the J-aggregates background index $n_b$. The dashed lines represent the excitonic transition at 2101.4 meV for dye-1 and at 1968.0 meV for dye-2.

We are interested in the observation of the hybridization of strongly coupled modes for two excitonic resonances. We recall that the J-aggregated dyes of this system can produce large Rabi splittings $\sim 200\,\text{meV}$ when coupled to an SPP, at room temperature. The energy separation of the emission spectra of the dyes $E_1 - E_2$ has a value of 133.4 meV, and we expect hybridization in the energy range comprehended between their respective excitonic resonances. To probe the optical properties of the structure, we measured their white light reflectivity spectrum with a wide-field illumination with a diameter of $\varnothing = 50\,\mu\text{m}$ (with a similar setup to the one showed in Chapter 3). Figure 5.7a shows the reflectivity dispersion with the modes of the sam-

ple. We observe the existence of two anticrossings at the exciton resonances that produce three polaritonic branches, as expected for a strongly coupled system between a photonic mode and two emitters. We classify these branches by their energy range, namely, the lower polariton (LP) branch ($E < 1968.0\,\text{meV}$), the middle polariton (MP) branch ($1968.0\,\text{meV} < E < 2101.4\,\text{meV}$) and the upper polariton (UP) branch ($E > 2101.4\,\text{meV}$). The center of the reflectivity dips for several energies is marked with black dots. The SNR is low due to the presence of several interfaces dye/air and dye-1/dye-2 that produce scattering of light, broadening the propagating modes. Moreover, as we will see later, the diffraction of light due to the periodic structuration is observable in luminescence for larger wavevectors in reciprocal space, reducing the contrast of the coupled modes for high $k$ values.

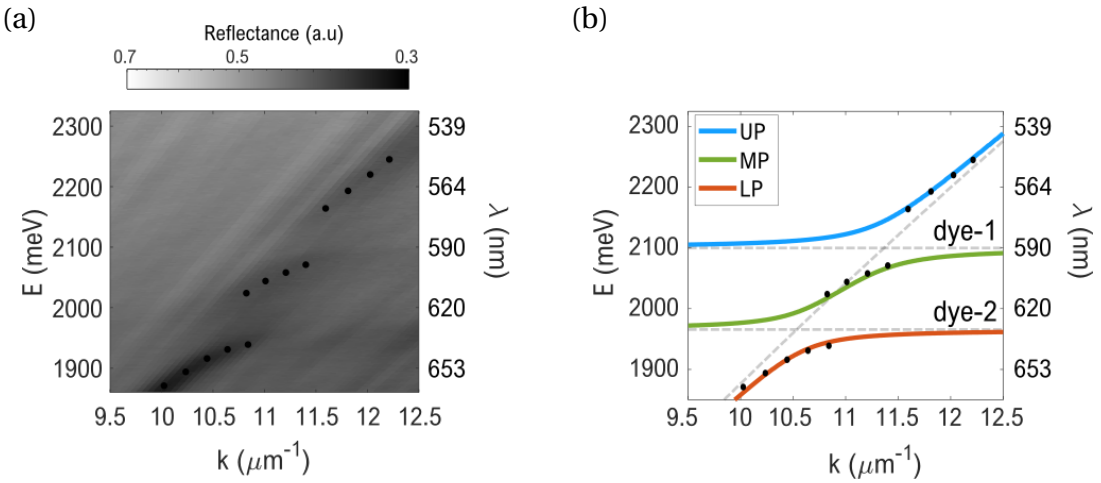


Figure 5.7 – a) Reflectance of the sample using wide-field illumination ($\varnothing = 50\,\mu\text{m}$). The image shows two anticrossings at the resonances of the J-aggregates, which creates three polaritonic branches: the upper polariton (UP), the middle polariton (MP), and the lower polariton (LP). Dips minima are indicated with black dots. To improve the visualization of the modes, we plotted the image with a logarithmic distribution of the colormap. Measurement performed by A. Bard at ILM. b) Polaritonic branches fitted with a coupled oscillators model. The model shows an excellent agreement with the experimental data for values of the light-matter coupling of $\hbar\Omega_1 = 97\,\text{meV}$, and $\hbar\Omega_2 = 104\,\text{meV}$.

In the following, we describe the observed behavior quantitatively using a model based on the interaction of three independent states. Chapter 2 described how the interaction between the electric field and a dipole could be understood by two coupled oscillators with a given coupling strength. In this chapter, we extend this model to

three-coupled oscillators describing the interaction between the SPP, with wavevector-dependent energy $E_{spp}(k)$ and the two dyes centered respectively at $E_1$ and $E_2$. The matrix equation for solving such Hamiltonian is:

$$(\hat{H} - E\hat{I})\,\vec{\alpha} = \begin{pmatrix} E_{spp}(k) - E & \hbar\Omega_1 & \hbar\Omega_2 \\ \hbar\Omega_1 & E_1 - E & 0 \\ \hbar\Omega_2 & 0 & E_2 - E \end{pmatrix} \begin{pmatrix} \alpha_{spp} \\ \alpha_1 \\ \alpha_2 \end{pmatrix} = 0 \tag{5.1}$$

where $\hbar\Omega_i$ is the energy interaction of the dye $i$ with the SPP. There are three unique solutions for $E$, and thus the polariton energy dispersion comprises three wavevector-dependent branches corresponding to the UP, MP, and LP branches. These solutions have corresponding eigenvectors $\vec{\alpha}$, which are written on the basis of the normal modes of the uncoupled resonances for the SPP and the dyes, with respective coefficients $\alpha_{spp}$, $\alpha_1$, and $\alpha_2$. In this model, the two emitters don't interact with each other unless via the plasmon, an hypothesis which is justified since the different species of emitters are spatially separated in the sample.

To solve equation 5.1, we use the minima of the TMM reflectivity for $E_{spp}(k)$ shown in Figure 5.6. The three numerical solutions of equation 5.1 are plotted on Figure 5.7b, which shows an excellent agreement with the experimental reflectivity data. The fitted values for the Rabi splitting for the dye-1 with the plasmon is $\hbar\Omega_1 = 97\,\text{meV}$. This result is consistent with the volume fraction of dye-1 in the unit cell of the sample, which corresponds to 56%. As an order of magnitude estimation, we compare this value to an extended layer of dye-1 with the same thickness and concentration deposited on silver, fabricated and studied at ILM having a Rabi splitting around 165 meV [3; 4]. The Rabi splitting for the coupling between dye-2 and the SPP is $\hbar\Omega_2 = 104\,\text{meV}$. Since both Rabi splittings were left as free parameters, these values should not be understood as a quantitative characterization but as tools to understand the hybridization of the sample modes. The coupled oscillator model's additional interest is that we can calculate the Hopfield coefficients [5], which characterize the hybridization of the modes as a function of the uncoupled states. Their square corresponds to the mixing coefficients $|\alpha_{spp}|^2$, $|\alpha_1|^2$, and $|\alpha_2|^2$ which describe the relative plasmonic and excitonic weights of the polaritons [6]. The mixing factors are numerically calculated for the three polaritonic states in Figure 5.8. Moreover,

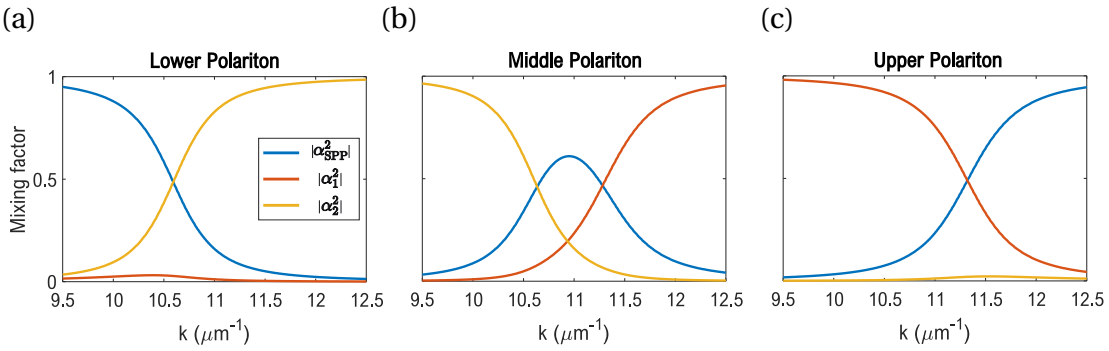


Figure 5.8 – Mixing factor or Hopfield coefficients for $|\alpha^2_{\mathrm{SPP}}|$ (blue), $|\alpha^2_1|$ (red), and $|\alpha^2_2|$ (yellow) for the a) LP b) MP and c) UP branches as a function of the in-plane wavevector. These values have been calculated from the determinant problem of the coupled oscillator model. The graphs show the mixed characters of the polaritonic branches. We observe that, for the UP and the LP, the mixing is maximized at the anticrossings corresponding to the wavevectors of $k = 11.35\,\mu\mathrm{m}^{-1}$ for the SPP with the exciton of dye-1, and $k = 10.61\,\mu\mathrm{m}^{-1}$ for the SPP with the exciton of dye-2. In the MP, the mixing is maximized at $k = 10.90\,\mu\mathrm{m}^{-1}$ with a high plasmonic character and a significant weight for both excitons. The constraint that $|\alpha_{\mathrm{spp}}|^2 + |\alpha_1|^2 + |\alpha_2|^2 = 1$ is verified for the three graphs.

the relative absorption of each polariton branches approximately follows their SPP fraction $|\alpha_{\mathrm{spp}}|^2$ [7]. In this manner, we observe that the plasmonic component of the LP branch reflectivity has a significant weight from 9.5 to 11 $\mu\mathrm{m}^{-1}$ of the dispersion curve and decreases as it approaches the exciton line of dye-2. At small wavevectors, only the lower branch has a significant plasmon character. The upper polariton is dominated by the plasmonic component between 11.5 and 12.5 $\mu\mathrm{m}^{-1}$. At 11.5 $\mu\mathrm{m}^{-1}$ the UP branch possesses a significant plasmon character and becomes detectable. It can be seen that the composition of the LP and UP branches mainly contains contributions from the surface plasmon and only one of the two excitons. Finally, in the experimental data shown in 5.7a, the MP is detected between 10.8 and 11.5 $\mu\mathrm{m}^{-1}$. The MP is dominated by the dye-2 exciton at small wavevectors and by the dye-1 exciton at high wavevectors. In an intermediate range the hybridization occurs between the SPP and the two excitons. The result is that at 10.9 $\mu\mathrm{m}^{-1}$, the SPP contribution is twice larger than $|\alpha_1|^2 = |\alpha_2|^2$. By comparing the experimental reflectivity dispersion shown in Fig. 5.7a, and the mixing factors, we verify that the UP, LP and MP are detected mainly when the plasmonic component is predominant.

## 5.3 Polariton-assisted energy transfer between spatially separated emitters

In the previous section, we observed that the sample behaves as a strongly coupled system with three hybrid modes propagating within it. In this section, we study the system's photoluminescence (PL) through wide-field and focused laser excitations and observe the distribution of the emission spectrally and spatially. We start by discussing the $E(k)$ emission pattern of the sample under wide-field excitation, in which we observe the emission directed mainly through the lower polariton branch. Also, we see the effect of the diffraction produced by the periodic structuration of the sample in real space. For the localized excitation, we excite the system in two possible configurations changing the relative angle of the array with respect to the spectrometer slit. Afterward, we show the PL of the sample under a focused laser excitation addressing only dye-1. We study the propagation of the hybrid modes by observing the fluorescence extended along the sample. We also show the wavelengths of the extended fluorescence by spatial-spectral measurements. The corresponding PL emission pattern shows broad modes in which the usual polariton-like aspect of the modes near the anticrossing is hard to resolve. However, as it will be shown below, we continue to observe more light emitted at the energy of dye-2 than what we would have expected for emitters without the plasmonic resonance, e.g., on a glass substrate.

### 5.3.1 Photoluminescence spectra in wide-field excitation

Figure 5.9 shows the spectral distribution of the PL emission in the absence of the plasmon. These data were obtained on a region of the sample in which the silver layer was not deposited, but the structuration of the arrays is identical to the one shown in Figure 5.5b. This spectrum shows that the intensity ratio between the emission peaks of the two dyes is close to unity, and it is taken as a reference to determine energy transfer processes when dye-1, dye-2 and the SPP interact on the silver film.

Figure 5.10 shows the luminescence of the structured layers on silver, under a wide-field excitation beam with a 50 $\mu$m diameter. In Figure 5.10a, we see the PL dispersion with most of the emission channeled through the lower polariton ($E <$

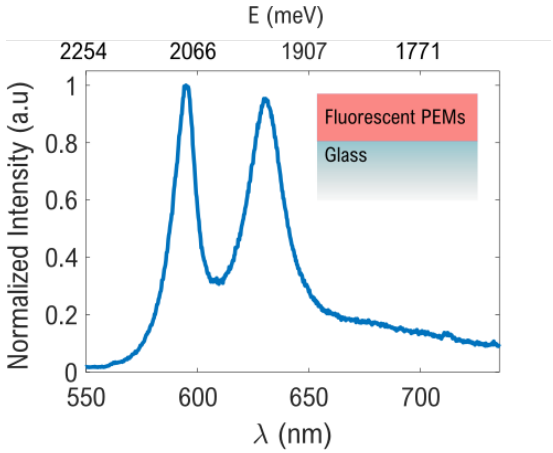


Figure 5.9 – Photoluminescence spectra of dye-1 and dye-2 on glass. Regions containing dye-1 and dye-2 are patterned following the same scheme as the one described in the previous section. The used deposition process is the same as for the one described in the previous section, but without the silver layer. The illumination consists of a wide-field laser excitation beam with a diameter of $\varnothing = 50\,\mu$m. The normalized spectrum shows the dyes' emission with maximal values that have almost the same intensity despite the different number of layers of dye-1 and dye-2 deposited on the substrate. Also, we notice a long tail for wavelengths larger than 650 nm.

1968.0meV) of the whole hybrid system. We also observe the weak emission of uncoupled emitters of dye-1 and almost no light coming from energies in the middle polariton range. Figure 5.10b shows the integrated spectrum of the sample's luminescence, in which the ratio between the peak maxima of dye-1 and the emission around dye-2 is 0.136. We recall that the LP is a state hybridized mainly between the SPP and the exciton of dye-2. By comparing the spectrum of Figure 5.10b with the PL reference on glass of Figure 5.9, we conclude that propagating modes, which in this system are hybrid exciton/SPP polaritons, favor the energy transfer between the two dyes. As we observed in section 1, we ensured that the only coupling between the two exciton species is that mediated by the propagating modes of the system since the dyes are separated by distances > 100 nm, which precludes short-range dipole-dipole interactions that are characterized by Forster transfer radii of typically less than 10 nm [7].

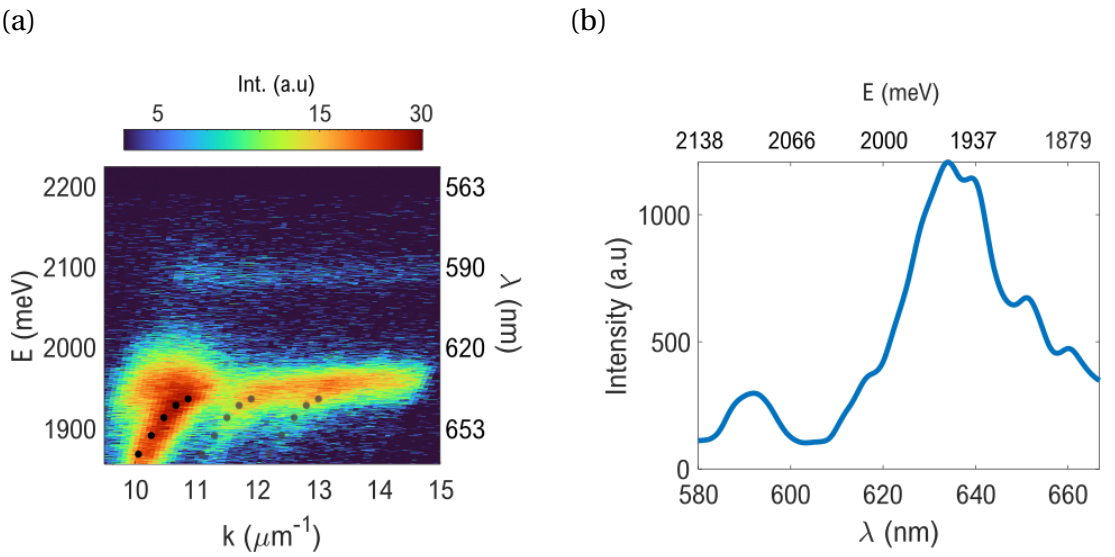


Figure 5.10 – a) Photoluminescence in TM polarization of the Moire sample under a 532 nm wide-field laser excitation. The emission around the energy of the uncoupled dye-1, which is around 2100 meV is weak and corresponds to the incoherent emission of uncoupled emitters. The largest contribution of the PL comes from the lower polariton of the system. The intensity colormap is on a logarithmic scale. The black dots correspond to the positions obtained in the reflectometry measurement.The shaded gray dots correspond to the same $(E,k)$ coordinates displaced by $\sim 1\,\mu\text{m}^{-1}$. This shift approximately matches the reciprocal periodicity of the array $b = 2\pi/a = 0.89\,\mu\text{m}^{-1}$ where $a = 7.07\,\mu$m is the spatial period of the array in the propagation direction of the detected modes. This shows that the rebounds are diffracted modes of the periodic array of the sample. b) Integrated spectrum from the $E$ vs. $k$ measurement in a). The low SNR is due to the low excitation in wide-field to protect against photobleaching the zones in which the deposition of the stamp was homogeneous and free of defects. Measurement performed by A. Bard at ILM.

The other notable feature of the PL dispersion shown in Figure 5.10a is the existence of diffracted rebounds observed at wavevectors larger than the wavevector of the LP, with the same bent shape of this mode. For example, looking at the energy cross-section, $E = 1900$ meV, the wavevector of the LP is 10.2 $\mu\text{m}^{-1}$, and it is followed by two rebounds that have a wavevector of 11.4 and 12.3 $\mu\text{m}^{-1}$. These rebounds are a product of the diffraction by the periodic structuration of the sample. Their difference in $k$, that we will call $\Delta k$ in the following, is related to the spatial period of the lattice formed by the sequence of dye-1 and dye-2 regions in such a way that $\Delta k = 2\pi/a$. The PL emission pattern showed in Figure 5.10a was measured in the 45° configuration depicted in Figure 5.11c, in which the detected propagating modes are

subject to a spatial period $a = 7.07\,\mu$m that corresponds to a period in the reciprocal space of 0.89 $\mu$m$^{-1}$. This agrees with the reciprocal period, which is experimentally observed.

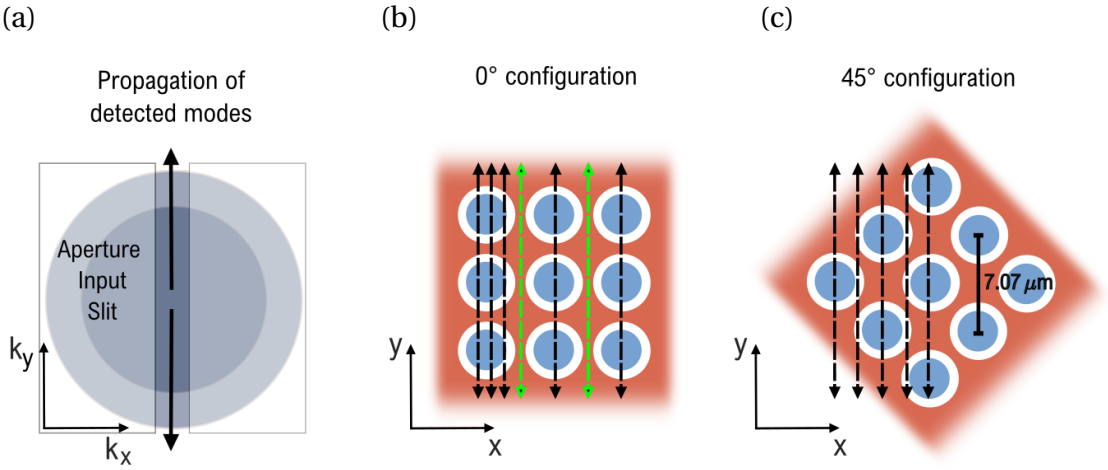


Figure 5.11 – a) Sketch of the back focal plane (grey disk) imaged on the spectrometer's slit. The dark grey disk is the signal collected below the objective's critical angle, and the light grey disk is the supercritical collected signal. The spectrometer slit, which is represented by the region between the two shaded rectangular areas, is optically conjugated with the BFP of the microscope objective, allowing to perform a selection in Fourier space. When the slit is almost closed, it leaves a narrow opening along the $k_y$ axis of the BFP, favoring the detection of propagating modes in this direction. b) Patterning of dye-1 (in red) and dye-2 (in blue) on the silver film. We will refer to this configuration as '0°', as opposed to the configuration sketched in c), in which the pattern is rotated by 45° and which is called '45°' in the text. In the 0° configuration, the plasmon that propagates along the spectrometer's slit axis can interact with the two dyes in different ways. The plasmon propagating along the black dashed lines goes through the interfaces air/dye and dye-1/ dye-2, while the plasmon propagating along the green arrow propagates without obstacles along with the continuous dye path. c) The plasmons propagating along with the direction of the slit in the second configuration, named 45°, have similar paths albeit not completely equivalent.

### 5.3.2 Photoluminescence spectra under focused excitation

In the previous subsection, we observed the luminescence of the sample under a wide-field excitation where the resulting collection is a spatial average of the sample's emission. In this section, we study the PL local response of the sample under a tightly focused excitation. In such a manner, we examine hybrid modes propagation,

and therefore the extension of the energy transfer from dye-1 towards dye-2. Moreover, we explore the two different orientations shown in Figure 5.11. Figure 5.11a illustrates the angular selection for the detection of propagating modes by closing the spectrometer slit, as described in Chapter 3. Figure 5.11b sketches a configuration in which the sample is placed so that the shortest lattice vector is parallel to the slit. In this case, named the 0° configuration, there are two possible kinds of paths through which the detected modes can propagate in real space when the excitation laser is focused at a given spot of the sample: one path, indicated by the dashed black arrows in Figure 5.11b, is such that the detected modes originate from directions on the sample periodically modulated by the circular patterns; the other path, indicated by dashed green arrows, is such that the detected modes originate from directions on the sample passing between the columns of circular patterns, where no periodic modulation is felt. Figure 5.11c shows that, by rotating the sample 45°, all the detected modes arise from directions on the sample in which the same spatial modulation is present.

First, we consider the case with the 45° configuration, as shown in Figure 5.12 in which all the images were acquired using a 532 nm laser excitation. We started by finding a region with a good deposition quality of the dye layer. Figure 5.12a and 5.12b show the fluorescence of the sample under a large wide-field illumination, in regions where homogeneity and continuity are observed in a diameter of $\sim 10\,\mu$m. In order to observe separately the signal emitted by dye-1 and the one emitted by dye-2, two 10 nm broad filters respectively centered at 590 nm (Figure 5.12a) and at 620 nm (Figure 5.12b) were inserted in the detection path. After this preliminary step in wide-field to find a good region of the sample, we preformed the measurement with a focused excitation spot at $(x, y) = (0, 0)\,\mu$m. Figure 5.12c shows the fluorescence of the sample, in which, thanks to the focused beam, only dye-1 is directly excited. As expected, the excitation produces a bright emission at its focus, but the PL of the two disks of dye-2 adjacent to the excitation position is also visible ($y \sim \pm 2.5\,\mu$m). We note that the PL of disks that are even farther away can be observed, as the one at $(x, y) = (6, -3)\,\mu$m. Moreover, it seems that the observation of dye-2's PL is directly correlated to the continuity of the dye-1's layer. When the dye-1 layer is continuous the PL of dye-2 is observed and vice-versa.

We then performed a spatial-spectral measurement, with the technique explained in Chapter 3. For this measurement, we image the PL on the slit of the spectrometer,

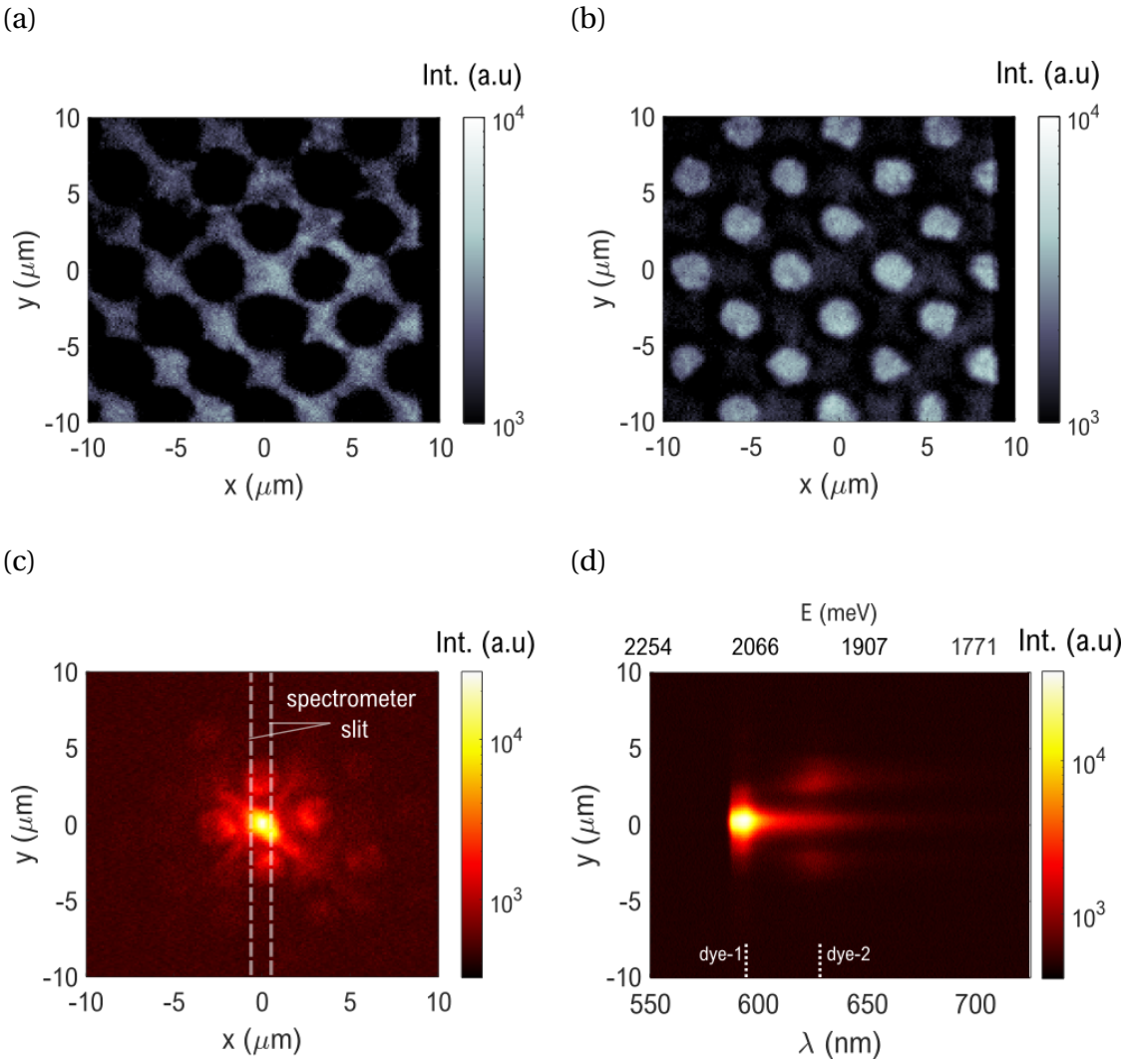


Figure 5.12 – Photoluminescence under a localized excitation. To assure the quality of the sample around the excitation zone we performed wide-field fluorescence images on the same region using a 10 nm band-pass filter centered at a) 590 nm to observe the disks of dye-1 and at b) 620 nm to observe the continuity of the film corresponding to dye-2. The colormap has a logarithmic scale. The images are centered at the excitation position. c) PL under a focused 532 nm laser excitation in which the emission of both dyes can be observed. d) Corresponding spatial vs spectral image. The light coming from the disks at $y = (0, \pm 2.5)\,\mu$m on c) is at the wavelength of dye-2 on d).

which is along the $y$ direction, centered on the excitation spot. For the sake of clarity the position of the slit is shown in Figure 5.12c. The position of the slit is coincident with the excitation spot and the size of the slit corresponds to $\Delta x = 1.04\,\mu$m on the sample plane. This value is chosen in order to prevent the detection of the PL coming from the disks adjacent to the excitation in the $x$ axis. For each pixel on the $y$ axis, a spectrum is measured. The result of this measurement is shown in Figure 5.12d. For $y = 0\,\mu$m we observe the PL of dye-1, while for $y = \pm 2.5\,\mu$m we observe the PL of dye-2. The dye-1 is directly excited by the laser, subsequently, it relaxes partially through the hybrid propagating modes of the system, which in turn excite dye-2. In this way, we observed energy transfer assisted by the polaritons product of the hybridization of dye-1 and dye-2 excitons, and the SPP. There is another fraction of the excited molecules of dye-1 that are uncoupled to the polaritons and emit as localized emitters.

As for the case of the PL under a wide-field excitation, we performed control experiments on a region without the silver film. Similar caution for the quality of the layer was taken as the case with the measurements on silver. As Figure 5.13a shows, the luminescence from the adjacent disks in the $y$ axis is very weak and can be barely resolved with a logarithmic color scale for the colormap. In the spatial vs. spectral measurement of Figure 5.13b, we found that only the disk at $y = -2.5\,\mu$m can be observed with low fluorescence. In Figure 5.14 we compare the total integrated spectra of the excitation of silver from Figure 5.12 with the glass control, and we normalized by the emission maxima. First, we observe a slight red-shift of the dye-1 peak on metal when compared to glass, as seen in previous studies [3]. Second, we observe that, although both spectra have an intensity of the same order of magnitude at 630 nm, a peak is only observable in the case where the SPPs are present.

We end this chapter by showing the PL emission under a localized excitation which is spatially separated from the detection. We work in the 0° configuration as shown in Figure 5.11b. To this aim, we focus the excitation in dye-1, while the spectrometer slit position is separated to the right of the laser excitation to coincide with the center of the closest dye-2 disks. This is shown on Figure 5.15a, where the vertical dashed lines show the position of the slit at $x = 0$ while the position of the excitation laser is $(-2, 0)\,\mu$m. Notably, the homogeneity of the dielectric layers of this region of the sample is optimal for the propagation of modes. We can detect the PL of the disks

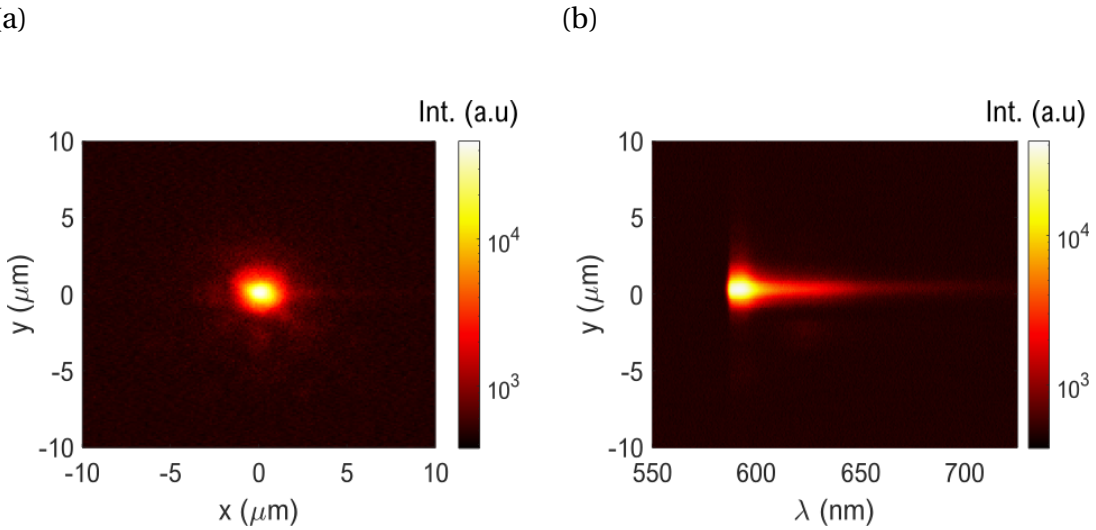


Figure 5.13 – Control measurement on glass. a) Localized photoluminescence of a region of the sample in which the silver was not deposited. We observe that the dye-2 disks on the surroundings of the excitation performed in dye-1 are barely visible even when the scale is logarithmic. b) Spatial vs. spectrum measurement. Even if there is light at the wavelength of the dye-2, this image shows that the radiation contribution coming from the disk is negligible.

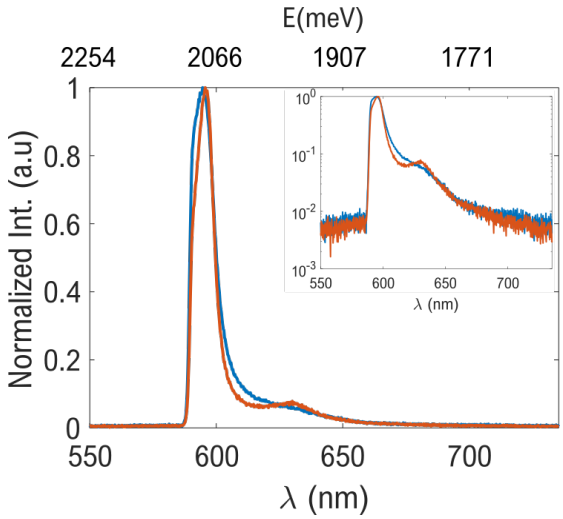


Figure 5.14 – Comparison of the integrated spectra for the localized excitation at dye-1 on silver (red curve) and glass (blue curve). The curves are normalized at their maxima intensity, which corresponds to the peak of dye-1. Even though both spectra have an intensity of the same order of magnitude at $\lambda = 630\,\text{nm}$, a peak is only observable in the case where the SPPs are present. The inset shows the same information on a logarithmic scale to better observe the spectral shape of the dyes' emission.

at distances $\sim 10\mu$m (out of the image range) away from the excitation. Figure 5.15b shows the spectrally dispersed image of a focused excitation separated from the detection by $\sim 2\,\mu$m. At $y = 0$ we observe light at $\lambda = 590$ nm, which comes from dye-1. For $y = \pm 3\,\mu$m we detect light at $\lambda = 630$ nm and this is the light coming from dye-2 and the LP. The most intense luminescent area is comprehended between $\pm 3\,\mu$m in which we observe the dye-1 excited along $x$ by propagating polaritons, and the adjacents disks of dye-2. Remarkably, we can observe the fluorescence emitted at 630 nm at $y \sim \pm 5\,\mu$m. Since at this position dye-2 is not deposited, the observable emission could be the result of the radiative relaxation of the system through the LP at wavelengths near to the exciton line of dye-2. A second effect observed in this spatial-spectral image, is that the luminescence centered around the dye-2 covered regions shifts to longer wavelengths as the position is farther from $y = 0$. This is probably due to the wavelength dependence of the propagation of the plasmon, which favors the red wavelengths to propagate farther.

(a) (b)

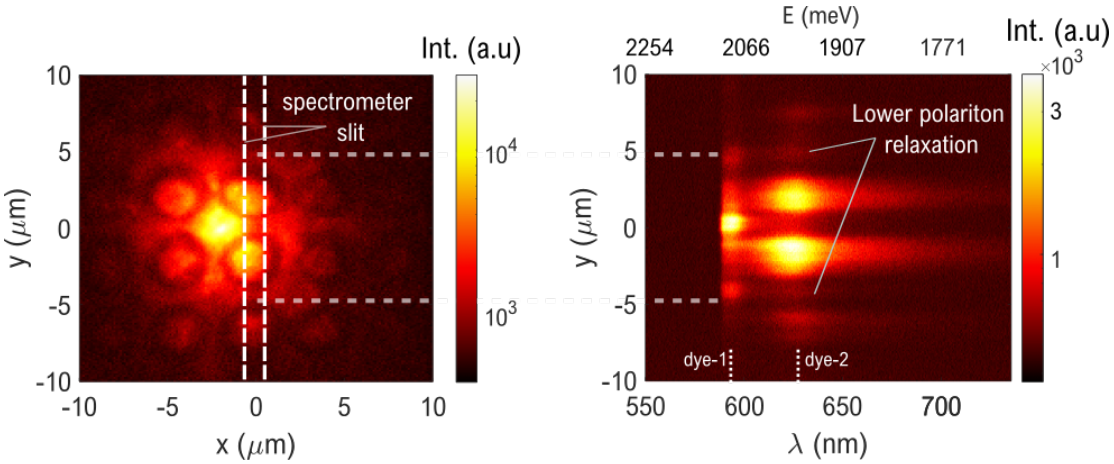


Figure 5.15 – Photoluminescence under a focused 532 nm laser excitation in the 0° configuration. The quality of the dielectric film has optimal properties for the hybrid modes to propagate through this region of the sample. For the spatial distribution of the spectrum, we performed a non-local measurement for which the center of the spectrometer slit is indicated with white dashed lines. b) Corresponding spectral distribution of the PL along the $y$ axis. We observe the emission of dye-1 excited at the same position of the excitation and the strong luminescence from the closest disks. At $y = \pm 5\,\mu m$, we observe the radiative relaxation of the system through the LP at the wavelength of dye-2.

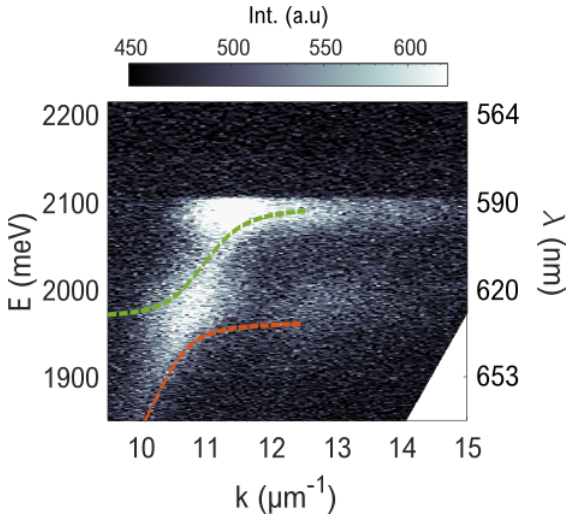


Figure 5.16 – PL dispersion for a localized excitation in the 0° configuration. The measurements in the direct space for this area with the same excitation are performed in the same configuration than Fig. 5.15, adding a Bertrand lens to disperse the angular emission pattern. By taking the dispersion, the relative position of the slit to the excitation spot is irrelevant. The intense emission from dye-1 at its excitonic line is saturated to better contrast the propagating modes emission and the background. The bending of the polaritons below the Rabi splittings is barely resolvable.

As already shown in Chapter 3, in our setup, we are also able to perform energy vs. wavevector measurements. In this case, we focused the excitation on a region containing dye-1 only, in the same area and 0° configuration as Figure 5.15, separating the slit 2 $\mu$m away from the laser focus. Figure 5.16 shows the dispersed emission pattern in $E$ vs. $k$ space. Since the collected signal in this configuration is much smaller than the signal collected under wide-field excitation, the excitation conditions are a trade-off between bleaching time, excitation intensity, and integration time. Therefore, the resulting SNR is lower than for the images acquired with wide-field excitation. We can barely recognize the presence of emitted light at the energy of the LP, the MP, and their horizontal asymptotes. As a guide for the eye, we superposed the calculated polariton lines from Figure 5.7(b). The modes are broadened due to the multiple interfaces constituting the sample. Since the excitation is centered on a region containing dye-1, detecting a PL signal at the other wavelengths confirms the observation of energy transfer towards dye-2 through hybrid modes under a localized excitation.

## 5.4 Conclusion

We studied the interaction between spatially separated J-aggregates with an SPP propagating at a silver/dielectric interface. In this system, the optical properties are determined by the interplay of the exciton/plasmon coupling and the non-local interaction between the active materials. Samples in which the deposition of two superimposed structures forming a Moiré pattern were successfully fabricated by the team of our collaborators at ILM by $\mu$CP, allowing to spatially separate dye-1 from dye-2. On these samples, reflectometry measurements were performed at ILM Lyon to measure the dispersion with a wide-field excitation. These measurements were complemented by spatio-spectral measurements of the photoluminescence dispersion realized at Institut Langevin, first with a wide field excitation, and then with a tightly focused excitation. One remarkable point is that the second stamp with dye-2 and its structuration did not significantly impact the already deposited dye-1, preserving the strong coupling of the ensemble. Wide-field reflectometry measurements of this system showed two anticrossings of the order of 100 meV, and three corresponding polaritonic branches. We characterized the system through a coupled oscillators model and observed an excellent agreement with the experimental data, demonstrating the applicability of the coupled oscillator model to describe this system. We studied the respective Hopfield coefficients for each polariton and observed that the experimental reflectivity correlates with the SPP fraction of the mode. Afterward, we showed how the strong coupling of the system channels the radiative emission through the lower polariton branch. We tested the energy transfer among the hybrid modes of the system under wide-field (measurements performed at ILM) and focused illumination (measurements performed at Institut Langevin). We observed that favoring the plasmon propagation by looking at zones where the dye deposition is free of defects favors the energy transfer between the dye-1, which acts as the donor, towards the dye-2, the acceptor. Furthermore, in an experiment in which the spectrometer slit is separated by $\sim 2\,\mu$m from the excitation focus, we observed light at wavelengths near the exciton line of dye-2, where it is not deposited. The origin of this emission could be a relaxation of the system through the lower polariton. We recall that in all the measurements presented in this chapter, we discounted any FRET effect since the different dyes are separated by a distances larger than 100 nm.

# References

[1] D. Li, C. Symonds, F. Bessueille, J. Plenet, A. Errachid, G. Wu, J. Shen, and J. Bellessa, *Journal of Optics A: Pure and Applied Optics* **11** (2009). 111, 112

[2] Y. Xia and G. M. Whitesides, *Annual review of materials science* **28**, 153–184 (1998). 111

[3] J. Bellessa, C. Bonnand, J. Plenet, and J. Mugnier, *Physical review letters* **93**, 036404 (2004). 117, 125

[4] K. Chevrier, J.-M. Benoit, C. Symonds, S. Saikin, J. Yuen-Zhou, and J. Bellessa, *Physical review letters* **122**, 173902 (2019). 117

[5] K. Georgiou, P. Michetti, L. Gai, M. Cavazzini, Z. Shen, and D. G. Lidzey, *ACS Photonics* **5**, 258–266 (2018). 117

[6] A. Kavokin, J. Baumberg, G. Malpuech, and F. Laussy, *Microcavities* (2008). 117

[7] D. M. Coles, N. Somaschi, P. Michetti, C. Clark, P. G. Lagoudakis, P. G. Savvidis, and D. G. Lidzey, *Nature materials* **13**, 712–719 (2014). 118, 120

# General conclusions and outlook

In this thesis, we studied the strong coupling between structured layers of J-aggregates with surface plasmon polaritons in the frame of a collaboration between the Institut Langevin and the Institut Lumière Matière (ILM) Lyon. We presented two different experiments, the first in which we probe the interaction of semiconductor quantum dots with the strongly coupled system. The second experiment corresponds to two spatially separated J-aggregates in strong coupling with the surface plasmon polariton. In this final chapter, we briefly summarize the main ideas presented in this manuscript, we recall the main results obtained in the two studied systems, and present perspectives for future works regarding the coupling between fluorescent emitters and surface plasmons.

We began this manuscript by a historical survey of the development of systems in which the Rabi splitting of electromagnetic modes with an excitonic transition is observable at room temperature (Chapter 1). We focused our attention to the experiments performed by our collaborators at ILM Lyon, in which they explored the properties of the strong coupling between J-aggregated TDBC and surface plasmon polaritons [1–3]. We also summarized the experiments performed in our group, in which long range energy transfer was observed by coupling emitters to surface plasmons [4; 5]. We then presented a general introduction to the strong coupling mechanism (Chapter 2), explaining the differences between weak and strong coupling with a classical model. Afterward, we discuss the specificities of the interaction between surface plasmon polaritons and fluorescent emitters. We show a simple model of coupled oscillators representing the interaction between light and matter and an electromagnetic model that predicts strong coupling based on the Transfer-Matrix Method. In Chapter 3, we showed the fluorescence microscopy setup through which we studied our samples. We detailed the real-space spectroscopy, in which, employ-

ing an EM-CCD with a square chip, we are able to perform spatio-spectral measurements, that allowed us to observe the spectral modification of the system along a particular direction. This is very useful considering that the samples that we used have a structure in the micron scale. At the end of Chapter 3, we showed the setup for the reciprocal-space spectroscopy. By dispersing the image of the objective's back focal plane on the spectrometer, we observed the relationship between the energy of the emitted (and reflected) photons from the sample with the in-plane wavevector of the propagating modes.

In Chapter 4, we presented the study of a sample consisting of quantum dots deposited on top of a layer of J-aggregates containing inactive areas produced by optical lithography. First of all, we studied the layer of J-aggregates on top of the silver film. We showed through reflectometry measurements that the J-aggregates entered in strong coupling with the surface plasmon polariton. We observed the formation of an upper and a lower polariton branch at the exciton/plasmon resonance with a corresponding Rabi splitting larger than 150 meV for different samples. By exciting the sample with a non-resonant laser, we observed how the strongly coupled system relaxes through the lower polariton while the emission from the upper polariton is barely detected. We then presented the photobleaching of circular areas on the J-aggregates layer creating regions with different optical properties within the sample. Afterward, we deposited QDs to probe the electromagnetic environment created by the strongly coupled system. For this purpose, we fabricated samples with QDs emitting at three wavelengths to probe different spectral ranges of the polaritons. We spectrally resolved the emission pattern of the different samples observing that the QDs weakly coupled to the available modes of the environment. We showed the progressive modification of the luminescence of the QDs, from their emission through a surface plasmon polariton mode in large areas (40 $\mu$m) of bleached J-aggregates towards their weak coupling to hybrid polaritons in areas where the organic dye is active. We also noticed that the presence of active J-aggregates in the surroundings modifies the overall spectrum of the QDs.

To model the system's photoluminescence of one of the samples, we collaborated with the Plasmonics and Quantum Nanophotonics team of the Laboratory Charles Fabry. We used a model based on the local Kirchhoff's law considering the thermal emission of ensembles of excited emitters. A chemical potential is introduced

to account for the gap in the distribution of states as a function of energy, which is characteristic of luminescent materials [6; 7]. We considered the multilayered structure containing the metallic silver film, the J-aggregates, and the QDs emitting at 2156 meV. The two layers of emitters were characterized by a refractive index and a chemical potential of radiation, unlike blackbody radiation whose chemical potential is zero. This model accurately reproduced our observations, and a difference in the chemical potential for the two species of emitters is extracted as a fitting parameter. The chemical potential difference quantifies the energy transfer between the two active layers of the sample. However, since the J-aggregates are suspected to be partially excited by the laser (even if care was taken to detune the latter from its absorption peak), further work is necessary to separate the contribution to the system's luminescence of the energy transfer from the direct laser excitation.

In Chapter 5, we studied the interaction between spatially separated J-aggregates with an SPP propagating at a silver/dielectric interface. Samples in which the deposition of two superimposed structures by $\mu$CP allow us to spatially separate dye-1 (J-aggregated TDBC) from dye-2 (J-aggregated S2278) were successfully fabricated. Wide-field reflectometry measurements of this system showed two anticrossings of the order of 100 meV, and three corresponding polaritonic branches. We characterized the system through a coupled oscillators model and observed an excellent agreement with the experimental data. We studied the respective Hopfield coefficients for each polariton and observed that the experimental reflectivity correlates with the SPP fraction of the mode. Afterward, we tested the energy transfer from dye-1, the donor, towards dye-2, the acceptor, by means of the hybrid propagating modes on the sample. We performed photoluminescence measurements, exciting the system under wide-field and focused illumination. In the former, we showed how the strong coupling of the system channels the radiative emission through the lower polariton branch. Using a focused excitation, we observed that zones, where the dye deposition is free of defects favor the propagation of the system's modes, which favors the energy transfer from dye-1 towards dye-2. Notably, we observed emission of the system at wavelengths near the exciton line of dye-2 in regions where only the layer of dye-1 is deposited, probably produced by the system's relaxation through the LP. We discounted any FRET effect since the different dyes are separated by a distance of 100 nm.

(a) (b)

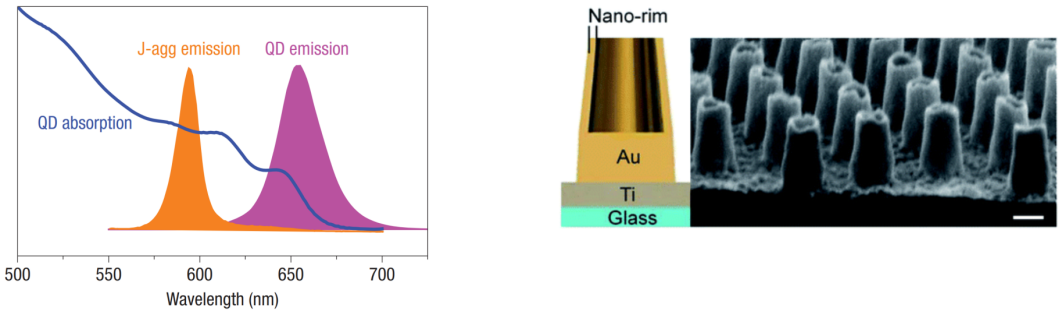


Figure 5.17 – (a) Emission and absorption spectra of QDs used in a study in which efficient energy transfer from J-aggregated TDBC was reported. The figure corresponds to the same study [8]. (b) SEM image of a sample containing an array of hollow Au nanopillars. A schematic representation of the nanofabricated Au structures is also shown. The scale bar is 100 nm. Image taken from [9].

To end this manuscript, we propose three perspectives regarding the hybridization of emitters to surface plasmons and optimization of energy transfer processes. The first corresponds to the study of similar systems as the ones in Chapter 4, but using quantum dots with an emission peak around $E \sim 1879\,\text{meV}$ ($\lambda = 660\,\text{meV}$). Research exploring the interaction of J-aggregates with red-shifted spectrally separated quantum dots has been already done [8], but without the plasmonic environment provided by the silver layer. This work reported a efficient energy transfer from the J-aggregates towards the QDs. Although this energy range is far from the resonance between the J-aggregates and the SPP (so the effects of the strong coupling are negligible), this system could be ideal for observing an energy transfer process in a plasmonic environment. First, the emission of the J-aggregated TDBC overlaps the large QDs absorption band that increases towards high energies, as shown in Figure 5.17(a). Second, a large red-shift of the QDs emission relative to the J-aggregates allows to spectrally separate the emitters. This is important to conclude if an energy transfer process is observed unambiguously. For example, in the sample in which we used quantum dots emitting at $E = 2042\,\text{meV}$, the emission peak overlapped the absorption of the J-aggregates and vice-versa, making it difficult to conclude the direction of the energy transfer. Moreover, supposing there is a significant energy transfer effect and the intensity of the QDs is high enough, the reduction of the concentration

of the QDs layer is a conceivable possibility. In this way, an attractive property of the quantum dots, which is that they are good candidates as single emitters, could be exploited.

The phenomenon of J-aggregated TDBC coupled to SPPs in different systems was deeply studied in this thesis. In a work in progress in our group, we expand this approach to study the coupling of such molecule with localized surface plasmon resonances (LSPR) supported by an array of hollow plasmonic conical pillars. The samples, shown in Figure 5.17(b), are provided by the Mesoscale Chemical Systems group from the University of Twente, and the fabrication process is described in [9]. Full-wave solution have shown that this structure has hot spots with enhancement factors of the electric field $\sim 150-400$. Moreover, the resonance of the nanostructure can be tuned towards the absorption peak of the J-aggregate exciton 590 nm, making it an ideal system to observe strong light-matter interaction with the organic dye. Furthermore, since this plasmonic device supports a highly dispersive modal structure, we search to characterize the strong coupling as a function of the angle without modifying a given parameter within the structure. Encouraging data, which are being acquired during the writing of this manuscript by Margoth Córdova-Castro and Kevin Chevrier, postdoctoral researchers at Institut Langevin, show a Rabi splitting that changes as a function of the excitation angle. This proves the interest of this sample. Indeed, usually, studies that explore the coupling between excitons and localized plasmon resonances require modifying a structural parameter of the resonator to tune its spectrum [10; 11], so that multiple samples are needed to span an energy range around the excitonic resonance.

# References

[1] J. Bellessa, C. Bonnand, J. C. Plenet, and J. Mugnier, *Phys. Rev. Lett.* **93**, 036404 (2004). 131

[2] S. Aberra Guebrou, C. Symonds, E. Homeyer, J. C. Plenet, Y. N. Gartstein, V. M. Agranovich, and J. Bellessa, *Phys. Rev. Lett.* **108**, 066401 (2012).

[3] K. Chevrier, J. M. Benoit, C. Symonds, S. K. Saikin, J. Yuen-Zhou, and J. Bellessa, *Phys. Rev. Lett.* **122**, 173902 (2019). 131

[4] D. Bouchet, D. Cao, R. Carminati, Y. De Wilde, and V. Krachmalnicoff, *Physical review letters* **116**, 037401 (2016). 131

[5] D. Bouchet, E. Lhuillier, S. Ithurria, A. Gulinatti, I. Rech, R. Carminati, Y. De Wilde, and V. Krachmalnicoff, *Physical Review A* **95**, 033828 (2017). 131

[6] J.-J. Greffet, P. Bouchon, G. Brucoli, and F. Marquier, *Physical Review X* **8**, 021008 (2018). 133

[7] P. Wurfel, *Journal of Physics C: Solid State Physics* **15**, 3967 (1982). 133

[8] Q. Zhang, T. Atay, J. R. Tischler, M. S. Bradley, V. Bulović, and A. Nurmikko, *Nature nanotechnology* **2**, 555–559 (2007). 134

[9] D. Jonker, Z. Jafari, J. Winczewski, C. Eyovge, J. Berenschot, N. Tas, J. Gardeniers, I. De Leon, and A. Susarrey-Arce, *Nanoscale advances* **3**, 4926–4939 (2021). 134, 135

[10] Y. Sugawara, T. Kelf, J. Baumberg, M. Abdelsalam, and P. Bartlett, *Physical review letters* **97**, 266808 (2006). 135

[11] J. Bellessa, C. Symonds, K. Vynck, A. Lemaitre, A. Brioude, L. Beaur, J. Plenet, P. Viste, D. Felbacq, E. Cambril, *et al.*, *Physical Review B* **80**, 033303 (2009). 135

# Appendix A

# Excitation of the J-aggregates layer with a 445 nm laser

Here, we present the PL measurements performed on a sample similar to the ones studied in Chapter 4 but only containing J-aggregated TDBC. It corresponds to the sample RUP1 previous to the deposition of the QDs layer emitting at 2156 meV. Figure A.1 shows that the PL of a layer of J-aggregates excited with a focused 445 nm laser is observable despite the detuning between the laser excitation wavelength and the absorption peak of the dye ($\lambda = 587$ nm).

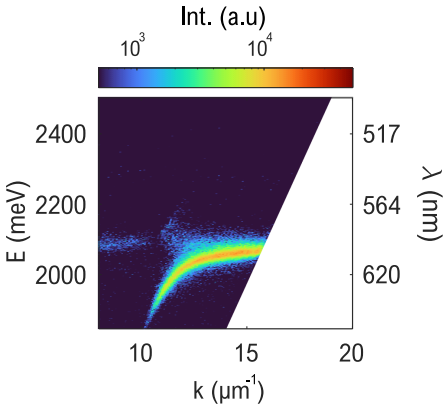


Figure A.1 – Photoluminescence of a layer of TDBC J-aggregates deposited on silver, excited by a 445 nm laser excitation. This sample corresponds to RUP1 before the deposition of the QDs. The experimental conditions are the same as the for the data shown in Chapter 4.

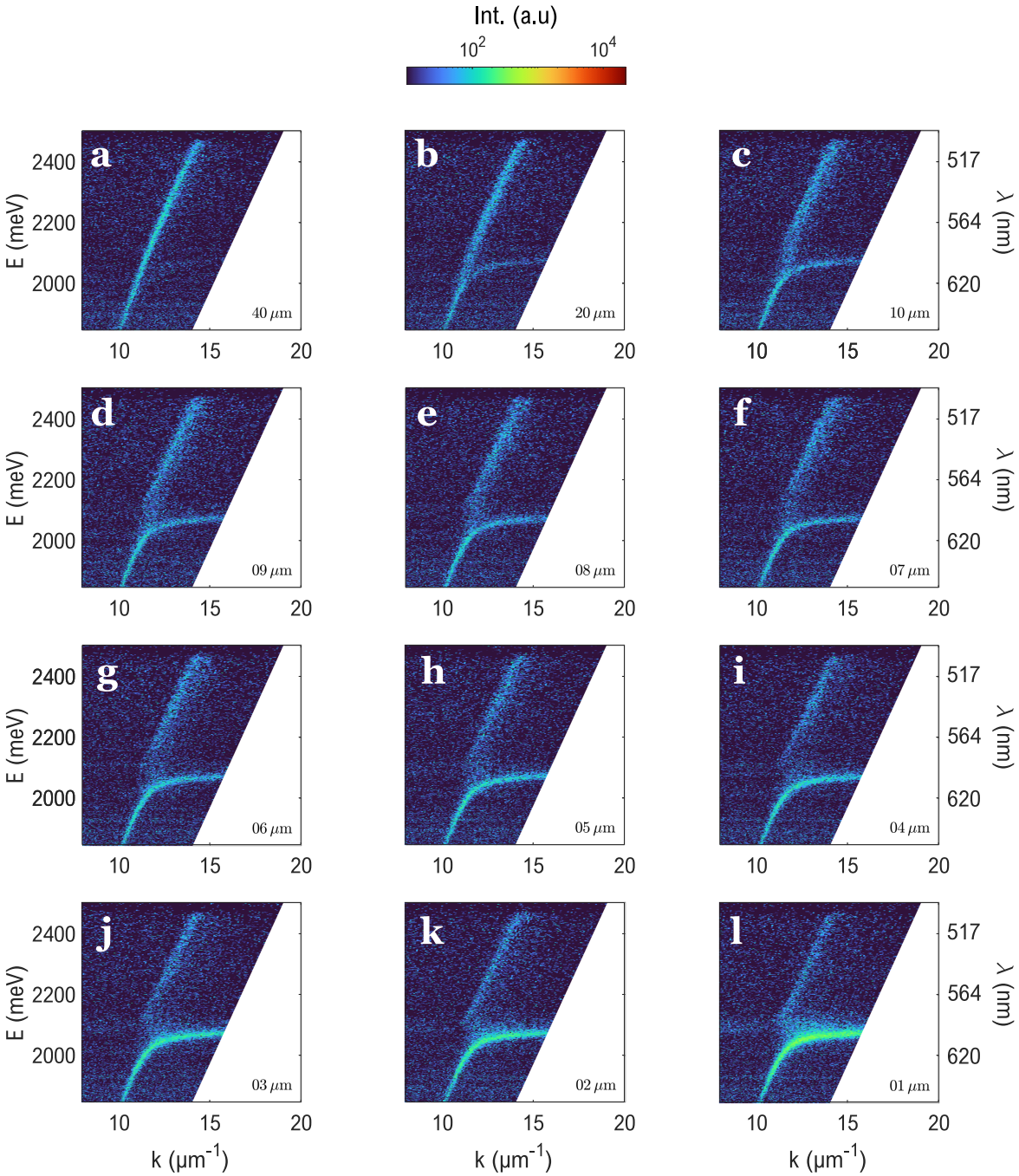


Figure A.2 – (a)-(l) Luminescence dispersion observed by focusing the laser at the center of the CPAs. The diameter is indicated in the lower right corner of the dispersion images.

Figure A.2 shows the PL emission patterns for all the CPAs in the lithography. As in Chapter 4, we focused the laser on the center of the CPAs and we polarized the collec-

tion in TM. For the 40 $\mu$m CPA, we observe light coupled to the SPP. In the 20 $\mu$m CPA, the emission from the lower polariton (LP) is observable and it increases for smaller CPAs. The signal arising from direct excitation is, for all the CPAs, much smaller than the signal detected when the QDs layer is present. It can be due to the plasmon which is launched by the laser or by the presence of some residual background coming from the CPAs.

# Appendix B

# Study of QDs decay rates

This appendix shows a series of experiments in which we attempted to understand the dependence of the QDs decay rate with the environment. In Chapter 4, we observed the presence of a slow component in the decay histogram that does not seem to be sensitive to the environments (dense layer of QDs embedded in PMMA deposited on silver and silver plus J-aggregates). In order to shed some light on this phenomenon, we performed some extra experiments that are presented in the following. Figure B.1 shows the decay rate histograms of a layer of diluted QDs on glass (in gray) compared to a histogram taken on a 40 $\mu$m CPA in sample RUP1. After $t = 50$ ns, the histograms converge to the same exponential decay.

To analyze the origin of this decay, we fabricated samples with a 70 nm Polyvinyl alcohol (PVA) layer deposited on a 50 nm silver film. Then, we spin-coated different layers of QDs on top, and so the PVA layer acts as an spacer. First, we fabricated samples with diluted solutions of QDs with, and without the PMMA that is present in the samples studied in Chapter 4. The different results are shown in Figure B.2(a). The sample without PMMA shows a decay rate of $\Gamma = 0.19\,\mathrm{ns}^{-1}$ (twice the value of the one with PMMA) in which the slow component does not have a significant contribution. We also compared two samples with and without PMMA, with a layer containing QDs with the same concentration of samples showed in Chapter 4. The results are shown in Figure B.2(b), in which we observe the histograms converging to the same slow component as the one observed in QDs on glass. We concluded that the presence of the PMMA, or the high concentration of QDs, screens the influence of the

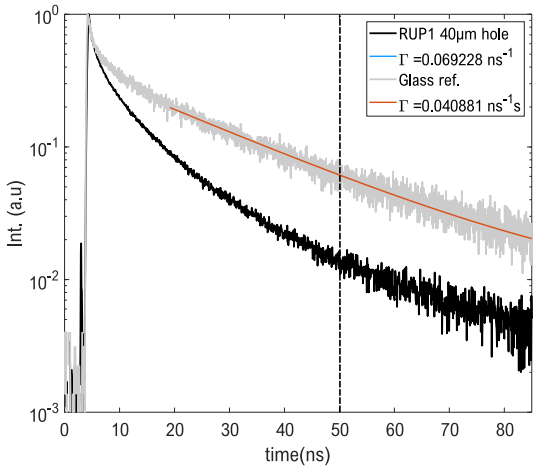


Figure B.1 – Normalized decay rate histograms for measurements of the center of a large 40 $\mu$m CPA on sample RUP1 (black curve) and diluted QDs on a glass coverslip (gray curve). For times $t > 50$ ns the histograms show the same exponential behavior. Orange and light blue curves are the result of a fitting procedure with a function that is the convolution between the IRF and a single exponential. The fitted value of Gamma is reported in the legend of the figure.

environment. Understanding the origin of this behavior, for which we have found no explanation in the literature, would require to perform a systematic study of the photophysical properties of the QDs themselves in absence of near-field coupling to J-aggregated TDBC or a metallic surface. As this was out of the scope of my thesis, we decided to abandon the study of the fluorescence decay rate to concentrate our efforts on the investigation of the dispersion relations.

(a) (b)

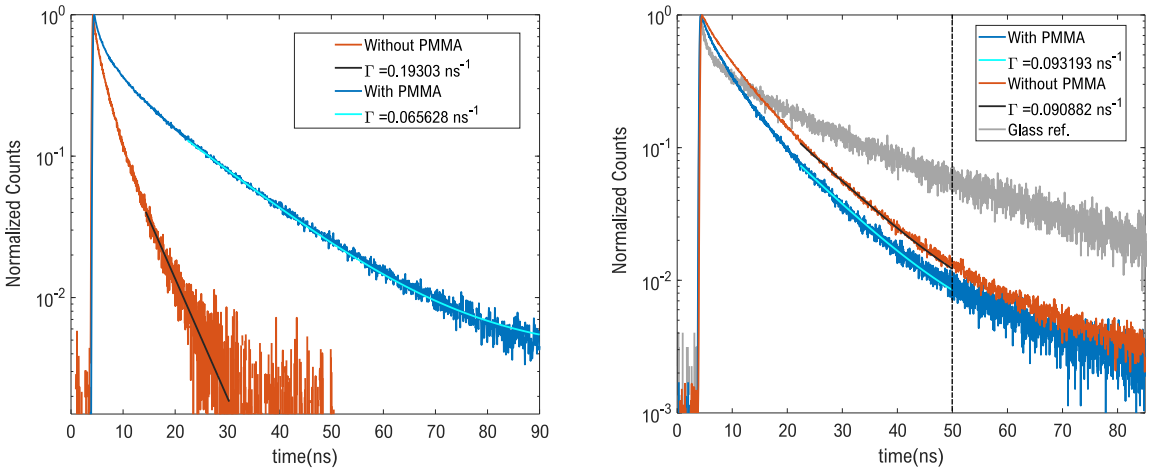


Figure B.2 – (a) Decay rate histograms for measurements of samples of diluted QDs spin-coated on top of a 70 nm PVA spacer. The blue curve shows the histogram for a sample in which the QDs are embedded in PMMA, while in the sample corresponding to the red curve there is no polymer matrix. (b) Same as (a) but with a concentration of QDs equal to the one used for samples RLP, RUP1 and RUP2. The decay rate histogram of diluted QDs on glass was added to observe how the curves converge to a similar exponential decay for times $t > 50$ ns. We performed a single exponential convoluted with the IRF fit in both curves to quantify the difference between decay rates. The values of Gamma resulting from the fit are reported in the legend of the figure.

# Appendix C

# Résumé substantiel (FR)

## Contents

Cette thèse a été réalisée dans le cadre du projet *Plashybrid* ANR dirigé par J. Bellessa de l'Institut Lumière Matière (ILM) et incluant trois autres partenaires : Institut Langevin (IL) (coordinatrice scientifique Valentina Krachmalnicoff), Institut de Science et d'Ingénierie Supramoléculaires (ISIS) (coordinateur scientifique Thomas Ebbesen), et Institut des Sciences Analytiques (ISA) (coordinateur scientifique François Bessueille). Nous avons également bénéficié de la collaboration avec l'équipe de Jean-Jaques Greffet du Laboratoire Charles Fabry de l'Institut d'Optique (LCFIO), et Thomas Pons et Sandrine Ithurria du Laboratoire de Physique et d'Étude des Matériaux (LPEM). Suite aux expériences pionnières réalisées à l'ILM sur le couplage fort avec les polaritons de plasmon de surface (SPP) et les agrégats J [1–3], l'objectif du projet ANR concernant ma thèse était de combiner les compétences disponibles à l'ILM pour synthétiser des échantillons et sonder la réponse optique globale d'un système fortement couplé avec celles de l'IL pour réaliser des mesures optiques locales sur des nanostructures plasmoniques avec émetteurs fluorescents [4; 5], pour étudier le comportement d'un système impliquant des plasmons de surface et des agrégats J en présence d'émetteurs autres que les agrégats J, selon leur nature et leur distribution spatiale. Nous avons décidé de pousser nos investigations dans deux directions : le couplage d'émetteurs quantiques faiblement couplés à un système fortement couplé et le couplage entre des systèmes déjà fortement couplés. À ces fins, des échantillons contenant des films d'argent et une couche structurée d'agrégats J ont été fabriqués, puis combinés avec des boîtes quantiques semi-conducteurs fournis par le LPEM. Au cours de mon doctorat, j'ai effectué plusieurs voyages au ILM consacrés à la production et à la caractérisation de tels échantillons. De même, nous avons bénéficié de la visite d'Antoine Bard, un doctorant de l'ILM, dans notre groupe à l'IL pour effectuer des mesures optiques locales. Pour approfondir notre compréhension de notre système, nous avons eu la chance de collaborer avec l'équipe du LCFIO dirigée par Jean-Jacques Greffet qui a proposé un modèle théorique basé sur une forme locale de la loi de Kirchhoff [6] pour décrire nos résultats expérimentaux. Des efforts importants ont ensuite été investis par sa doctorante Elise Bailly pour développer le code numérique adapté à notre système et utilisant nos paramètres d'entrée, ce qui a conduit à un très bon accord avec nos observations expérimentales [7; 8]. Dans les expériences présentées dans cette thèse, comme dans le développement des montages respectifs, j'ai travaillé avec Kevin Chevrier, qui a fait son doctorat

dans le groupe de Joel Bellessa et qui est actuellement chercheur postdoctoral à l'IL.

Dans cette annexe, un résumé détaillé de cette thèse de doctorat est présenté en montrant les parties principales de chaque chapitre. Si le lecteur souhaite approfondir un sujet particulier, il peut se référer au texte principal dans lequel des détails supplémentaires et des figures sont présentés en anglais.

## C.1 Chapitre I : Couplage fort entre les agrégats J et les SPPs

Dans ce chapitre, nous introduisons le contexte de la recherche présentée dans cette thèse. D'abord, nous passons en revue quelques articles séminaux sur l'observation du couplage fort entre un colorant organique et un SPP. Ensuite, nous nous concentrons sur les recherches précédentes concernant la cohérence spatiale des systèmes fortement couplés et le transfert d'énergie à longue portée observable entre les émetteurs fluorescents couplés aux SPP. Ces travaux constituent les pierres angulaires sur lesquelles nos expériences sont basées. Enfin, les objectifs spécifiques que nous poursuivons tout au long de ce travail sont présentés.

Le système lumière-matière le plus simple consiste en un émetteur à deux niveaux interagissant avec un seul mode électromagnétique supporté par l'environnement. L'étude de cette interaction remonte à la découverte de Purcell *et al.* [9] dans les années 1940 concernant l'interaction entre les noyaux d'hydrogène et les ondes électromagnétiques oscillant à des fréquences radio. Au cours des dernières décennies, le domaine s'est concentré sur l'étude de la modification des propriétés d'émetteurs actifs, comme les molécules fluorescentes, par l'interaction ou le couplage à des résonateurs optiques.

Le comportement de couplage fort d'un système est caractérisé par un écart d'énergie (*Rabi splitting*) des états du système à la résonance entre la transition radiative non couplée et le mode électromagnétique. Dans les années 1990, Lidzey *et al.* a publié le premier rapport concernant des colorants organiques en couplage fort : un grand écart de Rabi (plus de 100, meV) à température ambiante a été rapporté [10; 11]. La robustesse de cet effet de couplage fort a suggéré qu'il y avait des avantages à utiliser des colorants organiques dans la recherche de phénomènes de couplage fort

à température ambiante.

En 2004, Bellessa *et al.* [1] ont signalé un fort couplage dans un système constitué d'un film mince planaire d'un colorant, déposé par centrifugation sur une couche d'argent. Un écart de Rabi de 180 meV a été observé dans la relation de dispersion obtenue à partir de mesures de réflectivité. Dans cette étude, au lieu de modes résonnants dans des cavités optiques, les émetteurs se couplent aux modes de propagation à l'interface métal-diélectrique, c'est-à-dire les SPP. De plus, les films de colorants utilisés étaient des molécules de cyanine agrégées selon une disposition tête-queue (agrégats J) avec un grand moment dipolaire qui interagit fortement avec la lumière. Une autre caractéristique des agrégats J fortement couplés aux SPP est que l'hybridation des excitations électroniques et des modes plasmoniques entraîne des états cohérents étendus dans le milieu [12], dans lesquels la fluorescence de molécules distantes interfère. Des expériences explorant cette propriété ont également été menées par le groupe Bellessa à l'ILM Lyon, et ont conclu que la longueur de cohérence des modes fortement couplés des agrégats J et des SPP est de l'ordre de plusieurs microns [2; 3].

Le deuxième groupe d'expériences qui a jeté les bases de cette thèse concerne le transfert d'énergie assisté par les plasmons entre émetteurs fluorescents. Ce phénomène exploite la longueur de décroissance à l'échelle du micron de la propagation des SPP pour étendre l'interaction entre les fluorophores. Notre groupe à l'Institut Langevin a démontré une grande amélioration du transfert d'énergie entre une paire d'émetteurs donneur/accepteur dans le régime de couplage faible. Dans [4], Bouchet *et al.* ont dispersé de grosses billes fluorescentes (100 nm) incorporées dans une couche continue de molécules de colorant ont été déposées sur un film d'argent. Dans ce cas, le transfert d'énergie a été observé jusqu'à des distances de 7, $\mu$m entre la pompe et la sonde. Dans une deuxième expérience [5], Bouchet *et al.* ont rapporté un transfert d'énergie assisté par plasmon entre un point quantique unique et une perle fluorescente couplée à un nanofil. Ils ont notamment observé que les molécules de colorant à l'intérieur de la perle acceptrice présentaient le même comportement de clignotement que le point quantique.

Cette thèse vise à caractériser l'interaction entre différentes espèces d'émetteurs fluorescents dans un environnement supportant les SPPs. Nous étudions des échantillons multicouches structurés pour exploiter l'extension de cohérence des agrégats

J fortement couplés et la propagation à longue distance des SPP. Nous explorons deux systèmes différents : le premier consiste en des échantillons dans lesquels nous sondons l'interaction des boîtes quantiques avec les agrégats J/SPP fortement couplés. Le second correspond à deux colorants agrégés J qui sont séparés spatialement entre eux et hybridés simultanément avec le SPP.

## C.2 Chapitre II : Concepts de base

Ce chapitre présente le mécanisme de couplage entre la lumière et la matière dans le contexte de la plasmonique. Nous considérons un modèle simple pour l'interaction entre une onde électromagnétique monomode et un émetteur radiatif afin d'exprimer le écart de Rabi en fonction des fréquences des résonances non couplées. Nous discutons également des propriétés des SPPs et nous introduisons le formalisme de la méthode de la matrice de transfert, que nous utilisons pour obtenir les modes dans le système avec une géométrie multicouche et calculer la force du couplage entre les fluorophores et les SPPs.

Nous nous intéressons à l'étude de l'interaction d'une onde électromagnétique capable d'échanger de l'énergie avec un émetteur fluorescent. Nous considérons une molécule avec un moment dipolaire de transition $\boldsymbol{\mu}$ et une largeur de ligne intrinsèque $\gamma_0$, qui se trouve à l'intérieur d'un résonateur optique supportant un mode $\mathbf{E}_\mathbf{k}(t)$ avec une constante d'amortissement $\gamma$. Pour simplifier, considérons une onde harmonique $\mathbf{E}_\mathbf{k}(t) = \mathbf{E}_0 \cos(\omega t)$ comme le mode du résonateur. Dans l'interaction lumière-matière, la constante de couplage

$$\Omega = \boldsymbol{\mu} \cdot \mathbf{E}_\mathbf{k} \tag{C.1}$$

détermine le taux d'échange entre l'émetteur et le champ, qui à son tour établit la distinction entre le régime d'interaction à couplage faible et celui à couplage fort. Tout d'abord, considérons le cas où le taux d'échange est plus lent que le déphasage de l'un ou l'autre des constituants, c'est-à-dire si $\Omega \ll \gamma, \gamma_0$. L'amortissement du système surmonte l'interaction d'échange, et ce régime est connu sous le nom de *couplage faible*, et les états propres d'énergie du système restent inchangés. Cependant, un effet important de modification de la durée de vie de l'état excité de l'émetteur

subsiste. Si l'émetteur est résonant avec le mode électromagnétique, la densité optique des états vus par l'émetteur est augmentée par rapport à la densité des états du vide. Par conséquent, le taux d'émission spontanée est amplifié. Si $\Omega$ est nettement supérieur aux largeurs des lignes de résonance caractéristiques du système, les effets du couplage sont radicalement différents. Afin d'analyser le régime de couplage fort, présentons un modèle très simplifié dans lequel nous considérons un émetteur avec une résonance $\omega_0$ comme un système à deux niveaux échangeant de l'énergie avec un seul photon du mode de la cavité oscillant à une fréquence $\omega$. En résolvant le hamiltonien d'interaction (y compris les largeurs de ligne de l'émetteur et de la cavité), on obtient deux nouvelles solutions d'énergie $\mathscr{E}_{U,L}$ :

$$\mathscr{E}_{U,L} = \frac{\hbar}{2}(\omega+\omega_0) - \frac{i}{2}(\gamma+\gamma_0) \pm \frac{1}{2}\sqrt{\hbar^2\Omega_R^2 - (\gamma_0-\gamma)^2} \tag{C.2}$$

où $\Omega_R = \sqrt{\Omega^2+\Delta^2}$ est la fréquence de Rabi et $\Delta = \omega - \omega_0$ est le désaccord entre les fréquences. Nous observons que l'interaction donne lieu à deux nouveaux états hybrides séparés par l'écart de Rabi $\hbar\Omega_R$. La solution avec le signe plus est associée à la branche supérieure du polariton $\mathscr{E}_U$, et la solution avec le signe moins à la branche inférieure du polariton $\mathscr{E}_L$. Le terme *polariton* fait référence aux nouveaux modes mixtes entre le photon du résonateur et l'excitation de l'émetteur. À la résonance $\Delta = 0$, la différence d'énergie est le *vacuum Rabi splitting* $\hbar\Omega$. L'écart entre les deux nouveaux modes hybrides est la signature spectrale du régime de couplage fort.

Maintenant, nous portons notre attention sur les spécificités des SPPs. Un SPP est une onde électromagnétique de surface évanescente qui se propage à l'interface entre des milieux diélectriques et métalliques. Les expressions correspondantes pour les champs électriques et magnétiques sont obte-nues en appliquant les conditions de continuité à l'interface aux équations de Maxwell, et nous découvrons deux exigences pour l'existence d'un tel mode. Premièrement, les parties réelles des permittivités diélectriques des milieux ont des signes opposés $\mathrm{Re}\{\varepsilon_m\}\mathrm{Re}\{\varepsilon_d\} < 0$, ce qui est généralement satisfait par les métaux nobles $\varepsilon_m < 0$ et les diélectriques $\varepsilon_d > 0$ dans le spectre visible. La seconde, est que le mode de surface n'existe que dans la polarisation *magnétique transverse* (TM) dans laquelle le champ électrique a une composante parallèle à la propagation. Les propriétés d'un SPP air/argent sont condensées dans le diagramme de dispersion montré dans la figure C.1(a). Cette carte

de dispersion a été obtenue en utilisant la méthode de la matrice de transfert (TMM) pour les milieux stratifiés.

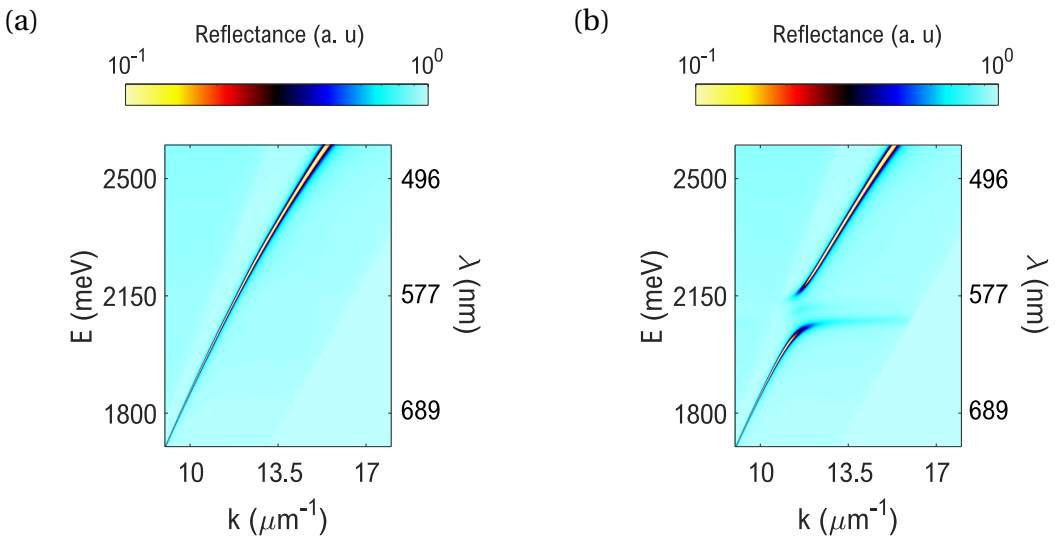


Figure C.1 – Réflexion calculée par TMM pour un système composé d'un substrat en verre $n_0 = 1,5$, d'un film mince d'argent 50 nm et d'une couche diélectrique d'épaisseur $l = 15$ nm et d'un indice de réfraction de fond $n_b = 1,72$. Dans (a), nous fixons la force d'oscillation généralisée de la couche diélectrique à $A = 0$ et dans (b) à $A = 5,0 \times 10^5$.

Il est important de noter que les métaux présentent un amortissement important dû aux pertes ohmiques des électrons entraînés par le champ SPP. Par conséquent, $\varepsilon_m$ est complexe, et par conséquent, la propagation du plasmon de surface est finie. Par exemple, un SPP se propageant à une interface air/argent à 445 nm a une longueur de propagation de 13.0 $\mu$m si l'on suppose que les pertes ohmiques sont la seule source d'amortissement. Dans l'espace réciproque ou vecteur d'onde, le champ SPP a une distribution lorentzienne [13; 14] et la dissipation se traduit par une largeur finie pour la résonance.

Nous nous intéressons au couplage fort entre les émetteurs fluorescents qui se trouvent au-dessus d'un film d'argent supportant les SPPs. Pour les expériences que nous réalisons, nous déposons des films minces contenant les émetteurs au-dessus de l'argent. Il s'agit de matériaux diélectriques homogènes où les charges sont liées à leurs molécules respectives et ne peuvent pas circuler indéfiniment en réponse à un champ électrique. On peut alors considérer que les particules oscillent autour de leur site en réponse à des champs extérieurs. Dans cette perspective, la transition lu-

minescente est une résonance des charges à un $\omega_0$ donné. Sous un champ électrique $\mathbf{E}(t) = E_0\, e^{i\omega t}\hat{\mathbf{x}}$ parallèle au moment dipolaire de la molécule. Ce modèle montre que le milieu se comporte comme un résonateur lorentzien, avec une permittivité diélectrique :

$$\varepsilon_d = \varepsilon_b + \frac{A}{(\omega_0^2 - \omega^2 - i\gamma\omega)} \tag{C.3}$$

où la constante $A$ est appelée force d'oscillation généralisée et $\varepsilon_b$ est une constante diélectrique de fond.

Avec cette approche, le comportement de couplage fort peut être retrouvé à travers les équations de Maxwell intégrées dans le TMM pour l'interaction entre la lumière et un milieu stratifié composé d'un film mince métallique et d'une couche diélectrique avec un indice de réfraction $n = \sqrt{\varepsilon_d}$. Nous observons l'existence d'un anticroisement dans la réflectance d'un tel système lorsque la force de l'oscillateur est suffisamment élevée . Dans la figure C.1(a), la force de l'oscillateur généralisé $A$ a été fixée à zéro et la dispersion d'un SPP peut être observée. En revanche, la figure C.1(b) montre un comportement de couplage fort lorsque l'on définit $A = Ne^2 f / V\varepsilon_0 m = 5.0 \times 10^5$.

## C.3 Chapitre III: Montage optique

Ce chapitre décrit le montage optique basé sur un microscope à fluorescence inversé que nous avons modifié pour caractériser en détail le comportement des fluorophores dans des environnements plasmoniques. Nos échantillons consistent en des structures multicouches avec des motifs lithographiés à l'échelle du micron. Pour les caractériser rigoureusement, nous contrôlons la position de l'excitation et de la détection optique au moyen d'un montage de microscopie à fluorescence de haute précision. Nous avons mis en place un chemin de détection pour observer l'émission dans l'espace du vecteur d'onde réciproque afin d'étudier les modes de propagation qui apparaissent à l'interface entre les milieux diélectrique et métallique. Nous avons complété les informations sur la dépendance spatiale en mesurant les temps de décroissance de la fluorescence avec un module de comptage de photons uniques corrélés dans le temps (TCSPC) après avoir collecté le signal de fluorescence avec une

diode à avalanche à photons uniques (SPAD).

Fait important, nous réalisons l'imagerie et la spectroscopie de l'espace réciproque ou de Fourier. La dépendance angulaire des modes de propagation fuyants apporte des informations essentielles sur les modes électromagnétiques dans un environnement donné. En ajoutant une lentille de Bertrand, nous pouvons facilement faire passer notre configuration d'imagerie de l'espace réel à l'espace réciproque et caractériser l'émission fluorescente en fonction du vecteur d'onde dans le plan de l'échantillon. De plus, nous avons inclus un chemin d'illumination en lumière blanche pour effectuer des mesures de réflectométrie dans l'espace de Fourier.

Nous avons réalisé les expériences présentées dans cette thèse sur un microscope inversé (IX83, Olympus) posé sur une table optique stabilisée pneumatiquement. La lumière est couplée au microscope par deux ports qui permettent de configurer l'excitation et la détection de l'échantillon. Nous utilisons différentes sources lumineuses pour l'excitation en fonction de l'expérience. Pour la microscopie de fluorescence, nous disposons d'un laser pulsé supercontinuum (SuperK Extreme EXB-6, NKT) filtré par un filtre passe-bande accordable (SuperK VARIA, NKT), et pour les mesures de réflectométrie, nous utilisons une lampe blanche à incandescence (EK-1, Euromex). Pour les expériences présentées, nous utilisons un objectif à immersion d'huile (UPLAPO100 XOHR, Olympus) avec une ouverture numérique NA = 1,50.

Une fois que le signal traverse le microscope, il est focalisé par une lentille de tube $f$ = 180 mm. A l'intérieur du microscope, un miroir à bascule automatique dirige la lumière par un port de sortie vers des optiques montées sur la table optique ou vers un EM-CCD (iXon 897, Andor) fixé sur le côté droit du microscope. Le chemin de détection situé sur le côté gauche du microscope est utilisé pour les mesures spectrales et de durée de vie. Pour l'analyse en espace réel de l'émission de fluorescence, nous utilisons deux détecteurs différents. Dans une branche du montage, l'image coïncide avec la fente d'ouverture du spectromètre et dans l'autre avec une photodiode à avalanche. L'image directe intermédiaire permet de réaliser une microscopie confocale en plaçant un sténopé qui filtre spatialement le signal.

La combinaison du spectrographe et de la puce carrée de la caméra permet d'acquérir de grandes surfaces d'un échantillon et de les disperser en longueur d'onde. Contrairement aux spectromètres dotés de puces rectangulaires étroites, cette configuration de mesures présente l'avantage de distinguer des caractéristiques en im-

agerie directe et de les relier à la distribution spectrale. Pour une excitation par faisceau focalisé, le laser est aligné au centre de la fente. Lorsqu'il est dispersé, l'image entière peut être intégrée pour observer la réponse spectrale globale. Cependant, dans les environnements spatialement inhomogènes, une analyse du spectre le long de la fente est plus pratique.

Pour les échantillons supportant des plasmons de surface ou, plus généralement, une émission dépendant de la polarisation, un polariseur peut être installé avant le spectromètre. Son orientation relative par rapport à l'axe de la fente définit une polarisation préférentielle d'observation. Dans le cas des SPPs, un polariseur orienté le long de la fente permet la détection des plasmons de fuite se déplaçant dans la même direction que la fente alors qu'une orientation perpendiculaire bloque leur détection.

Dans une autre voie du montage, la lumière peut être dirigée vers un SPAD (Single Photon Avalanche Diode PDM-Red, Micro Photon Devices) dont le diamètre de la zone active est de 50 $\mu$m. En effectuant des mesures de comptage de photons uniques corrélés dans le temps (TCSPC), nous cherchons à observer la modification de la dynamique temporelle du système.

La nature dispersive des polaritons plasmoniques de surface nécessite d'étudier la distribution angulaire du rayonnement émis par un échantillon plasmonique. Le rayonnement des SPPs est émis à des angles plus grands que l'angle d'incidence critique de l'interface air/verre. De plus, ils peuvent fuir à travers le métal et se coupler au champ lointain dans le milieu du substrat. La condition pour que cela se produise est la correspondance de momentum entre la propagation de la lumière dans le plan et le plasmon :

$$k_{\mathrm{spp}} = k_s \sin(\theta) \tag{C.4}$$

où $\theta$ est l'angle entre la normale et la direction de propagation de la lumière dans le substrat.

Dans une configuration de microscopie, l'information du modèle d'émission angulaire d'une image est contenue dans le plan focal arrière (BFP) de l'objectif du microscope. La lentille de l'objectif fait correspondre chaque direction $\theta$ de la lumière qui entre en elle à un point $\mathbf{r}(\theta)$ sur le BFP. La figure C.2 montre la configuration du dispositif permettant d'imager la BFP de l'objectif au niveau de la fente du spectromètre. Le schéma présente le tracé des rayons du centre du BFP, qui corre-

spond à un point de convergence pour les rayons qui entrent dans la lentille frontale de l'objectif à incidence normale. Après la lentille relais, une image intermédiaire du BFP est formée. Une lentille, appelée lentille de Bertrand, associée à une seconde lentille devant le détecteur, est utilisée pour former l'image du BFP soit sur la fente d'entrée du spectromètre.

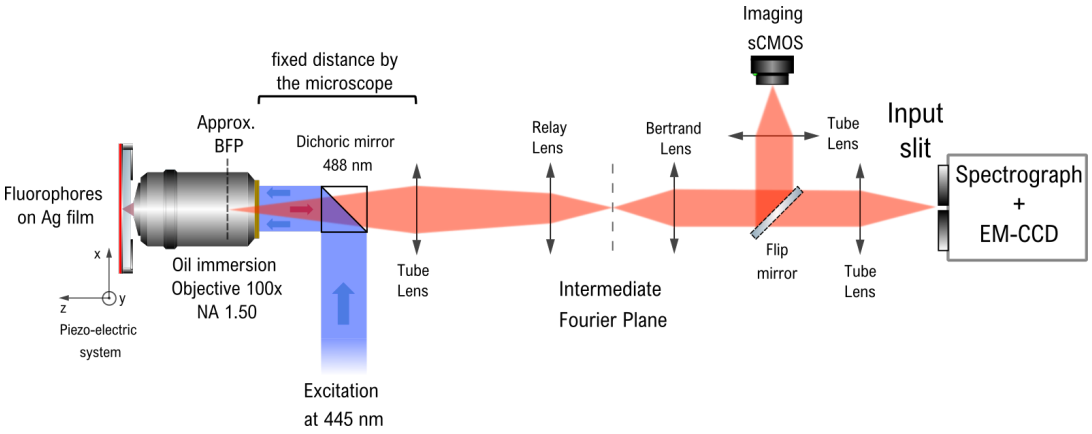


Figure C.2 – Schéma de la configuration et du traçage de rayons pour réaliser la spectroscopie de l'image de l'espace réciproque d'échantillons fluorescents. L'excitation laser entrante est focalisée sur l'échantillon dont la position est contrôlée par des actionneurs piézoélectriques. L'émission est dirigée vers l'ouverture de la fente d'entrée du spectromètre. Une lentille de Bertrand est insérée pour conjuguer l'image du plan de Fourier intermédiaire avec les détecteurs.

En utilisant le théorème du sinus optique, nous pouvons déterminer l'angle d'émission en tout point du BFP. Par conséquent, en dispersant l'image de la BFP dans le spectromètre, nous pouvons obtenir le momentum dans le plan correspondant à la propagation du plasmon s'échappant de l'échantillon. En reliant l'angle et l'axe de la longueur d'onde, nous pouvons obtenir le vecteur d'onde dans le plan correspondant de tous les points d'une image BFP. La figure C.3 montre les diagrammes $E$ vs. $k$ pour les mesures effectuées dans un système composé d'une couche de boîtes quantiques sur un film d'argent. La figure C.3(a) montre une mesure de réflectométrie (effectuée en remplaçant le laser par une lampe blanche) dans laquelle la large bande d'absorption du plasmon est observée. La figure C.3(b) montre la luminescence du système émettant à travers la ligne SPP et centrée à l'énergie des boîtes quantiques ($\sim 2040\,\text{meV}$).

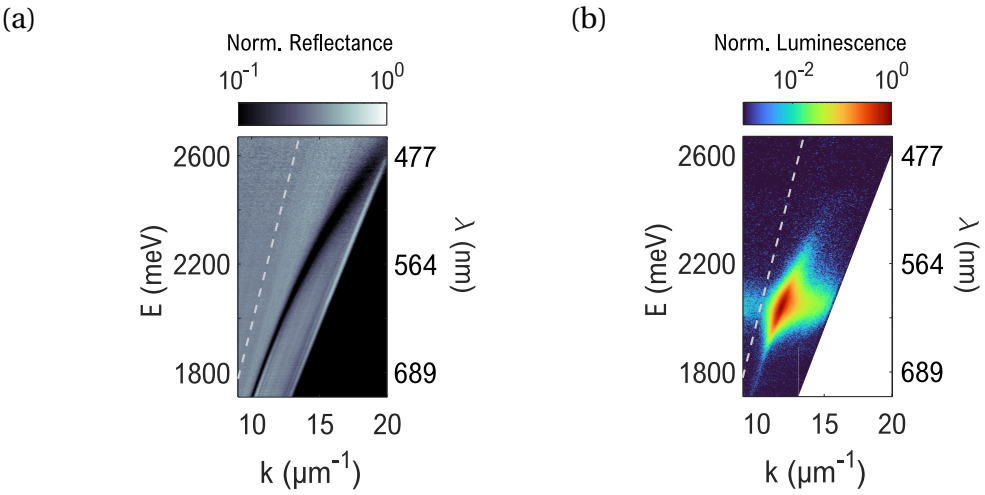


Figure C.3 – $E$ vs. $k$ diagrammes pour (a) la réflectométrie et (b) les mesures de luminescence d'un échantillon composé de boîtes quantiques reposant sur un film mince d'argent. En (a), le caractère large bande du plasmon est visible. En (b), l'émission à bande étroite des boîtes quantiques peut être observée le long du mode plasmonique. La ligne lumineuse $E = \hbar ck$ (ligne pointillée grise) indique l'angle critique $\theta_c$ entre l'air et le verre.

## C.4 Chapitre IV: Des boîtes quantiques faiblement couplées à un système fortement couplé

Ce chapitre présente le travail principal de cette thèse. Nous avons sondé l'environnement électromagnétique créé au voisinage d'un système fortement couplé composé d'agrégats J et d'un SPP. Pour cette étude, nous avons utilisé un film mince d'argent continu dans lequel des boîtes quantiques (ou quantum dots QDs) nanocristallins interagissent avec le doublet fortement couplé via des modes de propagation, incluant des SPP et des polaritons hybrides exciton/SPP. Les QDs, qui ont une faible force d'oscillation par rapport au colorant organique, se couplent faiblement aux modes de champ proche de l'échantillon, ce qui permet de les utiliser comme émetteur de sonde. Afin d'exploiter cette propriété, nous avons utilisé trois espèces de QDs dont l'émission chevauche différentes régions énergétiques des polaritons fortement couplés. Le travail présenté ici s'inscrit dans le cadre d'une collaboration entre l'équipe Matériaux et Nanostructures Photoniques, dirigée par Joel Bellessa à l'ILM Lyon, et notre équipe à l'Institut Langevin. La lithographie optique et la fabrication de certains échantillons ont été réalisées à l'ILM Lyon, tandis que la caractérisation optique

des échantillons a été effectuée à l'Institut Langevin pendant ma thèse. Nous remercions Alban Gassenq pour la conception et la réalisation de la lithographie optique, et Jean-Michel Benoit, Clémentine Symonds, et Joel Bellessa pour le processus de fabrication des échantillons et les nombreuses discussions scientifiques très stimulantes que nous avons eues sur toutes les subtilités du couplage fort.

Nous utilisons une couche de TDBC agrégée J comme matériau actif pour coupler fortement les SPP, et des boîtes quantiques multicellulaires nanocristallins comme sonde pour les modes fortement couplés et leur extension. Le TDBC est un colorant cyanine organique qui est capable de s'auto-assembler à des concentrations élevées en solution. Il en résulte une mise en ordre appelée agrégation J, qui se traduit par un rétrécissement et un décalage vers le rouge de l'émission des agrégats J par rapport à leurs monomères correspondants. Comme émetteurs de sondes optiques, nous utilisons trois espèces de QDs avec des noyaux CdSe et des multicoques CdS/CdZnS/ZnS avec des pics d'émission à 544, nm, 575, nm et 607, nm, qui ont été synthétisés par Thomas Pons et Sandrine Ithurria au Laboratoire de Physique et d'Étude des Matériaux (LPEM), ESPCI.

Pour la fabrication des échantillons, nous avons d'abord déposé le TDBC agrégé en J sur un film d'argent de 50 nm et réalisé une lithographie optique contenant des zones circulaires photo-blanchies (CPAs). Ensuite, nous avons déposé sur le dessus une couche de QDs noyés dans une matrice polymère. Nous avons fabriqué trois échantillons différents, cependant, dans ce résumé, nous ne parlerons que de celui avec les QDs émettant à 575, nm, nommé RUP1. Un schéma de l'échantillon est présenté dans la figure C.4.

Après le dépôt de la couche de QDs/PMMA, un seul anticroisement caractérise les dispersions de réflectivité à l'énergie du TDBC agrégé (2101 meV) avec un écart de Rabi de 152.7 meV. L'absence d'un second anticroisement dans la réflectivité, suggère que les QDs ne sont pas en couplage fort avec le reste du système. Cependant, les QDs sont soumis à un environnement électromagnétique déterminé par l'hybridation entre les agrégats J et les SPPs. Nous montrons le couplage faible des QDs aux polaritons fortement couplés par spectroscopie de l'espace réciproque de la luminescence de l'échantillon. Nous avons exploré l'interaction des QDs avec le reste du système en excitant différentes régions de l'échantillon avec une excitation laser focalisée de 445 nm. Nous avons étudié le comportement PL en comparant les

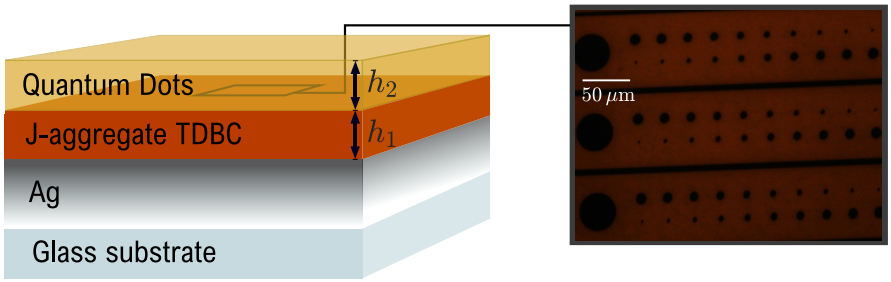


Figure C.4 – Schéma d'un échantillon multicouche constitué de deux films minces fluorescents déposés sur une couche de 50,nm d'argent évaporé sur un substrat en verre. La première couche déposée, d'épaisseur $h_1$, contient l'agrégat J TDBC. L'image de microscopie en champ sombre montre la lithographie optique réalisée sur cette couche, dans laquelle l'exposition à un laser UV a photo-blanchi les zones sombres circulaires. Ensuite, une deuxième couche d'épaisseur $h_2$ contenant des boîtes quantiques est déposée.

cas de QDs sur de grands CPAs de $\varnothing = 40\,\mu$m à la situation dans laquelle les QDs se trouvent au-dessus d'une région qui n'a pas été lithographiée. Tous les diagrammes $E(k)$ présentés sont polarisés TM pour augmenter le rapport du signal provenant des modes polaritoniques par rapport à l'émission non couplée.

Pour comprendre la contribution des QDs à la luminescence totale des échantillons, nous devons considérer que l'émission des agrégats J actifs lorsqu'ils se couplent fortement au SPP n'est observée que par la branche polariton inférieure (LP). Nous remarquons également que la relaxation de la luminescence est observable malgré le désaccord entre la longueur d'onde d'excitation du laser et le pic d'absorption du colorant ($\lambda = 587\,$nm). Nous présentons maintenant les résultats de l'échantillon RUP1, dans lequel l'émission des QDs est résonante avec la faible gamme d'énergie du polariton supérieur ($E = 2156\,$meV), et sa largeur spectrale chevauche le gap. La figure C.5a montre l'émission de QDs excités au centre d'un CPA de 40,$\mu$m. Nous avons observé la canalisation efficace du rayonnement des QDs par un mode SPP étroit. La figure C.5b montre l'émission de QDs excités au-dessus d'une zone homogène non lithographiée. De façon remarquable, nous observons que l'émission des QDs est partiellement canalisée à travers le polariton haut (UP) du système fortement couplé. Comme mentionné précédemment, l'état UP a une PL négligeable lorsque les seuls émetteurs actifs dans le système sont les agrégats J.

Maintenant on montre comment le comportement du système multicouche composé du film d'argent, des agrégats J et des QDs est reproduit en modélisant sa pho-

(a) (b)

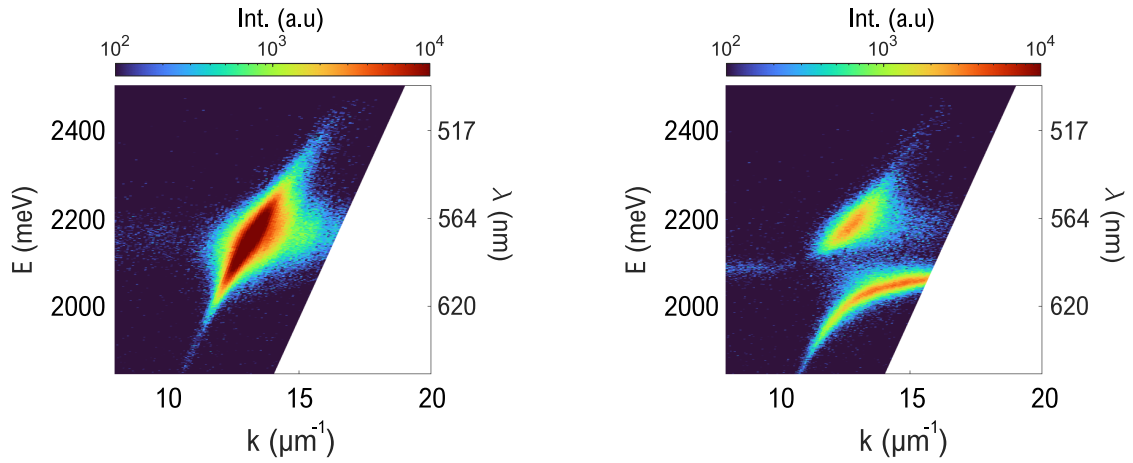


Figure C.5 – Dispersion de la luminescence des QDs (a) dans un grand CPA de $\varnothing = 40\,\mu$m émettant par le mode plasmonique et (b) où les agrégats J sont non blanchis, dans lesquels l'émission est canalisée par les modes fortement couplés. Notez que le spectre des QDs chevauche l'espace autour de l'anticroisement et des deux polaritons.

toluminescence à l'aide de la forme locale de la loi de Kirchhoff, qui étend la validité de la loi de Kirchhoff aux corps non isothermes avec des photons à potentiel chimique non nul [6]. Cette approche a été développée et appliquée à nos données par l'équipe de Jean-Jacques Greffet au Laboratoire Charles Fabry (LCFIO). Ils ont utilisé une loi de Kirchhoff locale établissant l'égalité entre le taux d'absorption local et le taux d'émission local dans une structure multicouche qui tient compte du substrat de verre, de la couche mince d'argent et des couches d'agrégats J et de QDs. Il a été démontré [6] que la loi de Kirchhoff locale peut être utilisée pour modéliser la photoluminescence des semi-conducteurs (tels que les QDs) et des molécules de colorant (telles que le TDBC). Ce cadre théorique est donc bien adapté à la description des échantillons étudiés dans ce manuscrit. Nous étudions l'échantillon RUP1 contenant des QDs qui émettent à 2156 meV, en supposant que dans les deux couches actives, l'ensemble des émetteurs est thermalisé.

La luminescence de ces matériaux peut être considérée comme une émission thermique, avec un potentiel chimique fini pour les photons $\mu$ représentant le nombre d'émetteurs dans l'état excité [15]. De cette manière, la loi de Kirchhoff modifiée

incluant le potentiel chimique des photons est donnée par le produit de l'absorptivité par la radiance du corps noir généralisé de Planck $B(T,\omega-\mu/\hbar) = B(T,\omega,\mu)$ [6; 15] : Explicitement,

$$B(T,\omega,\mu) = \frac{\omega^2}{8\pi^3 c^2} \frac{\hbar\omega}{\exp(\frac{\hbar\omega-\mu}{k_B T}) - 1} \tag{C.5}$$

où $T$ est la température du corps, $\omega$ la fréquence, et $\hbar$ la constante de Planck. Par conséquent, la puissance totale émise par un système thermalisé, dans l'angle solide $d\Omega$ dans un domaine spectral $d\omega$ est de

$$S(\Omega,\omega) = \frac{dP_e^{(l)}}{d\Omega\, d\omega} = \int_V d^3\mathbf{r}' \alpha_{abs}^{(l)}(-\mathbf{u},\mathbf{r}',\omega) \times B(T,\omega,\mu) \tag{C.6}$$

où $\alpha_{abs}^{(l)}$ est la densité de la section transversale d'absorption qui dépend de la forme du système et de son orientation relative par rapport à la lumière incidente, $\mathbf{u}$ la direction du mode incident, $\mathbf{r}'$ la coordonnée de position de l'absorbeur, et l'exposant $l$ spécifie la polarisation [6]. Notre échantillon consiste en un système isotrope dans un plan donné. Afin d'établir la dépendance angulaire avec l'axe normal à ce plan, nous écrivons l'équation C.6 en fonction de l'angle solide $\Omega$ :

$$S(\Omega,\omega) = A(\Omega,\omega) \times B(T,\omega,\mu) \tag{C.7}$$

Pour tenir compte de l'émission des agrégats J et des QDs, nous considérons l'émission totale comme la somme des photoluminescences individuelles de chaque couche. Par manipulation algébrique, nous obtenons une expression dans laquelle la luminescence de chaque matériau actif peut être traitée individuellement. La photoluminescence totale de notre système est alors égale à la somme du rayonnement thermique des deux couches, l'émission des QDs étant pondérée par la différence de potentiel chimique des ensembles d'émetteurs. Les figures C.6a et C.6b montrent l'émission indépendante des deux types d'émetteurs couplés aux modes polaritoniques de l'échantillon. La figure C.6c est calculée en utilisant le paramètre libre $\Delta\mu$ pour réproduire l'intensité relative observée dans les données expérimentales (figure C.5b).

La valeur ajustée pour la différence de potentiel chimique est $\Delta\mu = \mu_{\text{QDs}} - \mu_{\text{Jagg}} =$

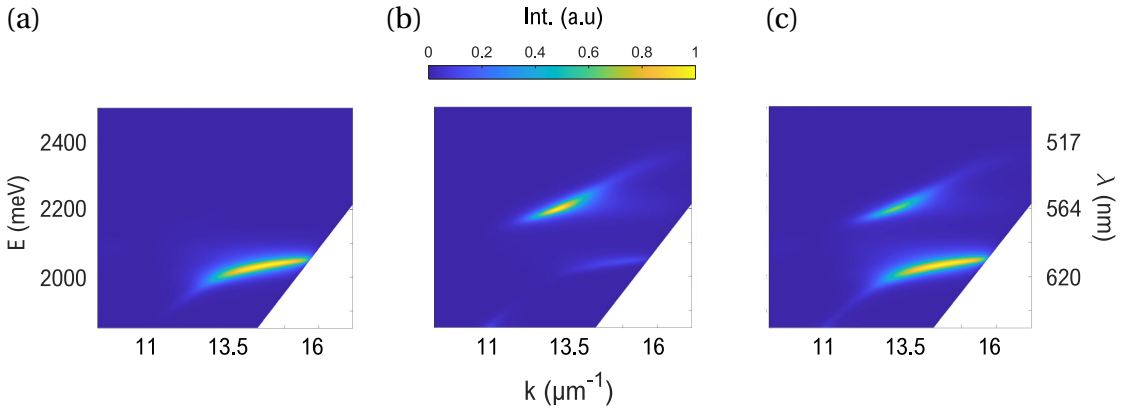


Figure C.6 – Calcul du schéma d'émission d'un système multicouche composé d'un substrat en verre, d'un film mince d'argent $h = 50\,\text{nm}$, d'une couche d'agrégats J TDBC $h_1 = 18\,\text{nm}$ et d'une couche de QDs $h_1 = 15\,\text{nm}$ avec une émission à 2156 meV. La méthode utilise un algorithme d'analyse rigoureuse des ondes couplées (RCWA) avec le modèle de Kirchhoff décrit dans le texte principal. L'émission indépendante des couches est représentée en (a) pour les agrégats J et en (b) pour la couche de QDs. (c) montre l'intensité du système en ajustant le modèle aux données expérimentales de la figure 4.15(b). Le paramètre libre obtenu est $\Delta\mu = 192\,\text{meV}$.

192 meV, ce qui constitue une estimation du transfert d'énergie entre la couche de QDs vers les agrégats J. La valeur de $\Delta\mu$ est une mesure relative qui doit être comparée à des simulations similaires pour des CPAs de différents diamètres, et qui est en travail en cours. Nous pouvons également noter un point important. Pour le moment, cette simulation ne tient pas compte de l'éventuelle excitation directe des agrégats J par le laser. En présence d'une excitation directe, le nombre de molécules d'agrégats J qui sont excitées via un transfert d'énergie depuis les QDs serait alors plus faible que sans excitation directe, ce qui rend délicat une estimation quantitative des émetteurs qui participent au transfert d'énergie. Le développement actuel de ces calculs est en cours, au moment où ce manuscrit est écrit.

Dans ce chapitre, nous avons étudié des échantillons dans lesquels différents modes de propagation coexistent en raison de la photoblanchiment d'une couche homogène d'agrégats J. La grande force d'oscillation de ce matériau le rend approprié pour l'observation d'un couplage fort entre les émetteurs fluorescents et les SPP. Nous avons déposé des QDs pour sonder l'environnement électromagnétique dans des zones de photo-blanchiment circulaire de différents diamètres afin d'observer

l'influence non-locale des polaritons hybridés dans leurs vicinités. Dans ce système riche, où les propriétés physiques sont déterminées par une interaction entre le transfert d'énergie et le couplage en champ proche, nous avons adopté différentes approches pour caractériser l'interaction entre les émetteurs fluorescents. Outre la spectroscopie dans l'espace réciproque réalisée au centre des CPAs, nous avons analysé, dans le cadre d'une collaboration avec l'équipe Plasmonique et Nanophotonique Quantique du LCFIO, le système à travers un modèle considérant l'émission thermique d'émetteurs excités qui reproduit correctement nos observations. Comme le nombre de photons émis est lié au nombre de molécules d'agrégats J et de QDs excités, ils acquièrent un potentiel chimique non nul, contrairement à un corps noir ordinaire. Nous extrayons une différence du potentiel chimique du rayonnement comme le paramètre qui permet de faire correspondre l'intensité relative des deux matériaux actifs de l'échantillon avec les données expérimentales correspondantes.

## C.5 Chapitre V: Hybridation entre deux colorants fortement couplés à un plasmon

Dans ce chapitre, nous présentons l'étude de l'hybridation entre un SPP et deux espèces d'émetteurs fluorescents séparés spatialement. Il s'agit de colorants (agrégés J) qui peuvent entrer indépendamment en couplage fort avec le SPP. Le premier est le TDBC et le second est un autre colorant cyanine avec des bandes d'absorption et d'émission décalées vers le rouge par rapport au spectre d'émission du TDBC. Le travail présenté ici s'inscrit dans le cadre d'une collaboration entre l'équipe Matériaux et Nanostructures Photoniques, dirigée par Joel Bellessa à l'ILM Lyon, et notre équipe à l'Institut Langevin. Nous remercions Sylvain Minot, Antoine Bard, Alban Gassenq, Jean-Michel Benoit, et François Bessueille pour le développement et l'optimisation du processus de fabrication des échantillons. Nous remercions Antoine Bard, Clémentine Symonds, et Joel Bellessa pour la caractérisation optique des échantillons en champ large, qui nous a permis de prouver l'hybridation des modes dans l'échantillon. A l'Institut Langevin, nous avons réalisé une caractérisation optique qui consistait à observer le comportement du système sous une excitation très focalisée et à sonder localement la réponse luminescente.

Les échantillons que nous étudions dans ce chapitre consistent en des réseaux périodiques de deux agrégats J déposés sur un film d'argent mince de 50 nm. Les maxima d'émission des colorants sont séparés par ~ 39 nm (127 meV) et que le spectre d'absorption du S2278 présente un chevauchement non négligeable avec l'émission du TDBC. L'objectif de la conception de l'échantillon est de créer des zones dans lesquelles les deux espèces de colorants fluorescents sont séparées dans l'espace. À cette fin, deux films minces différents structurés en réseaux carrés périodiques sont superposés et déposés par une technique de lithographie douce appelée impression par microcontact ($\mu$CP). La figure C.7a montre la structuration de l'échantillon en observant un scan par microscopie à force atomique. Il est constitué d'une couche homogène de TDBC avec un réseau de trous 2D de diamètre $\varnothing_h = 4,25\,\mu$m et d'un réseau complémentaire du S2278 constitué de disques de diamètre $\varnothing_d = 3,75\,\mu$m. Les deux réseaux ont une période spatiale de $5,\mu$m. Il est important de noter qu'il existe une séparation spatiale entre les deux colorants avec un contact négligeable entre leurs bords. À partir de maintenant, nous appellerons le TDBC le colorant-1 et le S2278 le colorant-2.

Ces molécules peuvent entrer dans un régime d'interaction à couplage fort avec la SPP de manière indépendante. En les déposant sur le dessus d'un même film d'argent, dans des régions séparées par des distances inférieures à la longueur de propagation du SPP, nous cherchons à observer leur hybridation simultanée avec le SPP. La figure C.7b montre le spectre de réflectivité en lumière blanche de l'échantillon dans lequel nous observons l'existence de deux anticroisements aux résonances des excitons qui produisent trois branches polaritoniques, comme attendu pour un système fortement couplé entre un mode photonique et deux émetteurs. Nous classons ces branches selon leur gamme d'énergie, à savoir la branche du polariton bas (LP) ($E < 1968,0\,$meV), la branche du polariton du milieu (MP) ($1968,0\,\text{meV} < E < 2101,4\,\text{meV}$) et la branche du polariton haut (UP) ($E > 2101,4\,$meV). Le centre des creux de réflectivité pour plusieurs énergies est marqué par des points noirs.

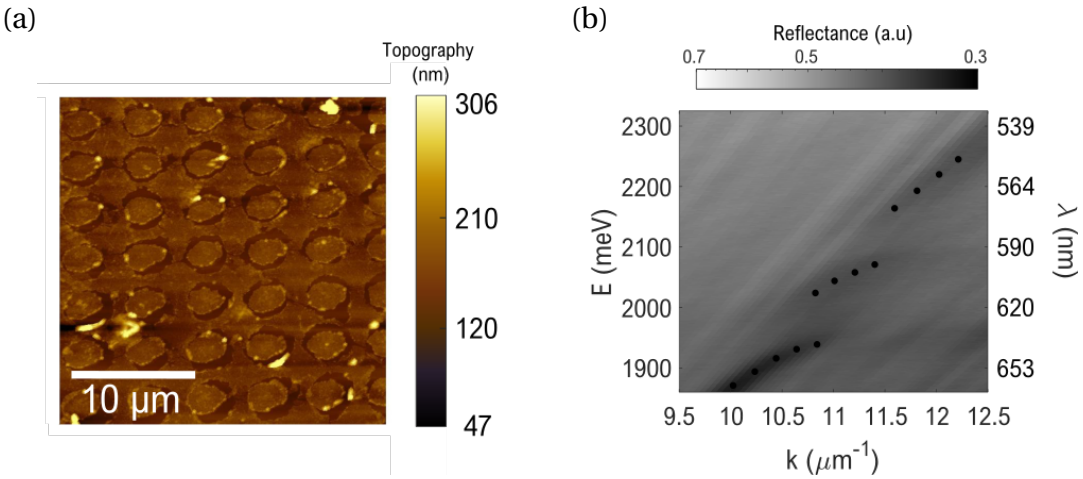


Figure C.7 – a) Les mesures AFM montrent le dépôt réussi de TDBC et de S2278 structurés, avec une épaisseur de couche de ~ 16 nm pour les deux cas. On observe que le chevauchement spatial entre les colorants correspondant aux deux motifs est négligeable. De plus, il existe des espaces vides dans la couronne comprise entre les disques de S2278 et le TDBC. b) Réflectance de l'échantillon à l'aide d'un éclairage à grand champ ($\varnothing = 50\,\mu$m). L'image montre deux anticroisements aux résonances des agrégats J, ce qui crée trois branches polaritoniques : le polariton supérieur (UP), le polariton moyen (MP) et le polariton inférieur (LP). Les minima de dips sont indiqués par des points noirs. Pour améliorer la visualisation des modes, nous avons tracé l'image avec une distribution logarithmique de la carte des couleurs. Mesures effectuées par A. Bard à l'ILM .

Une fois qu'on a observé l'hybridation entre les dexu colorants et le SPP, nous étudions la réponse locale PL de l'échantillon sous une excitation étroitement focalisée. De cette manière, nous examinons la propagation des modes hybrides, et donc l'extension du transfert d'énergie du colorant-1 vers le colorant-2. Comme le montre la figure C.8 dans laquelle toutes les images ont été acquises à l'aide d'une excitation laser de 532 nm. Nous avons commencé par trouver une région présentant une bonne qualité de dépôt des couches de colorant. Les figures C.8a et C.8b montrent la fluorescence de l'échantillon sous un éclairage à grand champ, dans des régions où l'homogénéité et la continuité sont observées dans un diamètre de ~ 10 $\mu$m. Afin d'observer séparément le signal émis par le colorant-1 et celui émis par le colorant-2, deux filtres larges de 10 nm respectivement centrés à 590 nm (Figure C.8a) et à 620 nm (Figure C.8b) ont été insérés dans le chemin de détection. Après cette étape préliminaire en champ large pour trouver une bonne région de l'échantillon, nous avons effectué la mesure avec un spot d'excitation focalisé à $(x, y) = (0, 0)\,\mu$m. La figure C.8c

montre la fluorescence de l'échantillon, dans laquelle, grâce au faisceau focalisé, seul le colorant-1 est directement excité. Comme prévu, l'excitation produit une émission brillante à son foyer, mais le PL des deux disques de colorant-2 adjacents à la position d'excitation est également visible ($y \sim \pm 2.5\,\mu$m). Nous notons que le PL de disques encore plus éloignés peut être observé, comme celui à $(x, y) = (6, -3)\,\mu$m. De plus, il semble que l'observation du PL du colorant-2 soit directement corrélée à la continuité de la couche de colorant-1. Lorsque la couche de colorant-1 est continue, le PL du colorant-2 est observé et vice-versa.

Nous avons ensuite effectué une mesure spatio-spectrale dans laquelle nous avons imagé le PL sur la fente du spectromètre, qui est le long de la direction $y$, centrée sur le spot d'excitation. Pour des raisons de clarté, la position de la fente est représentée sur la figure C.8c. La position de la fente coïncide avec le point d'excitation et la taille de la fente correspond à $\Delta x = 1,04\,\mu$m sur le plan de l'échantillon. Cette valeur est choisie afin d'éviter la détection du PL provenant des disques adjacents à l'excitation dans l'axe $x$. Pour chaque pixel sur l'axe $y$, un spectre est mesuré. Le résultat de cette mesure est représenté sur la figure C.8d. Pour $y = 0\,\mu$m, on observe le PL du colorant-1, tandis que pour $y = \pm 2.5\,\mu$m, on observe le PL du colorant-2. Le colorant-1 est directement excité par le laser, ensuite, il se relaxe partiellement à travers les modes de propagation hybrides du système, qui à leur tour excitent le colorant-2. De cette façon, nous avons observé un transfert d'énergie assisté par le produit polaritons de l'hybridation des excitons du colorant-1 et du colorant-2, et le SPP. Il existe une autre fraction des molécules excitées du colorant-1 qui sont découplées des polaritons et émettent comme des émetteurs localisés.

Nous avons étudié l'interaction entre des agrégats J spatialement séparés avec un SPP se propageant à une interface argent/diélectrique. Dans ce système, les propriétés optiques sont déterminées par l'interaction entre le couplage exciton/plasmon et l'interaction non-locale entre les matériaux actifs. Des échantillons dans lesquels le dépôt de deux structures superposées ont été fabriqués avec succès par l'équipe de nos collaborateurs à l'ILM par $\mu$CP, permettant de séparer spatialement le colorant-1 du colorant-2. Les mesures de réflectométrie à grand champ de ce système ont montré deux anticroisements de l'ordre de 100 meV, et trois branches polaritoniques correspondantes. Ensuite, nous avons montré comment le fort couplage du système canalise l'émission radiative à travers la branche inférieure du polariton. Nous avons

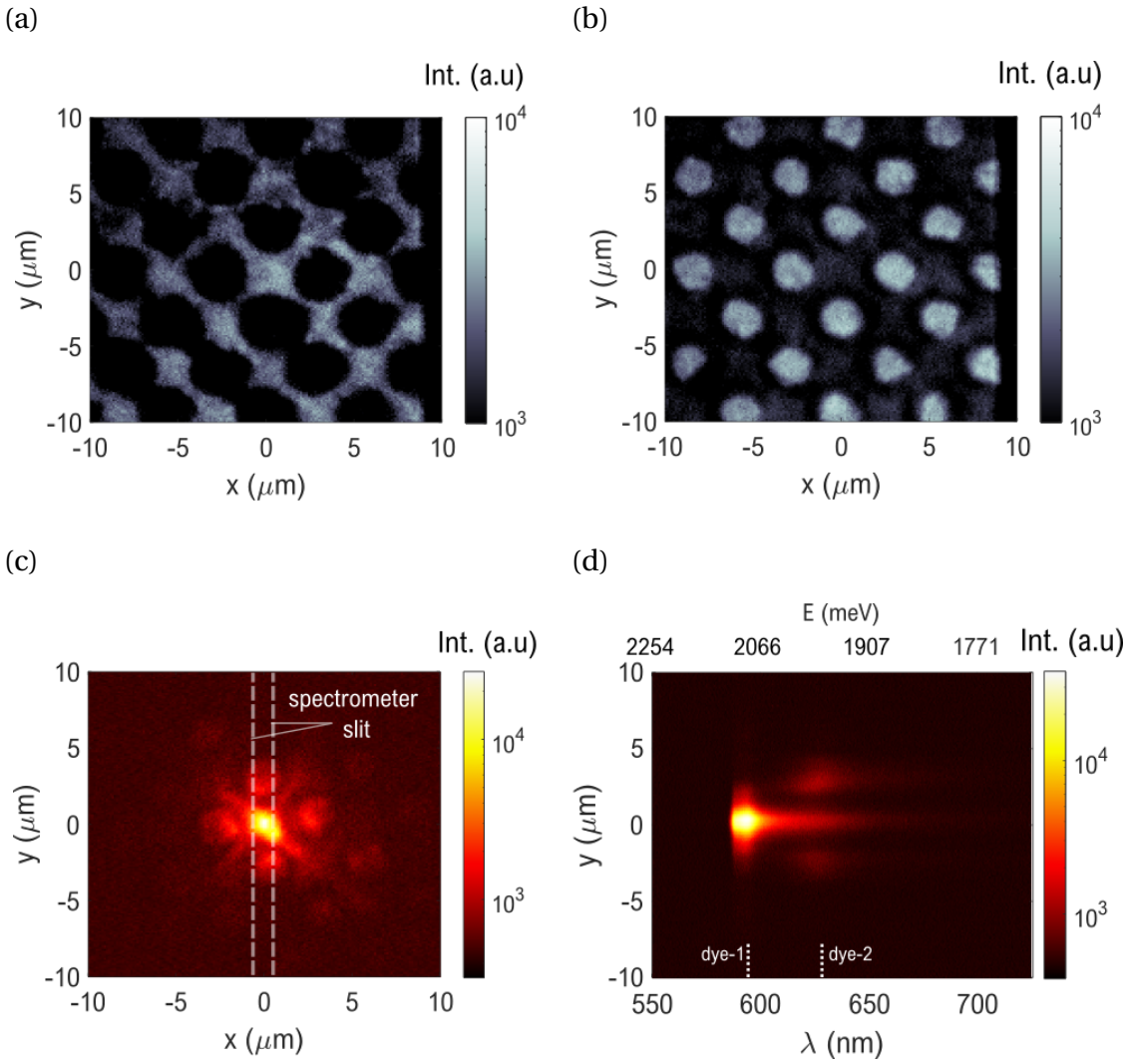


Figure C.8 – Photoluminescence sous une excitation localisée. Pour s'assurer de la qualité de l'échantillon autour de la zone d'excitation, nous avons réalisé des images de fluorescence en champ large sur la même région en utilisant un filtre passe-bande de 10 nm centré à a) 590 nm pour observer les disques de colorant-1 et à b) 620 nm pour observer la continuité du film correspondant au colorant-2. La carte des couleurs a une échelle logarithmique. Les images sont centrées sur la position d'excitation. c) PL sous une excitation laser focalisée de 532 nm dans laquelle l'émission des deux colorants peut être observée. d) Image spatiale vs spectrale correspondante. La lumière provenant des disques à $y = (0, \pm 2.5)\,\mu$m sur c) est à la longueur d'onde du colorant-2 sur d).

testé le transfert d'énergie entre les modes hybrides du système sous illumination à champ large (mesures effectuées à l'ILM) et sous illumination focalisée (mesures effectuées à l'Institut Langevin). Nous avons observé que favoriser la propagation des plasmons en regardant les zones où le dépôt de colorant est exempt de défauts favorise le transfert d'énergie entre le colorant-1, qui agit comme le donneur, vers le colorant-2, l'accepteur. De plus, dans une expérience où la fente du spectromètre est séparée de $\sim 2\,\mu$m du foyer d'excitation, nous avons observé de la lumière à des longueurs d'onde proches de la ligne d'exciton du colorant-2, là où il n'est pas déposé. L'origine de cette émission pourrait être une relaxation du système par le polariton bas. Nous rappelons que dans toutes les mesures présentées dans ce chapitre, nous avons écarté tout effet FRET puisque les différents colorants sont séparés par une distance supérieure à 100 nm.

## C.6 Conclusions

Dans cette thèse, nous avons étudié le couplage fort entre des couches structurées d'agrégats J avec des polaritons plasmoniques de surface dans le cadre d'une collaboration entre l'Institut Langevin et l'Institut Lumière Matière (ILM) Lyon. Nous avons présenté deux expériences différentes, la première dans laquelle nous sondons l'interaction de boîtes quantiques semi-conducteurs avec le système fortement couplé. La seconde expérience correspond à deux agrégats J spatialement séparés en fort couplage avec le polariton plasmonique de surface.

Dans le chapitre 4, nous avons présenté l'étude d'un échantillon constitué de boîtes quantiques déposés au-dessus d'une couche d'agrégats J contenant des zones inactives produites par lithographie optique. Nous avons observé la formation d'une branche haute et d'une branche basse de polariton à la résonance exciton/plasmon avec un écart de Rabi correspondante supérieure à 150, meV pour différents échantillons. Ensuite, nous avons déposé des QDs émettant à trois longueurs d'onde (pour trois échantillons différents) afin de sonder l'environnement électromagnétique créé par le système fortement couplé. Nous avons résolu spectralement le modèle d'émission des différents échantillons en observant que les QDs sont faiblement couplés aux modes disponibles de l'environnement. Pour modéliser la photoluminescence du système de l'un des échantillons, nous avons collaboré avec l'équipe Plasmonique

et Nanophotonique Quantique du Laboratoire Charles Fabry. Nous avons utilisé un modèle basé sur la loi de Kirchhoff locale considérant l'émission thermique d'ensembles d'émetteurs excités [6; 15], qui reproduit fidèlement nos observations.

Dans le chapitre **??**, nous avons étudié l'interaction entre des agrégats J spatialement séparés avec un SPP se propageant à une interface argent/diélectrique. Nous avons fabriqué avec succès des échantillons dans lesquels le dépôt de deux structures superposées par $\mu$CP nous permet de séparer spatialement le colorant-1 (TDBC agrégé) du colorant-2 (S2278 agrégé). Les mesures de réflectométrie à large champ de ce système ont montré deux anticroisements de l'ordre de 100, meV, et trois branches polaritoniques correspondantes. En utilisant une excitation focalisée, nous avons observé que les zones, où le dépôt de colorant est exempt de défauts favorisent la propagation des modes du système, ce qui favorise le transfert d'énergie du colorant-1 vers le colorant-2. Notamment, nous avons observé une émission du système à des longueurs d'onde proches de la ligne d'exciton du colorant-2 dans les régions où seule la couche de colorant-1 est déposée, probablement produite par la relaxation du système à travers le LP. Nous avons écarté tout effet FRET puisque les différents colorants sont séparés par une distance de 100 nm.

# References


[1] J. Bellessa, C. Bonnand, J. C. Plenet, and J. Mugnier, *Phys. Rev. Lett.* **93**, 036404 (2004). X, XII

[2] S. Aberra Guebrou, C. Symonds, E. Homeyer, J. C. Plenet, Y. N. Gartstein, V. M. Agranovich, and J. Bellessa, *Phys. Rev. Lett.* **108**, 066401 (2012). XII

[3] K. Chevrier, J. M. Benoit, C. Symonds, S. K. Saikin, J. Yuen-Zhou, and J. Bellessa, *Phys. Rev. Lett.* **122**, 173902 (2019). X, XII

[4] D. Bouchet, D. Cao, R. Carminati, Y. De Wilde, and V. Krachmalnicoff, *Phys. Rev. Lett.* **116**, 037401 (2016). X, XII

[5] D. Bouchet, E. Lhuillier, S. Ithurria, A. Gulinatti, I. Rech, R. Carminati, Y. De Wilde, and V. Krachmalnicoff, *Phys. Rev. A* **95** (2017). X, XII

[6] J.-J. Greffet, P. Bouchon, G. Brucoli, and F. Marquier, *Physical Review X* **8**, 021008 (2018). X, XXIII, XXIV, XXXII

[7] C. Perez, *et al. In preparation* (2021). X

[8] E. Bailly, *et al. In preparation* (2021). X

[9] E. M. Purcell, H. C. Torrey, and R. V. Pound, *Physical review* **69**, 37 (1946). XI

[10] D. G. Lidzey, D. Bradley, M. S. Skolnick, T. Virgili, S. Walker, and D. Whittaker, *Nature* **395**, 53–55 (1998). XI

[11] D. G. Lidzey, D. Bradley, T. Virgili, A. Armitage, M. S. Skolnick, and S. Walker, *Phys. Rev. Lett.* **82**, 3316–3319 (1999). XI

[12] V. M. Agranovich, M. Litinskaia, and D. G. Lidzey, *Physical Review B* **67**, 085311 (2003). XII

[13] K. Chevrier, *Cohérence dans les systèmes métal/organique en couplage fort états étendus et métasurfaces*, Ph.D. thesis, Université Claude Bernard - Lyon I (2019). XV

[14] J. Grandidier, G. Colas Des Francs, S. Massenot, A. Bouhelier, L. Markey, J.-C. Weeber, C. Finot, and A. Dereux, *Nano Letters* **9**, 2935–2939 (2009). XV

[15] P. Wurfel, *Journal of Physics C: Solid State Physics* **15**, 3967 (1982). XXIII, XXIV, XXXII

## RÉSUMÉ

Dans cette thèse, nous étudions l'interaction entre un ensemble d'émetteurs fluorescents (boîtes quantiques ou colorants organiques) et un système fortement couplé formé par une couche structurée de molécules de colorant hybridées avec des polaritons de plasmon de surface. Le manuscrit est organisé en cinq chapitres. Le chapitre 1 résume brièvement l'historique du développement de systèmes présentant un couplage fort entre émetteurs et modes photoniques/plasmoniques à température ambiante. Le chapitre 2 introduit, d'un point de vue théorique, le mécanisme de couplage entre la lumière et la matière dans le contexte de la plasmonique et présente les formalismes (tels que la méthode de la matrice de transfert) avec lesquels nous caractérisons les échantillons étudiés. Dans le chapitre 3, nous détaillons les montages optiques qui ont été utilisés pour la mesure de la réponse spectrale des échantillons, dans l'espace réel et réciproque. Des mesures de réflectance et de photoluminescence ont été effectuées. Le comportement temporel de la photoluminescence a également été caractérisé. Le chapitre 4 présente le travail principal de cette thèse, dans lequel nous sondons les modes d'un système fortement couplé avec un ensemble de boîtes quantiques colloïdales. Pour commencer, nous déposons une couche de colorant organique sur un film mince d'argent. L'exciton du colorant s'hybride avec le plasmon de surface se propageant à l'interface entre l'argent et le milieu diélectrique. La couche de colorant a été structurée par lithographie optique pour créer des zones de diamètres variables dans lesquelles le matériau est optiquement inactif. Une couche de matrice polymère dans laquelle sont incorporées des boîtes quantiques colloïdales, déposée sur la couche de colorant, est utilisée pour sonder les modes de l'environnement électromagnétique. Un modèle basé sur la loi de Kirchhoff locale est utilisé pour simuler les données expérimentales. Dans le chapitre 5, nous étudions l'hybridation de deux colorants organiques spectralement différents avec un plasmon de surface en propagation. Contrairement à l'échantillon précédent, les deux espèces de colorants sont toutes deux en couplage fort avec le plasmon de surface. Les couches de colorants sont structurées de telle sorte que les deux espèces ne se chevauchent pas dans l'espace et qu'elles n'interagissent que par des modes de propagation. Tout d'abord, nous démontrons l'existence de modes hybridés dans l'échantillon par des mesures de réflectométrie. Ensuite, nous présentons des images spatiales-spectrales dans lesquelles la luminescence du système est étudiée lors de l'excitation sélective de la région peuplée par une seule espèce de colorant.



## MOTS CLÉS

Couplage exciton-plasmon - Nanostructures plasmoniques - Couplage fort - Nanophotonique - Microscopie de champ proche.



## ABSTRACT

In this thesis, we study the interaction between an ensemble of fluorescent emitters (either quantum dots or organic dyes) and a strongly coupled system formed by a structured layer of dye molecules hybridized with surface plasmon polaritons. The manuscript is organized into five chapters. Chapter 1 briefly summarizes the development of systems showing strong coupling between emitters and photonic modes at room temperature from a historical perspective. Chapter 2 introduces, form a theoretical point of view, the coupling mechanism between light and matter in the context of plasmonics and presents the formalisms (such as the Transfer-Matrix Method) with which we characterize the studied samples. In Chapter 3, we detail the optical setups that have been used for the measurement of the spectral response of the samples, in both real and reciprocal space. Both reflectance and photoluminescence measurements have been performed. The temporal behavior of photoluminescence has also been characterized. Chapter 4 presents the leading work of this thesis, in which we probe the modes of a strongly coupled system with an ensemble of colloidal quantum dots. To begin with, we deposit an organic dye layer on top of a silver thin film. The exciton of the dye hybridizes with the surface plasmon propagating at the interface between the silver and the dielectric medium. The dye layer was structured by optical lithography to create zones of varying diameters in which the material is optically inactive. A layer of colloidal quantum dots embedded in a polymer matrix, deposited on top of the dye layer, is used to probe the modes of the electromagnetic environment. A model based on the local Kirchhoff's law is used to simulate the experimental data. In Chapter 5, we study the hybridization of two spectrally different organic dyes with a propagating surface plasmon. Contrarily to the previous sample, the two species of dyes are both in strong coupling with the surface plasmon. The dye layers are structured in such a way that the two species do not overlap spatially so that they only interact through propagating modes. First, we demonstrate the existence of hybridized modes in the sample through reflectometry measurements. Then, we present spatial-spectral images in which the luminescence of the system is studied upon selective excitation of the region populated by only one dye's species.



## KEYWORDS

Exciton-plasmon coupling - Plasmonic nanostructures - Strong coupling regime - Nanophotonics - Near-field microscopy.